THE HONG KONG POLYTECHNIC UNIVERSITY

The Department of Electrical Engineering

A Robust Full-Digital Drive for Linear Permanent Magnet Synchronous Motors

Michael Shing-Wai TAM

Thesis for the degree of Master of Philosophy

April 2005

CERTIFICATE OF ORIGINALITY

I hereby declare that this thesis is my own work and that, to the best of my knowledge and belief, it reproduces no material previously published or written nor material which has been accepted for the award of any other degree or diploma, except where due acknowledgement has been made in the text.

_____ (Signed)

Shing-Wai TAM (Name of student)

ABSTRACT

The applications of Linear Permanent Magnet Synchronous Motors (LPMSMs) are becoming more and more popular in the semiconductor package industry. This is due to the fact that substantial cost can be saved through reduced mechanical parts, and simple mechanical adjustments and alignments. LPMSM also improves the speed, precision and the overall reliability. In many industrial processes, there are needs for the transportation of various work loads with different masses from one place to another by LPMSMs. Examples are transportation of the lead-frame to the bonding platform, and the processed lead-frame to the storage magazine. These factors attract an investigation into the high-speed robust control for LPMSM.

The objective of this research project is to investigate the LPMSM characteristics, and to develop a robust and high-performance fully digital drive for the high-speed and high-precision operation of LPMSM.

The investigation is divided into 3 stages:

(i) Construct a fully digital drive for LPMSM, and perform closed-loop position control under existing driving method. Investigate its performance and shortcomings.

(ii) Propose a robust and high-performance driving scheme that is suitable for the high-speed and high-precision control of LPMSM. This includes:

   (a) the modeling of the system drive, and

   (b) the simulation of the driving scheme using Matlab/Simulink.

(iii) Implement in hardware the proposed driving scheme and verify its performance.

ACKNOWLEDGEMENTS

I would like to thank my research supervisors, Dr. N.C. Cheung and Prof. D. Sutanto, for giving valuable suggestions and constructive guidance throughout this research project. Also, I would like to thank my company, the ASM Assembly Automation, for the full-support of my research project, by providing the necessary measurement equipment, facilities and the linear permanent magnet synchronous motor. Finally, I have to say thank you to my family, especially my wife, Samantha, for their continuous support and encouragement on my work on the research.

ABBREVIATIONS

The descriptions of the abbreviations that used in this research project are listed below:

Abbreviations	Description
2DOF:	2 Degree Of Freedom
ADC:	Analog-to-Digital Converter
DAC:	Digital-to-Analog Converter
DC:	Direct Current
DSP:	Digital Signal Processor
EMF:	Electro-Motive Force
EMI	Electro-Magnetic Interference
IC:	Integrated Circuit
IO:	Input Output
LPMSM:	Linear Permanent Magnet Synchronous Motor
MCU:	Micro-Controller Unit
MMF:	Magneto-Motive Force of a magnetic circuit
MOSFET:	Metal-Oxide Semiconductor Field Effect Transistor
PC:	Personal Computer
PLD	Programmable Logic Device
PMSM:	Permanent Magnet Synchronous Motor
PWM:	Pulse-Width Modulation
RPMSM:	Rotary Permanent Magnet Synchronous Motor
SISO:	Single-Input Single Output
SMPS:	Switching Mode Power Supply
SV:	Space Vector

TABLE OF CONTENTS

CHAPTER ONE INTRODUCTION

In this chapter, the applications of the Linear Permanent Magnet Synchronous Motor (LPMSM) are presented. They lead to the motivation for the research project. Afterwards, the objectives of the research are listed, then followed by the contributions of the research work. The organization of the thesis is described at the end of this chapter.

1.1 MOTIVATION

Permanent magnet motors are used in a wide variety of applications [1]. Their use has increased following the availability of the Neodymium-Iron-Boron magnetic material. Permanent Magnet Synchronous Motors (PMSM) using the Neodymium-Iron-Boron magnets are characterized by high thrust density, low loss, small electrical time constant and rapid response [25, 26]. In addition, the brushless version of the PMSM implies that the motor has higher efficiency as well as lower maintenance than the brush type PMSM [27]. Moreover, the deterioration of performance over the lifetime of the motor is minimal [36].

In the applications where linear motion is required, the linear PMSM has additional advantages over the rotary type PMSM. It has a simple structure, lower cost, reduced size, and improved reliability. In addition, the direct drive characteristic of the linear LPMSM allows the delivery of very high-speed motions under great precision [28]. Owing to the above reasons, linear PMSMs are becoming important actuators in high performance motion systems. Linear and rotary PMSMs are used for computer hard and floppy disc drives, with about 10 million units are produced each year for the above purpose alone [15]. In the manufacturing industry, they are utilized in servo drives for machine tools, X-Y tables, bond head actuators and robotic arms [28].

Since linear PMSMs are directly drive actuators, the traditional damping effect from the ball-screw and nuts in traditional rotary-to-linear motion system is absent [39]. Therefore, the motion performance can be directly affected by the system parameter uncertainties, such as the change of load, frictional force, and mechanical vibration. Furthermore, the relatively small electrical time constant and the open structure characteristics of the linear PMSM drive systems will generate much higher EMI noise than the traditional rotary PMSM drive systems. Faced with these new challenges, a robust control algorithm and a

sophisticated all-digital power electronic drive system are needed to overcome these problems.

1.2 OBJECTIVES

Fast response and consistent performance are the two essential requirements in linear drive systems of the semiconductor package machines [37]. For the case of the Chip-On-Board wire-bond machine, there is substantial load change as the PCB size varies with different production lots. Therefore, a high-speed motion system with the ability to withstand large load change is required.

The objectives of this research project are to propose new and innovative methodologies to overcome the above problems. Therefore, the main objectives of this project are:

(i) To develop a high speed, fully digital drive system for the linear PMSM to combat the problem of inconsistent performance.

(ii) To develop a robust control scheme to compensate the load variation problem.

1.3 CONTRIBUTIONS OF THE THESIS

In this research project, a high performance fully digital Pulse-Width Modulation (PWM) drive for the linear PMSM has been developed. Moreover, a novel robust control scheme for the high-speed and high-precision application of the linear PMSM has been proposed and implemented. Specifically, the following contributions have been made:

(i) Developed a LPMSM model that is accurate, efficient and simple to implement.

(ii) Reported on the shortcomings of traditional PID drive when it is applied to high-speed high-precision operation of LPMSM.

(iii) Proposed an innovative robust control methodology to combat the problem of inconsistence performance due to load variations.

(iv) Developed a stable and low-cost fully digital LPMSM driving platform for the test and verification of the proposed robust controller.

1.4 ORGANIZATION OF THE THESIS

Chapter one presents the motivation of this research project. It discusses the current applications of the LPMSMs and their importance in the direct linear drive system. The objectives and the contributions of this research are also described.

Chapter two is a review on the literature on the LPMSM and the control system. The mathematical model of the LPMSM is derived. The vector control scheme with the PI current control for high-performance drive of the LPMSM is presented. In addition, the model for the power drive is also derived. Finally, a novel robust control scheme to compensate the load variation for LPMSM system is proposed.

Chapter three is development of the high-performance fully digital drive for the LPMSM system. The profile generator and its advantages are presented. Afterwards, the disturbance compensated controller for improving the robustness of the LPMSM drive system is discussed. The hardware structure for implementing an all-digital digital PWM drive is proposed.

Chapter four is the modeling of the LPMSM drive system. The models of the drive system are developed by using Matlab/Simulink software. The simulation results are presented at the end of this chapter.

Chapter five discusses the implementation of the robust fully digital control system for the LPMSM. The system makes use of the PC, the DS1102 dSPACE controller card and a 3-phase power stage. The hardware circuit is also discussed.

Chapter six presents the simulation and measured results of the robust LPMSM control system. The results are compared with traditional controlling scheme.

Chapter seven summaries the results of the research project, and provides the concluding remarks. Further development works on this project are also suggested in this chapter.

CHAPTER TWO LITERATURE REVIEW

In this chapter, the rotary and linear motion drive systems will be discussed and their structural characteristics will be compared. Some issues concerning the use of linear motors will be presented and the respective solutions to these issues will be proposed. As a result, the mathematical model of the linear PMSM and the space vector control of the linear PMSM will be developed towards the end of this chapter.

2.1 THE ROTARY AND LINEAR DRIVE SYSTEM

Many industrial automation systems require linear motions for the transportation of materials for processing. One typical example is the wire-bonding machine in semiconductor packaging [33]. In this application, the die and the lead-frame are moved by a 2-dimensional moving platform where the wire bonding process is being carried out. The moving platform usually constructed from an X-Y table and the 2-dimensional movements are obtained by orthogonally cascading two linear slides together as shown in Figure 2-1.

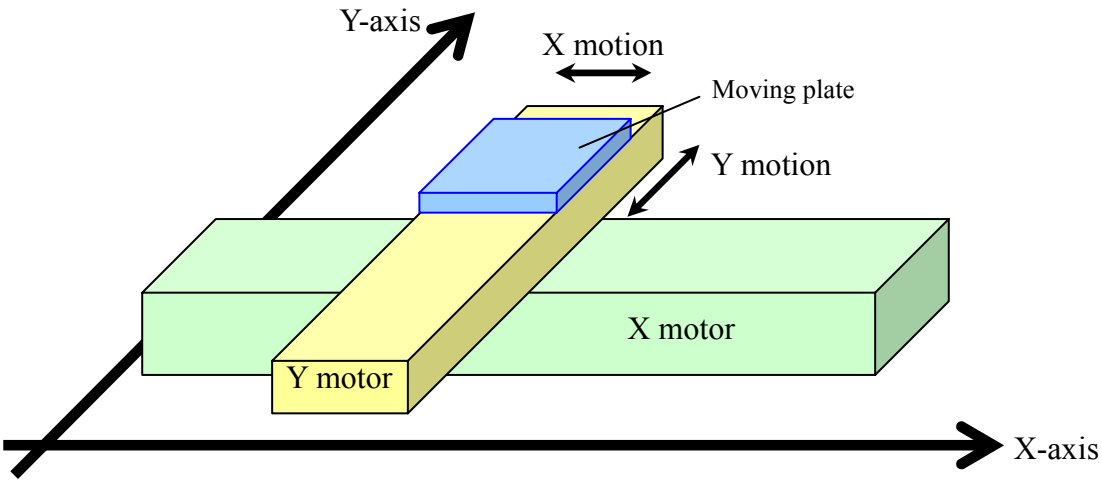

Figure 2-1 A typical X-Y table for 2 dimensions linear motion system

Figure 2-1 shows a typical X-Y table, with the moving plate mounted on the Y-motor, and the Y-motor itself cascades on the X-axis motor. Under this configuration, the X-motor has to bear the load of the moving plate and the Y-motor assembly. The linear motion guide is an important element in any complex motion requirements. Multi-dimensional motions can be achieved by cascading linear motion guides together. For example, if a vertical linear motor, Z-motor, is added to the X-Y table, a 3-dimensional motion can be achieved, and the work-load can be moved to any spatial point within the traveling range

of the three motors.

To obtain the linear motion from an electro-mechanical actuator, one can either:

(i) convert the rotation motion of a rotary motor into linear motion via a mechanical converter, such as the gear box, lead-screw or ball-screw system, or

(ii) use a direct-drive linear motor to obtain the linear motion directly.

Before discussing the above two kinds of motion actuators, the structure of the rotary and linear motors will be discussed first.

2.1.1 The Rotary Permanent Magnet Synchronous Motor (RPMSM)

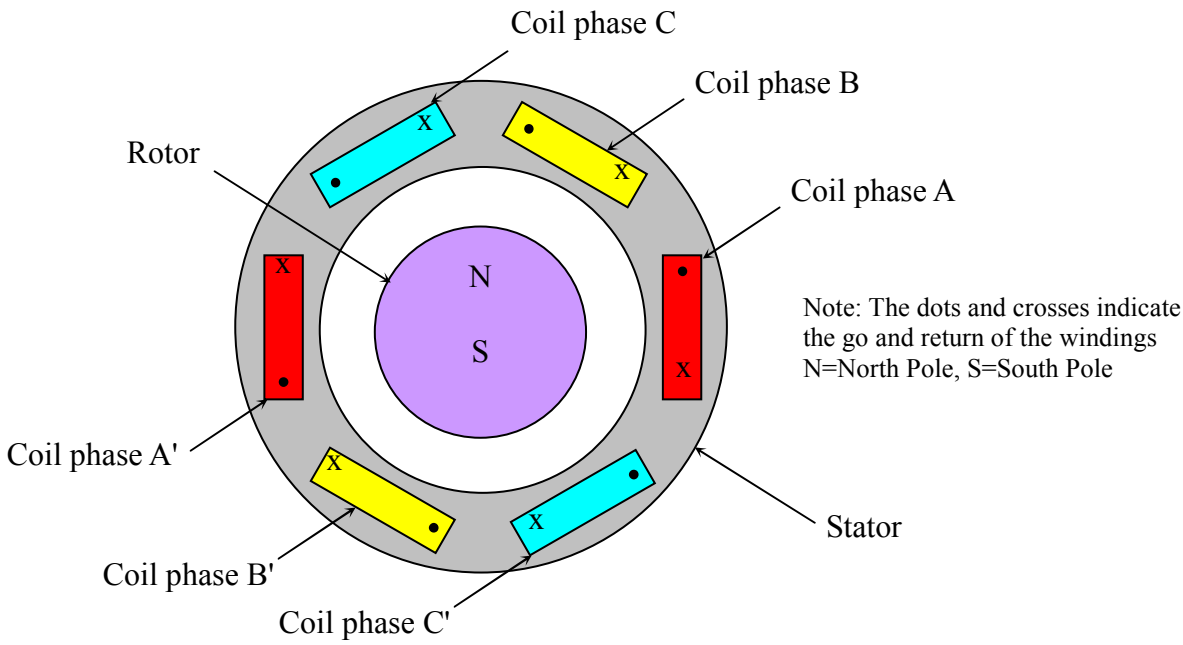

Figure 2-2 Cross-section view of an RPMSM

Figure 2-2 is the cross-sectional view of an RPMSM. The 3-phase coils for energizing the motor are normally wound on the stator for better heat dissipation. Lap windings are avoided in many industrial RPMSM in order to simplify the assembly procedure and to reduce cost [27, 36]. The coil phase A and the coil phase A' are pair of coils connected in series to have an addition effect of the generated magnetic flux. The connections of the other two pairs of coils phase B and B' and phase C and C' are similar to the phase A. The

3-phase motor coils, A, B and C, are either configured in star or delta connection.

The magnetic path is designed in a way that the magnetic flux distribution is sinusoidal. The materials for the stator are usually alloys of nickel-iron-molybdenum [15].

The rotor is made of rare-earth high-energy magnet fixed on the motor shaft and supported by two rotary bearings. In this example the rotary motor is a 2-pole moving magnet type synchronous motor. A complete cycle a 3-phase sinusoidal current input will move the rotor by an electrical angle of 360°. The radial-section view of the RPMSM is illustrated in Figure 2-3.

As compared to the brush type DC motor, the RPMSMs have the advantages of being brushless, free of maintenance, small size, high torque-to-volume ratio and able to generate less EMI noise. [2]

As the motor is a 3-phase motor, current commutation is needed in order to drive the motor properly [30, 34]. This will be further discussed in section 5.1.

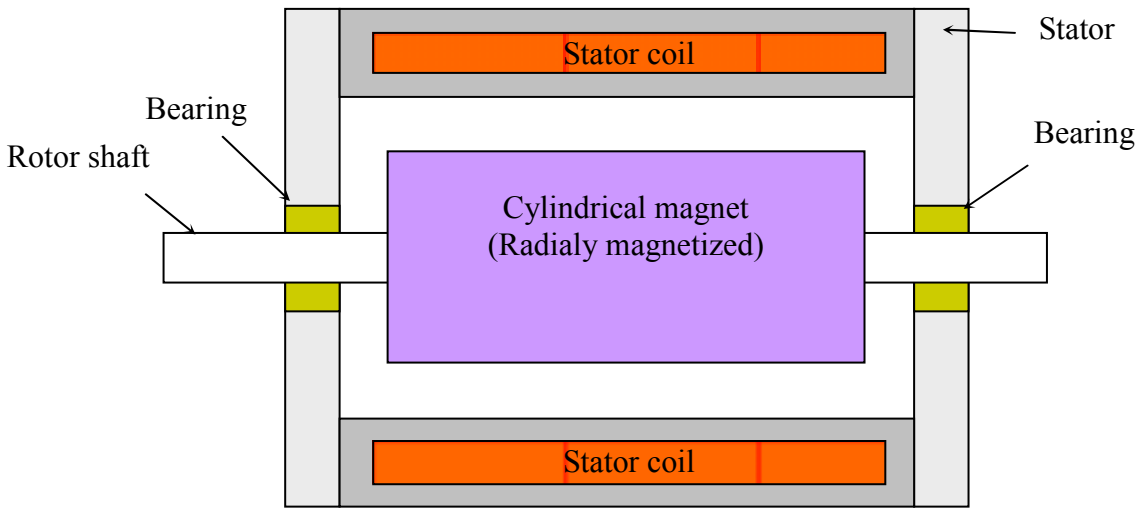

Figure 2-3 Radial-section view of an RPMSM

2.1.2 Converting Rotary Motion into Linear Motion

A number of mechanical parts are needed to convert the rotary motor motion into the linear motion. Traditionally, it is done through a mechanical converter, as shown in Figure 2-4.

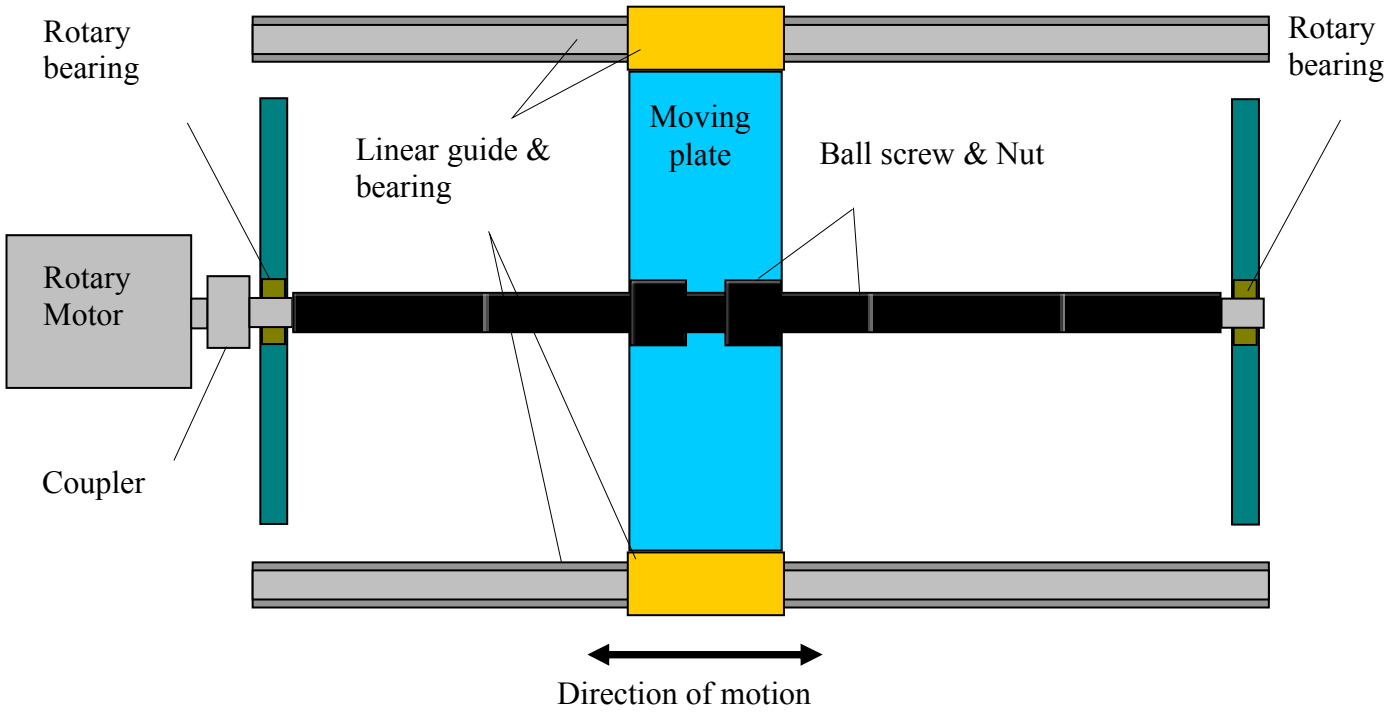

Figure 2-4 Ball-screw and nuts linear motion system

The motion system shown in Figure 2-4 is the Ball-Screw and Nut Linear Motion System [3]. The rotary motor is the mechanical power source that drives the system. As the rotary motor and the ball-screw are two individual mechanical parts, the power transmission is usually connected via a coupler, which couples the motor power to the ball-screw. The rotation axis of the motor shaft and the ball-screw has to be fully aligned. Otherwise the motor bearings and the bearings supporting the ball-screw could generate uneven stress and shorten the lifetime of the motion system [32]. Perfect alignment is very difficult, as there is no effective tool to guide and indicate a good connection. Usually the connection is checked manually by turning the screw and feeling the uneven friction. The coupler helps to reduce the mechanical stress on the parts due to slight miss-alignment. On the top of these are two rotary bearings at each side of the ball-screw for support.

The Ball-Screw and Nuts is the key component of the linear side and it has a major impact on the overall system performance, in terms of speed and precision. A fine pitch ball-screw and nut for precision application usually is very expensive. It is also the most easily damaged part when the table is subjected to shock or collision. It is also the quickest part to wear-out in the whole system. Long lifetime can not be guaranteed if it is operated in a fast acceleration/deceleration motion profile. In addition, the performance of the ball-screw can be seriously affected by dust or solid particles sticking onto them. Hence they are normally required to be operated in a clean environment and a dust shield is usually required [16].

The pair of linear guides and bearings is for guiding the moving platform to travel in a linear direction. These two linear bearings need to be mounted in perfect parallel position in order not to stress the bearing. This is the second alignment challenge. The third difficulty encountered is the mounting of the moving plate. An inaccurate or unbalanced mounting of the plate will add stress to the lead screw which then makes the lead-screw to wear-out faster.

Hence periodical maintenance of cleaning, greasing and tuning are needed to ensure a good performance of the ball-screw and nuts system.

2.1.3 The Direct Drive Linear Motion System

The direct drive linear motion system is shown in Figure 2-5. This linear motion system uses a linear motor to generate the linear motion directly. Only a pair of linear bearings is needed to support the moving platform's motion.

There are two designs for a linear permanent magnet motor. It can be of the form of a linear magnetic rail and a set of moving coils, or a linear coil-winding and a moving magnet. The moving coil type can have the advantages of smaller and lighter mover; it delivers faster dynamic response. On the other hand, the high cost of the magnet in the

stator will result in limited travel range. More magnets are needed for longer stator.

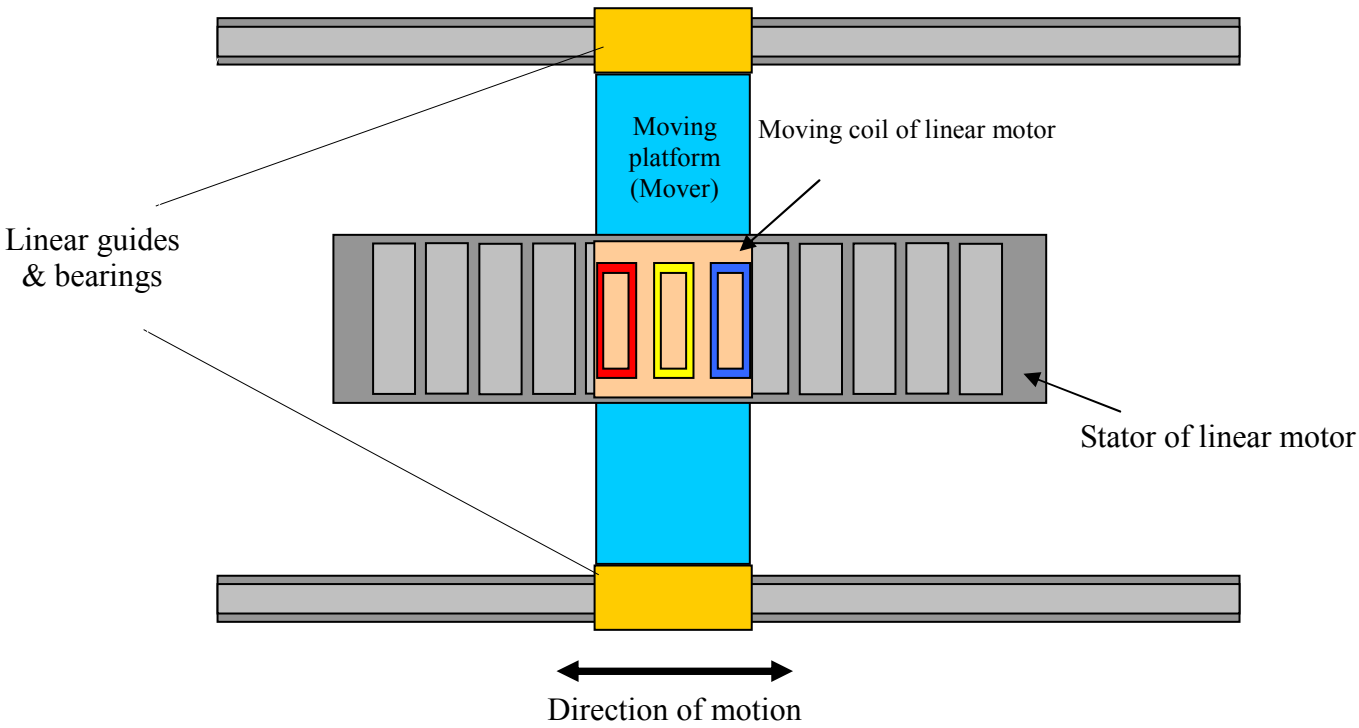

Figure 2-5 Direct drive linear motion system

The moving magnet type has a relatively lower cost. However, if the travel distance is long, the inductance of the coil will increase; it will limit the current dynamics and will result in a slow motion dynamics of the system.

Similar to the rotary drive system, there is also alignment difficulty of the linear bearings. However, the alignment problem of the linear motor is already smaller than the rotary motor because only a pair of linear guides is needed to mount and adjust.

The linear motor drive system uses less mechanical parts to convert the electrical energy into the linear mechanical motion, and the traditional mechanical coupler and translator are not necessary. These include the bearings for the rotary motor and the lead screw, and the ball-screw and nuts. All these components are very expensive in the case for high-speed and high-precision applications. Also, the mechanical hystersis as in the rotary drive linear motion system can be eliminated by using the direct linear drive linear motion system. This allows the overall system can be modeled accurately without the use of

higher order system transfer function. The driving system makes use of the linear motor which allows a simpler and more straightforward design, and resulting in a more cost-effective system. For example, for a 15cmx15cm X-Y table with 5μm accuracy, the cost reduction can be up to 80% if the rotary system is replaced by a linear one [1]. Also, the overall mechanical friction in the system is smaller, with less audible noise, and the motor can move faster. In addition, since the position sensor is attached very close to the load; the actual position of the load can be controlled more accurately. Furthermore, the system is virtually maintenance free. This results in a more robust and reliable motion system.

As compared with the rotary drive linear system, the advantages of the linear drive linear system can be summarized as follows:

(i) As there is only a pair of linear guides, mechanical alignment is easier.
(ii) Less mechanical parts so can run faster and less noise generation.
(iii) As results from (ii) above, the system is more cost effective.
(iv) Direct load control with minimum mechanical hystersis.

2.1.4 The Direct Drive Challenges

On the other hand, there are disadvantages in a direct drive linear motion system. They are:

(i) The direct disturbances from load variations,
(ii) The end-effect of the linear motor, and
(iii) The commutation of the linear motor

They are discussed in the subsequent sections.

2.1.4.1 The Direct Disturbances from Load Variations

In the rotary drive linear motion system, it is found that the frictional force introduced by the ball-screw and nuts can contribute to a better damping effect to the overall system [6, 7]. While in a direct drive linear motion system, there is an absence of such damping effect. The system is more likely to be subjected to the disturbances of system parameters drifts, such as the variation of load, the change of frictional force from the linear bearings and the thermal drift of current sensors. A robust control scheme is needed in order to solve the disturbances in the linear drive system.

2.1.4.2 End-effect of the Linear Motor

The rotary motor does not have any control problem because it has no end-travel limitation, but the linear motor always has a limited travel distance. Special attention is required to prevent the motor from running beyond the operation limits (i.e. the non-linear regions at both the ends of the linear motor). The application and software design will limit the travel of the mover within its linear traveling range.

2.1.4.3 Commutation of the Linear Motors

In the case of a rotary motor, the commutation is not a problem as the encoder count per revolution is fixed. The value of the encoder count per pole is consistent for every revolution.

This is not the same for the linear motor. Owing to the accumulative position inaccuracy in installing the magnets on a linear rail, there can be accumulative error in determining the mover position relative to the magnetic flux position. This error could be large enough to degrade the force generation of the linear motor. The control system will pump more current into the motor, and causing excessive heat dissipation in the motor. As a result, the efficiency and performance of the drive system are degraded.

To summarize, the use of linear drive system brings many advantages but also created some disadvantages. There are new challenges in deriving a control system for the linear PMSM. The ways of handling and solving those problems will be described in subsequent chapters.

2.1.5 The Linear Permanent Magnet Synchronous Motor (LPMSM)

Figure 2-6 is the structure of a LPMSM in the cross-sectional view. The stator consists of a series of magnets attached to a ferro-magnetic material which usually made from soft iron. The magnetic axis of the magnet is mounted vertically while the pole sequences of the magnets are installed in an alternating manner (i.e. north-south, south-north, north-south … etc.). By a proper design of the size, spacing of the magnets and choice of the distance above the magnets, a sinusoidal distributed magnetic flux can be obtained along the horizontal position (x), see Figure 2-6.

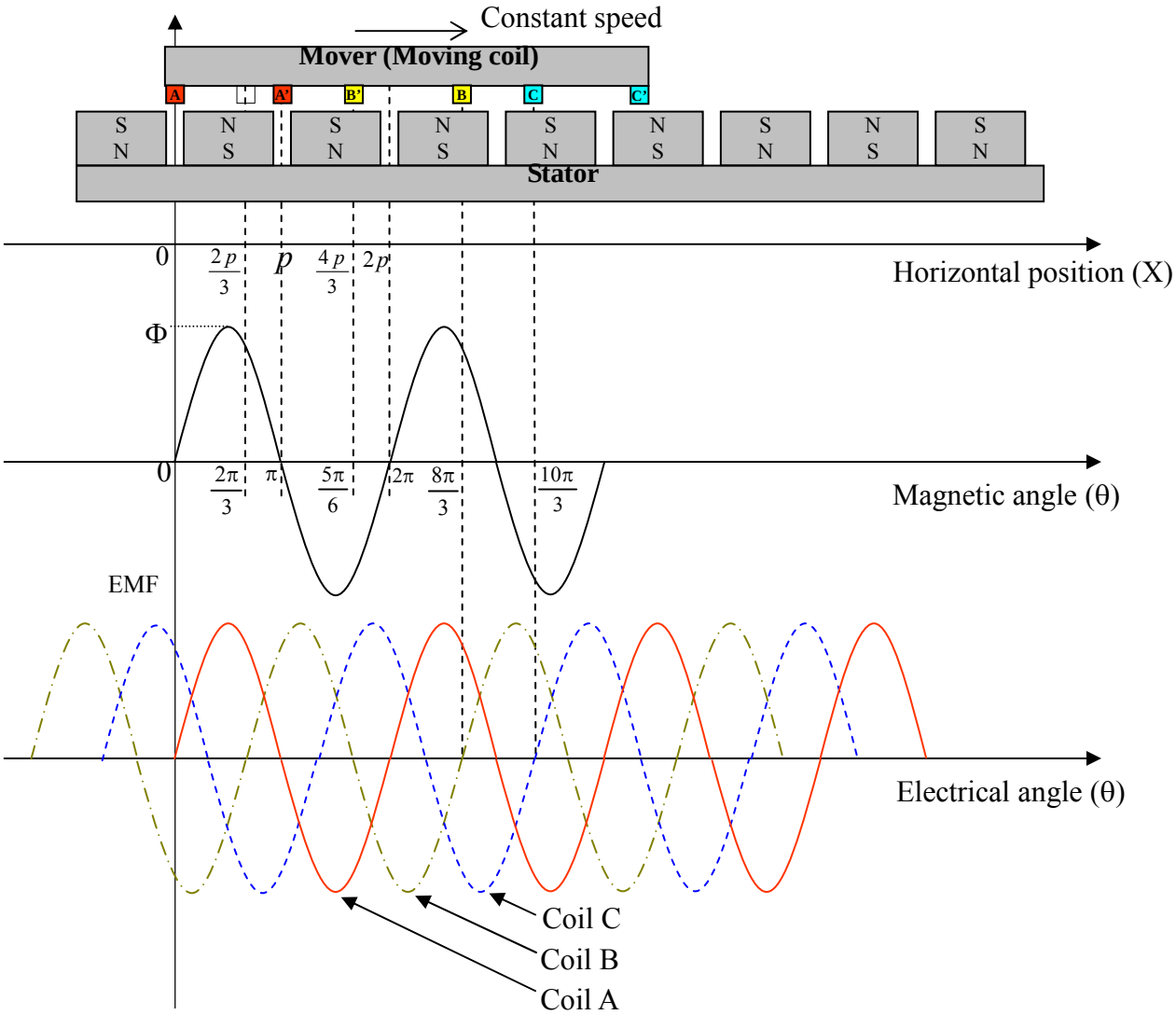

Figure 2-6 The structure, flux distribution and EMF waveforms of the LPMSM

The LPMSM as shown in Figure 2-6 is a moving coil motor with a fixed linear magnetic rail [1]. Separate winding instead of lap winding is used in this motor. Such arrangement can ease the production of the winding coils. As the coils are identical, they can be mass produced and glued to the mounting plate easily.

Taking the zero magnetic field point as zero reference, the beginning of winding A can be started at this point. The winding of phase B can start at an angle equivalent to $2\pi/3$ lagging phase A. For separate winding it is shifted a cycle backward at $8\pi/3$; but the return of the winding is situated at $5\pi/6$ in order to minimize the size of the mover. The winding of phase C is exactly $4\pi/3 + 1$ cycle lagging the winding of phase A. The positions of the coils are illustrated in Figure 2-6.

2.1.6 Model of the LPMSM

Refer to Figure 2-6, if the magnetic pole pitch is p, and the coils are moving at a constant speed u, then the distance x move in t is:

$$x = ut, \tag{2.1}$$

The corresponding magnetic angle θ in radian is:

$$\theta = \pi \frac{x}{p} \tag{2.2}$$

Or

$$\theta = \pi \frac{ut}{p}, \tag{2.3}$$

Since the magnetic flux is sinusoidally distributed, the magnetic flux linkage is also sinusoidal when the mover moves along the x-axis. With a maximum magnetic flux density Φ, the function of the magnetic flux density ϕ is thus:

$$\phi = \Phi sin(\pi \frac{ut}{p}) \tag{2.4}$$

The EMF induced e_A in the winding of phase A is the rate of change of the total flux linkage λ:

$$e_A = \frac{d\lambda}{dt}$$

$$= 2Nl\,\frac{d\phi}{dt}$$

$$= 2Nl\,\frac{d\sin\left(\pi\frac{ut}{p}\right)}{dt}$$

$$= 2\pi Nl\,\frac{u}{p}\cos\left(\frac{\pi ut}{p}\right) \qquad \textbf{(2.5)}$$

Where N is the number of turns of the winding

l is the length of the winding orthogonal to the motion

The induced EMF of windings B and C are the same as winding A except that they are $2\pi/3$ phase lag and lead to winding A respectively i.e.:

$$e_B = 2\pi Nl\,\frac{u}{p}\cos\left(\frac{\pi ut}{p} - \frac{2\pi}{3}\right) \qquad \textbf{(2.6)}$$

$$e_C = 2\pi Nl\,\frac{u}{p}\cos\left(\frac{\pi ut}{p} + \frac{2\pi}{3}\right) \qquad \textbf{(2.7)}$$

As the coils are separated from each other, assume the mutual inductances between the windings are negligible [16]. The system equation in matrix form is thus:

$$\begin{bmatrix} v_a \\ v_b \\ v_c \end{bmatrix} = \begin{bmatrix} R_a & 0 & 0 \\ 0 & R_b & 0 \\ 0 & 0 & R_c \end{bmatrix} \begin{bmatrix} i_a \\ i_b \\ i_c \end{bmatrix} + \frac{d}{dt}\begin{bmatrix} L_{aa} & 0 & 0 \\ 0 & L_{bb} & 0 \\ 0 & 0 & L_{cc} \end{bmatrix} \begin{bmatrix} i_a \\ i_b \\ i_c \end{bmatrix} + \begin{bmatrix} e_a \\ e_b \\ e_c \end{bmatrix} \qquad \textbf{(2.8)}$$

Putting (2.5) (2.6) and (2.7) into (2.8),

$$\begin{bmatrix} v_a \\ v_b \\ v_c \end{bmatrix} = \begin{bmatrix} R_a & 0 & 0 \\ 0 & R_b & 0 \\ 0 & 0 & R_c \end{bmatrix} \begin{bmatrix} i_a \\ i_b \\ i_c \end{bmatrix} + \frac{d}{dt} \begin{bmatrix} L_{aa} & 0 & 0 \\ 0 & L_{bb} & 0 \\ 0 & 0 & L_{cc} \end{bmatrix} \begin{bmatrix} i_a \\ i_b \\ i_c \end{bmatrix} + 2\pi Nl \frac{u}{p} \begin{bmatrix} cos\left(\frac{\pi ut}{p}\right) \\ cos\left(\frac{\pi ut}{p} - \frac{2\pi}{3}\right) \\ cos\left(\frac{\pi ut}{p} + \frac{2\pi}{3}\right) \end{bmatrix} \quad \textbf{(2.9)}$$

Where v_a, v_b and v_c are the voltage across the phase windings

i_a, i_b and i_c are the current flow in the phase windings

R_a, R_b and R_c are the resistance of the phase windings

L_a, L_b and L_c are the self-inductance of the phase windings

Since the three phase windings are identical, their resistances and inductances are the same and are equal to R and L respectively. The term $2\pi Nl/p$ is the EMF constant of the motor and let it equals to K_e. Therefore the LPMSM system equations of (2.9) can be re-written as:

$$\begin{bmatrix} v_a \\ v_b \\ v_c \end{bmatrix} = \begin{bmatrix} R & 0 & 0 \\ 0 & R & 0 \\ 0 & 0 & R \end{bmatrix} \begin{bmatrix} i_a \\ i_b \\ i_c \end{bmatrix} + \frac{d}{dt} \begin{bmatrix} L & 0 & 0 \\ 0 & L & 0 \\ 0 & 0 & L \end{bmatrix} \begin{bmatrix} i_a \\ i_b \\ i_c \end{bmatrix} + K_e u \begin{bmatrix} cos\left(\frac{\pi ut}{p}\right) \\ cos\left(\frac{\pi ut}{p} - \frac{2\pi}{3}\right) \\ cos\left(\frac{\pi ut}{p} + \frac{2\pi}{3}\right) \end{bmatrix} \quad \textbf{(2.10)}$$

Assume 100% electro-mechanical energy transfer, the thrust force, F_e , produced by the motor is:

$$F_e = \frac{1}{u} (i_a e_a + i_b e_b + i_c e_c) \quad \textbf{(2.11)}$$

Taking into account the frictional force F_F, the mover's inertia M_M, the cogging force F_C and the load F_L, the mechanical force output is:

$$F_M = M_M \frac{d}{dt} u + B u + F_L + F_C \qquad (2.12)$$

Where B is the frictional constant

With the derived equations for the LPMSM, the next task is to find a way of driving the LPMSM. The possible ways of driving the motor will be discussed in the next section.

2.1.7 The LPMSM

The LPMSM used in this project is the moving coil type. Figure 2-7 shows the overview of the LPMSM. This includes the mover, linear bearings, stator and dummy load. The linear motor moves horizontally in the 'x' direction, it is so called the x-axis motor. The mass of the dummy load shown in the figure is 0.5kg. Dummy load of different mass can be mounted on the mover easily for performance testing. The linear bearings for guiding the motion are mounted in the front. The total traveling range of the linear motor is 30cm.

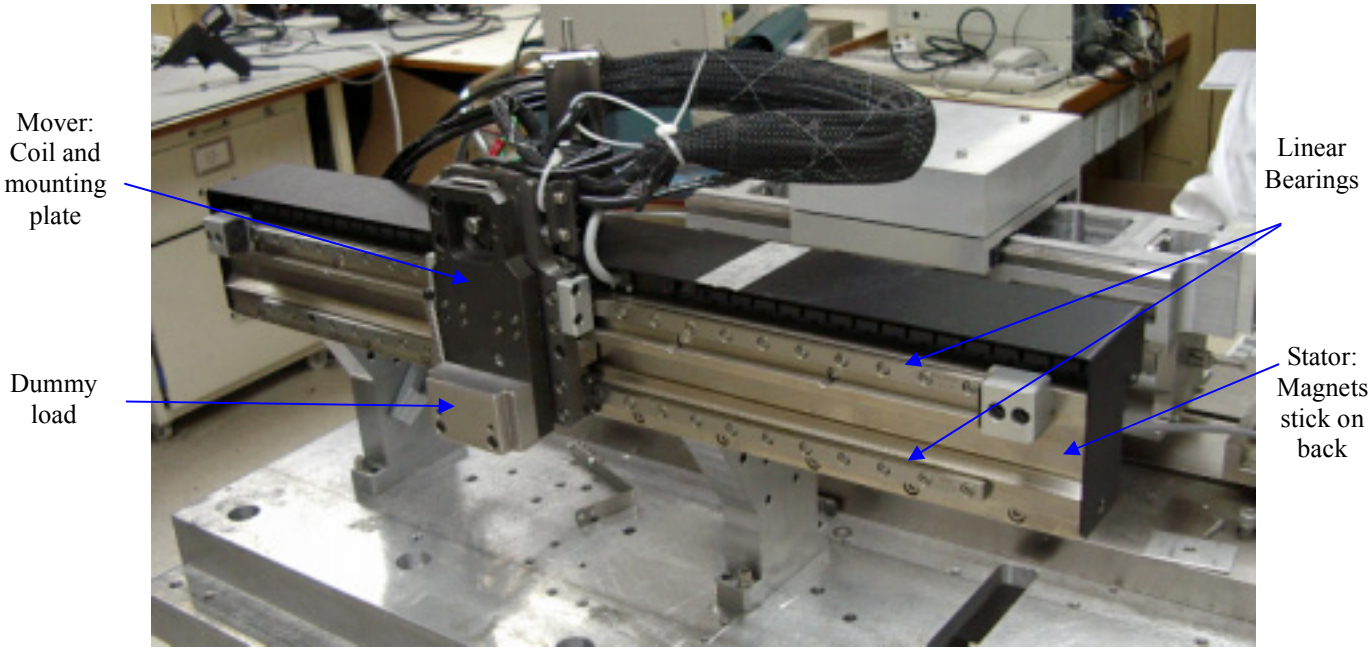

Figure 2-7 Overview of the LPMSM

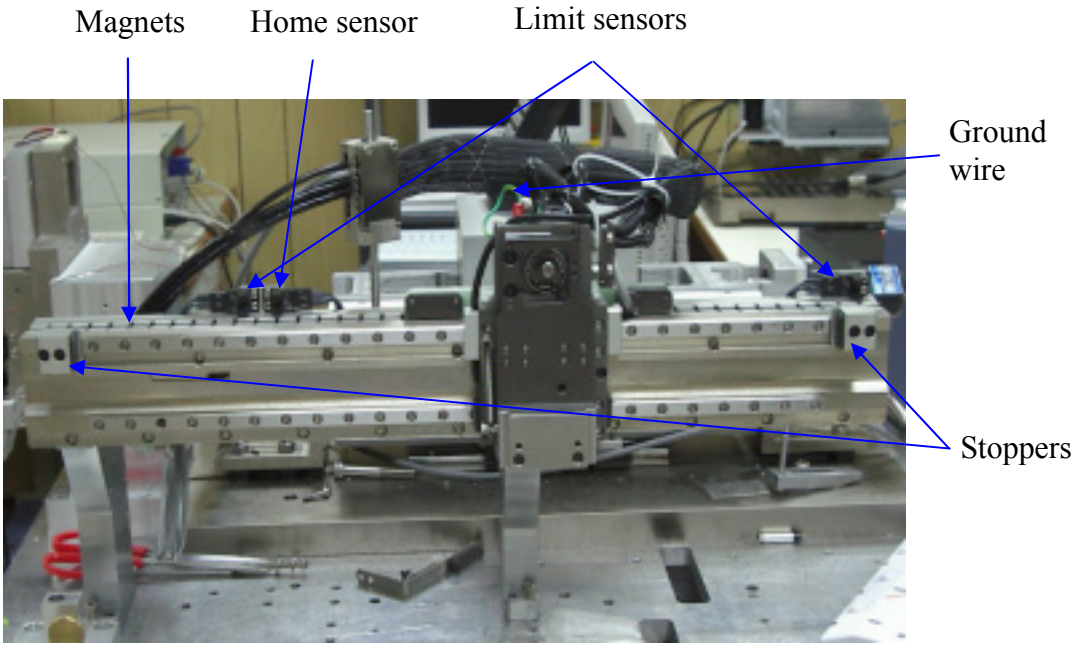

Figure 2-8 Limit sensors and stoppers on the LPMSM

On removing the cover, there are the home sensor and the limit sensors as shown in Figure 2-8. The home sensor is to detect if the mover is at the defined home position. It is always mounted at one end of the motor, and is at the location before the mover hits one of the limit sensors – the left side limit sensor in this motor. When the system starts up, the mover is commanded to move to left to search the home position, once it is detected, the encoder value is recorded as home position value. Such value can then be regarded as a reference so that the controller knows where the mover is. If the home position can not be found in a preset traveling range, the home search action is failure. The controller can either do the search again or reports the error to the system.

The limits sensors are mounted at both end to detect if the mover is in the limit positions. When either one of the limit positions is detected, one should ramps down and stops the mover immediately.

There are also the stoppers mounted at both ends of the motor. They limit the traveling range of the mover and prevent the motor coils from moving out of the magnetic rail.

The encoder read head is mounted behind the mover to read the encoder scale that sticks on the stator as indicated in Figure 2-9.

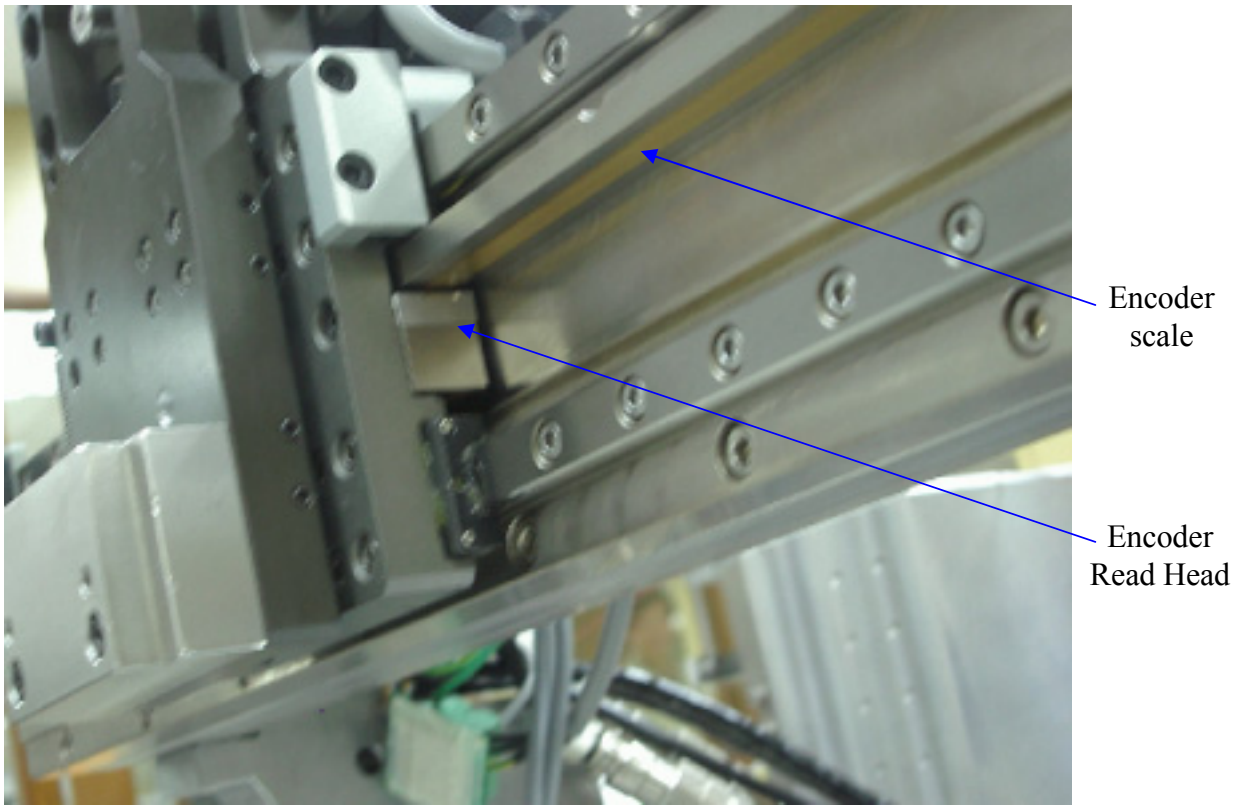

Figure 2-9 The encoder read-head and encoder scale on the LPMSM

Since the encoder read head is mounted close to the motor coils of the mover, the EMI generated in those coils due to high voltage switching can affect the encoder signals. The encoder manufacturers always put the encoder read head in a metal case for EMI shielding. The case of the encoder read head is connected to ground to avoid the signals are jammed by conductive or radiated noises. The stator of the motor is ground to ensure electrical safety and minimize EMI problem. As the mover is moving on the pair of linear bearings, ground continuity of mover is guaranteed by using a ground wire as shown in Figure 2-8. The ground wire effectively connects the mover to the ground.

The characteristics of the LPMSM are shown in Table 2-1. It is a star-connected 3-phase moving coil motor. The encoder has a resolution of 1μm. For a targeted maximum mover velocity of 2m/s, the encoder line frequency will be at 400KHz. The differential outputs of the encoder ensure high noise immunity for the high speed encoder signals.

Since the magnetic pole pitch is 2cm, if the mover is moving at a velocity of 2m/s, the frequency of the motor phase current will be at 25Hz. For a 20 times current over sampling rate, the required frequency bandwidth of driver will be 500Hz.

The motor has a force constant of 11.6N/A. When over driving the motor at 11A peak current, and mass if the mover with dummy load is 2kg, a peak acceleration of 63.8m/s^2, i.e. ~6.46G, can be achieved, where G is the gravitational acceleration (1G = 10m/s^2).

Table 2-1 The characteristics of the Linear PMSM

Parameters	**Value**	**Remark**
Motor Inductance	1.1mH	Phase-to-phase
Motor Resistance	0.9Ω	Phase-to-phase
Motor Force Constant	11.6N/A	DC equivalent value
Mover Mass	1kg	Motor coil and dummy load
Peak Current	10A	
RMS current	4A	@25°C
Encoder Resolution	1um	2.5μm line 4x interpolated to 1um resolution 5V supply RS485 differential outputs
Traveling distance	40cm	
Magnetic pole pitch	2cm	
Maximum acceleration	8G	
Maximum velocity	4m/s	
Life time	5year	<2kg load

2.2 DRIVING THE LPMSM

Since the structure of a linear motor is fundamentally different from a rotary motor, the electrical characteristics of the two motor types are different. Table 2-2 and Table 2-3 show the motor inductance and resistance of three rotary PMSMs and three linear PMSM in the power range of 50W to 200W.

Table 2-2 Inductances and Resistances of Rotary PMSM

Motor Type	Motor inductance (line-line)	Motor Resistance (line-line)
Tamagawa 50W motor	11.3mH	9.1
Tamagawa 100W motor	6.7mH	4.9
Tamagawa 200W motor	3.2mH	0.93

Table 2-3 Typical Inductances and Resistances of Linear PMSM

Motor Type	Motor inductance (line-line)	Motor Resistance (line-line)
50W motor	2.1mH	1.2
100W motor	1.5mH	2.2
200W motor	1.1mH	0.9

In this investigation, the linear motor employed is the 200W type. From the actual measurements of the electrical characteristics of the LPMSM with the RPMSM, the inductance of the linear motor (1.1mH) is about 3 times lower than that of the rotary motor. Therefore the current dynamics can be much higher. This implies that the feedback current sensor needs to have a fast response in order to track the current profile accurately, and to allow a proper control of the current loop [46]. In addition, a higher chopping frequency is needed in case of the PWM current scheme in order to maintain the current ripple to minimum. Hence, there will be compromise between the chopping frequency and switching loss of the power stage [47].

Another difference is the EMI shielding of these two types of motor. The windings of the rotary motor are already housed in the metal stator, which effectively shields and suppresses the EMI noise radiation. Since there is no metal case in the linear motor, the EMI caused by the fast switching currents and voltages can radiate out directly. Electronic system designer has to pay more attention when operating the circuitry in such noisy condition [18].

2.2.1 The Current Drive of the LPMSM

There are two possible kinds of commonly used current control methods: the hystersis control and the linear current control. The hystersis control is a bang-bang current control. A fixed drive voltage of correct polarity is applied to the load if the current does not reach the set point; else the load current either circulates via a low resistance (the power devices) or quickly discharges to the supply source. The hystersis control requires a threshold level which controls the current ripple and also the zero-dead-band of the driver [19, 20, 21].

2.2.2 PI Current Control Loop

A better scheme is to use PI controller to control the current of the motor [10, 29]. For simplicity the single-phase current control loop is discussed here. The 3-phase control is simply the addition of one active phase and one passive phase to the single-phase current

control.

The block diagram in Figure 2-10 below is a single-phase current control loop with an inductive motor load:

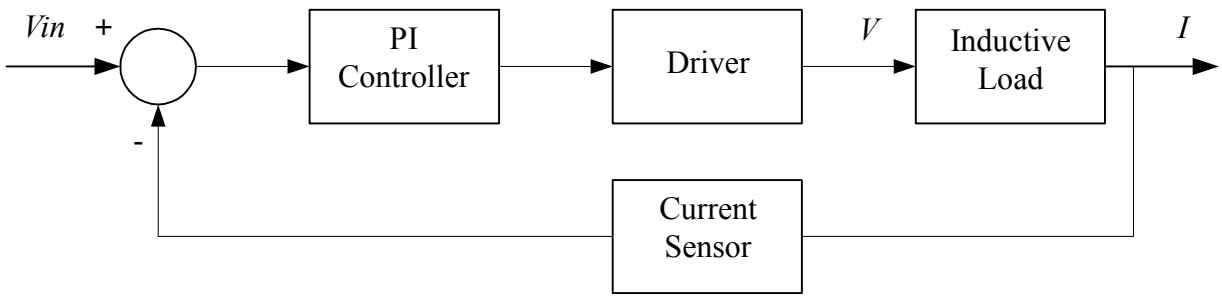

Figure 2-10 Single-phase PI current control loop

Let L_m and R_m respectively be the inductance and resistance of the inductive load, the transconductance *G(s)* of the motor load in *s* domain is given by

$$G(s) = \frac{I(s)}{V(s)} = \frac{1}{sL_m + R_m} = \frac{\frac{1}{L_m}}{s + \frac{R_m}{L_m}} \qquad \textbf{(2.13)}$$

The transfer function, *T(s)*, of the PI controller is:

$$T(s) = K_p + \frac{K_i}{s} = \frac{K_p}{s}\left(s + \frac{K_i}{K_p}\right) \qquad \textbf{(2.14)}$$

For ease of analysis, assume the transfer function of the Driver block is unity, the forward transfer function of the current loop, *C(s)*, can therefore be written as:

$$C(s) = T(s)\,G(s)$$

$$= \frac{K_p}{s}\left(s + \frac{K_i}{K_p}\right) \frac{\frac{1}{L_m}}{s + \frac{R_m}{L_m}}$$

$$= \frac{K_p}{Ls} \frac{\left(s + \frac{K_i}{K_p}\right)}{\left(s + \frac{R_m}{L_m}\right)} \qquad \textbf{(2.15)}$$

By matching $\frac{K_i}{K_p} = \frac{R_m}{L_m}$, the pole and zero of (2.15) are eliminated each other and the closed loop current transfer function $I_c(s)$ is a first order element, which can be quickly responsed:

$$I_c(s) = \frac{\frac{K_p}{L_m}}{s + \frac{K_p}{L_m}} \qquad \textbf{(2.16)}$$

If ω_n is the required bandwidth of the current loop, the K_p and K_i can be found as follows:

$$K_p = \omega_n L_m \qquad \textbf{(2.17)}$$

and

$$K_i = \omega_n R_m \qquad \textbf{(2.18)}$$

2.2.3 Application of the PI current control loop

From the equations (2.13) to (2.18) as described, the current loop using the PI control can easily be tuned to the desired value by the pole-zero cancellation technique. Also, for the space vector current control scheme (which will be discussed and employed), the tracking of the controlled variables will be a slow varying vector current profile and it is particularly suitable for the low pass characteristic of the PI controller.

From the literature in [23], it has proved that the PI current loop can tolerate up to 30% parameter variation with slight change in the current loop response. Hence the PI

controller will be employed for controlling the current of the LPMSM.

2.2.4 Block Diagram of a 3-Phase Current Drive

Based on the single PI current control loop derived in the previous section, the 3-phase current control loop can be built by using two individual single current loops with the third phase deduced by the current law: $I_a + I_b + I_c = 0$

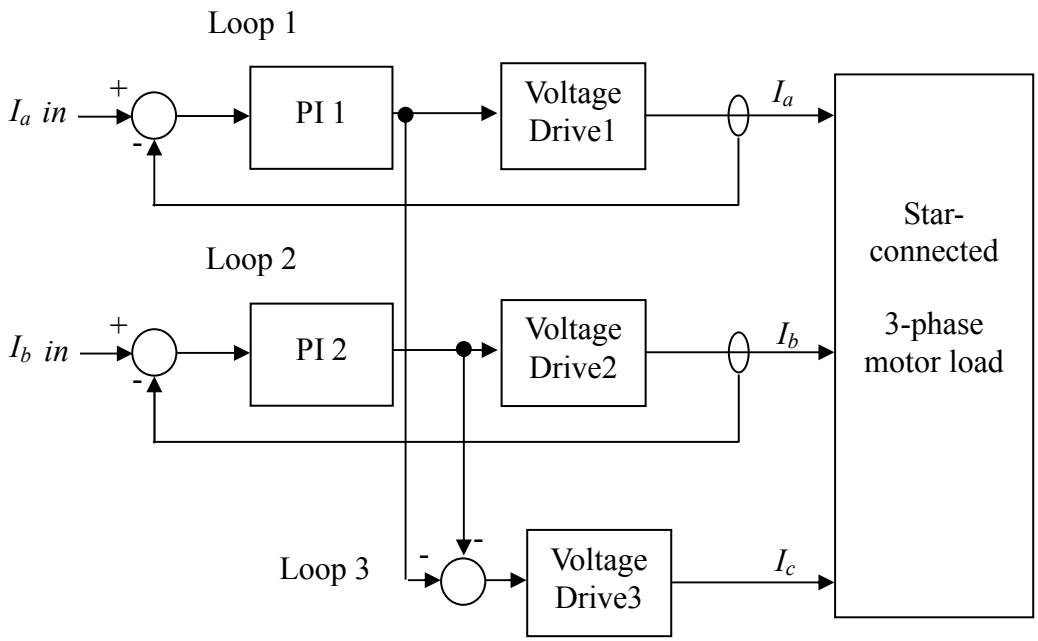

Figure 2-11 3-Phase PI current control loop

Figure 2-11 above is the 3-phase current control loop. Loop 1 and Loop 2 are two identical single phase PI current control loop. Each of them regulates the respective phase current individually. Since the motor load is a balanced 3-phase load, the voltage of the third Loop 3 is the inversion of the summation of the voltage of Loop 1 and Loop 2. The Loop 3 is actually a passive loop, which performs the inverted voltage summation of the Loop 1 and Loop 2 in order to balance the zero current summation of the 3-phase motor loop. Therefore, the gain of the Voltage Drive1, Voltage Drive2 and Voltage Drive3 is the same.

As can be seen only two current sensors are needed for the current control of the 3-phase motor.

2.3 VECTOR CONTROL THEORY FOR THE LPMSM

Equation (2.10) involves three current variables, it is always preferable to transform the current variables into a form that is more convenient for the motion controller. In the subsequent section, the generalized model of an electrical machine is developed [4, 17].

2.3.1 General Model of the Electrical Machine

With a suitable co-ordinate transformation, an electrical machine can be represented by the basic 2-coil model [30]: one on the Direct Axis (d) and the other on the Quadrature Axis (q). See Figure 2-12 below. The q-axis spatially leads the d-axis by 90°.

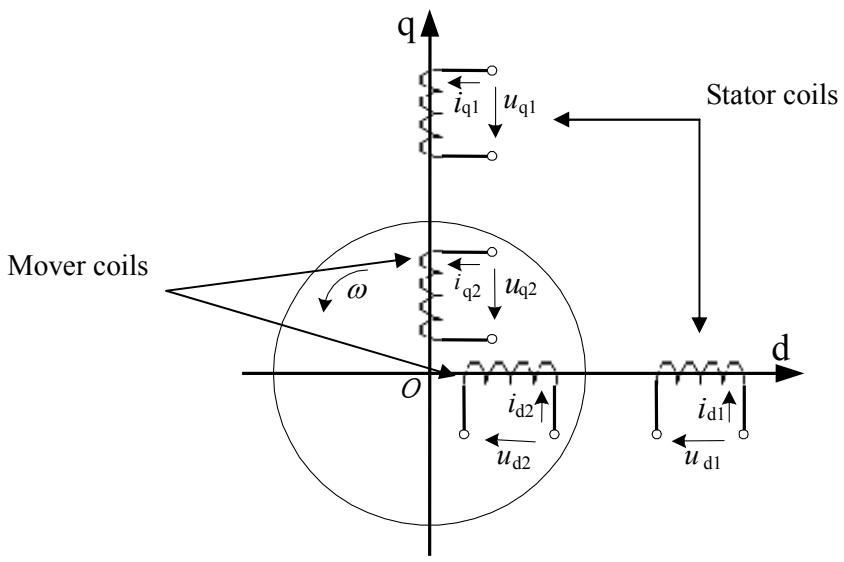

Figure 2-12 Generalized electrical machine

Both the mover and stator coils are split into two components, one on the d-axis and the other on the q-axis. There are no mutual inductance between the coils on the d-axis and q-axis [31].

In the following analysis, it is assumed that:

(i) The magnetic circuit is not operated in the saturation region and is linear,

(ii) Iron loss is small enough to be ignored as compared to copper loss, and

(iii) The MMF and magnetic flux is sinusoidally distributed [27].

The convention of the vector variables are defined as:

(i) The positive direction of the d-axis aligns with the main magnetic flux. The q-axis leads d-axis by an electrical angle of 90°.

(ii) The positive direction of the magnetic flux linkage and magnetic flux aligns with the y and x coordinate axis respectively.

(iii) The current direction is positive when the produced magnetic flux linkage is positive.

By converting the linear motion to the angular electrical angle, the forward motion is the positive direction of the electro-magnetic torque follows positive anti-clockwise rotation of the machine. The positive direction of other torque is reverse of the electro-magnetic torque.

With the above definitions, the magnetic linkage equations of electrical machine in Figure 2-12 can be written as:

$$\psi_{d1} = L_{d1} i_{d1} + L_{d12} i_{d2} \quad \textbf{(2.19)}$$

$$\psi_{q1} = L_{q1} i_{q1} + L_{q12} i_{q2} \quad \textbf{(2.20)}$$

$$\psi_{d2} = L_{d21} i_{d1} + L_{d2} i_{d2} \quad \textbf{(2.21)}$$

$$\psi_{q2} = L_{q21} i_{q1} + L_{q2} i_{q2} \quad \textbf{(2.22)}$$

Subscript 1 is for the stator while 2 is for the mover, ψ_{d1}, ψ_{q1}, ψ_{d2}, ψ_{q} are the respective total magnetic flux linkages and L_{d1}, L_{q1}, L_{d2}, L_{q2} are the respective self inductance and

L_{d12}, L_{d21}, L_{q12}, L_{q21} are the mutual inductance of the coils.

As the spatial displacement of the coils are fixed, their self and mutual inductances are constant and equal regardless where the mover is [31],

i.e. $L_{d12} = L_{d21}$, $L_{q12} = L_{q21}$

The voltage equations can be expressed as

$$u_{d1} = R_{d1} i_{d1} + p\psi_{d1} \tag{2.23}$$

$$u_{q1} = R_{q1} i_{q1} + p\psi_{q1} \tag{2.24}$$

$$u_{d2} = R_{d2} i_{d2} + p\psi_{d2} + \omega\psi_{q2} \tag{2.25}$$

$$u_{q2} = R_{q2} i_{q2} + p\psi_{q2} - \omega\psi_{d2} \tag{2.26}$$

where u_{d1}, u_{q1}, u_{d2}, u_{q2} are the voltage drops of the coils and

R_{d1}, R_{q1}, R_{d2}, R_{q2} are the resistance of the coils,

$p = d/dt$ is the differential operator；

ω is the angular velocity that cut the sinusoidal magnetic flux, $\omega = p_n \Omega$,

p_n is the magnetic pole pairs, and Ω is the angular velocity of the mover.

In the voltage equations of the mover, the transformer voltage ($p\psi_{d2}$, $p\psi_{q2}$) and the velocity back EMF ($\omega\psi_{q2}$, $\omega\psi_{d2}$) are created due to the motion of the mover.

Putting (2.19)~(2.22) into (2.23)~(2.26)，the following matrix equation is obtained:

$$\begin{bmatrix} u_{d1} \\ u_{q1} \\ u_{d2} \\ u_{q2} \end{bmatrix} = \begin{bmatrix} R_{d1} + L_{d1}p & 0 & L_{d12}p & 0 \\ 0 & R_{q1} + L_{q1}p & 0 & L_{q12}p \\ L_{d21}p & \omega L_{q21} & R_{d2} + L_{d2}p & \omega L_{q2} \\ -\omega L_{d21} & L_{q21}p & -\omega L_{d2} & R_{q2} + L_{q2}p \end{bmatrix} \begin{bmatrix} i_{d1} \\ i_{q1} \\ i_{d2} \\ i_{q2} \end{bmatrix} \tag{2.27}$$

(2.27) can be simplified as

$$u = Zi \qquad \textbf{(2.28)}$$

Where:

u is the voltage column vector, $\boldsymbol{u} = \begin{bmatrix} u_{d1} \\ u_{q1} \\ u_{d2} \\ u_{q2} \end{bmatrix}$,

i is the current column vector, $\boldsymbol{i} = \begin{bmatrix} i_{d1} \\ i_{q1} \\ i_{d2} \\ i_{q2} \end{bmatrix}$,

Z is the impedance matrix，

$$Z = \begin{bmatrix} R_{d1} + L_{d1}p & 0 & L_{d12}p & 0 \\ 0 & R_{q1} + L_{q1}p & 0 & L_{q12}p \\ L_{d21}p & \omega L_{q21} & R_{d2} + L_{d2}p & \omega L_{q2} \\ -\omega L_{d21} & L_{q21}p & -\omega L_{d2} & R_{q2} + L_{q2}p \end{bmatrix} \qquad \textbf{(2.29)}$$

The impedance matrix Z can be decomposed into

$$Z = R + Lp + \omega G$$

Where

$$R = \begin{bmatrix} R_{d1} & 0 & 0 & 0 \\ 0 & R_{q1} & 0 & 0 \\ 0 & 0 & R_{d2} & 0 \\ 0 & 0 & 0 & R_{q2} \end{bmatrix}, \quad L = \begin{bmatrix} L_{d1} & 0 & L_{d12} & 0 \\ 0 & L_{q1} & 0 & L_{q12} \\ L_{d21} & 0 & L_{d2} & 0 \\ 0 & L_{q21} & 0 & L_{q2} \end{bmatrix}, \text{ and}$$

$$G = \begin{bmatrix} 0 & 0 & 0 & 0 \\ 0 & 0 & 0 & 0 \\ 0 & L_{q21} & 0 & L_{q2} \\ -L_{d21} & 0 & -L_{d2} & 0 \end{bmatrix},$$

The voltage equations can thus be written as:

$$u = Ri + Lpi + \omega Gi \qquad \textbf{(2.30)}$$

The instantaneous power input of the electrical machine is

$$\boldsymbol{i}^{\mathbf{T}}u = \boldsymbol{i}^{\mathbf{T}}Ri + \boldsymbol{i}^{\mathbf{T}}L\mathbf{p}i + \boldsymbol{i}^{\mathbf{T}}\omega G\boldsymbol{i} \qquad \textbf{(2.31)}$$

In the above equation, the first terms in the right hand side is the resistive loss, the second is the rate of magnetic stored energy, and the third term is the power output of the machine. Therefore, the mechanical power output can be written as:

$$P_{\mathbf{mech}} = \omega \boldsymbol{i}^{\mathbf{T}}Gi \qquad \textbf{(2.32)}$$

Putting $\boldsymbol{i}^{\mathrm{T}}$、$\boldsymbol{I}$ and $\boldsymbol{G}$ into(2.32), then

$$P_{\mathbf{mech}} = \omega(\psi_{q2}i_{d2} - \psi_{d2}i_{q2}) \qquad \textbf{(2.33)}$$

Electrical force F_e is

$$F_e = \frac{P_{mech}}{\Omega} = p_n(\psi_{q2}i_{d2} - \psi_{d2}i_{q2}) \qquad \textbf{(2.34)}$$

Let F_{e} be the electrical force from motor, F_{L} be the loading force, R_{Ω} be damping factor and $R_{\Omega}\Omega$ be the system damping force, M is total mass of the mover and load, the motion system of the mechanical system can be written as:

$$M\frac{dv}{dt} = F_e - F_L - R_{\Omega}\Omega \qquad \textbf{(2.35)}$$

The previously derived equations of magnetic flux linkage, voltage, force and mechanical motion, are called the united equation of electrical machine [30]. The magnetic flux linkage and voltage equations are called the Park equations [31].

2.3.2 *Coordinate Transformation*

For the convenience of analysis, the equations of the electrical machine are often expressed by the following co-ordination transformation [31]: the 3-phase coordinate system of the static 3-phase winding is labeled as *abc* while the static 2-phase coordinate system is labeled as α-β.

The α-axis aligns with the *a*-axis, β-axis leads α-axis by an electrical angle of 90°. The coordinate system that synchronizes with the rotating magnetic flux is defined as *d-q.* The relationship between the three coordinate systems are shown in Figure 2-13

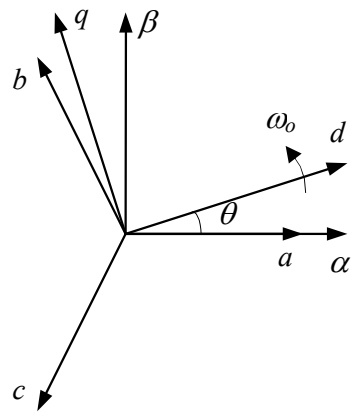

Figure 2-13 The *abc*, *dq* and $\alpha\beta$ coordinate systems

$$\theta = \int \omega_0 dt + \theta_0 \qquad \textbf{(2.36)}$$

Where ω_0 is the synchronous rotating speed of the *d-q* system

θ_0 is the initial angular position.

There are two kinds of coordinate transformation systems: one is the power-invariant coordinate transformation while the other power-variant transformation required a multiplier factor for the transformed power equations [31].

2.3.2.1 *Power-Invariant Coordinate Transform*

For the transformation between the static 3-phase *abc* and 2-phase α-β coordinate system, takes the currents transformation as example, the relationship between the *abc* and α-β coordinate is as follows:

$$\begin{bmatrix} i_\alpha \\ i_\beta \\ i_0 \end{bmatrix} = \sqrt{\frac{2}{3}} \begin{bmatrix} 1 & -\frac{1}{2} & -\frac{1}{2} \\ 0 & \frac{\sqrt{3}}{2} & -\frac{\sqrt{3}}{2} \\ \frac{1}{\sqrt{2}} & \frac{1}{\sqrt{2}} & \frac{1}{\sqrt{2}} \end{bmatrix} \begin{bmatrix} i_a \\ i_b \\ i_c \end{bmatrix} \qquad \textbf{(2.37)}$$

For 3-phase 3 wire system, there is the current relation of $i_a + i_b + i_c \equiv 0$,

So $i_0 \equiv 0$, and the previous equation can be simplified as:

$$\begin{bmatrix} i_\alpha \\ i_\beta \end{bmatrix} = \sqrt{\frac{2}{3}} \begin{bmatrix} 1 & -\frac{1}{2} & -\frac{1}{2} \\ 0 & \frac{\sqrt{3}}{2} & -\frac{\sqrt{3}}{2} \end{bmatrix} \begin{bmatrix} i_a \\ i_b \\ i_c \end{bmatrix} \qquad \textbf{(2.38)}$$

Hence, the coordinate matrix transformation from *abc* system to α-β system is

$$C_{abc-\alpha\beta} = \sqrt{\frac{2}{3}} \begin{bmatrix} 1 & -\frac{1}{2} & -\frac{1}{2} \\ 0 & \frac{\sqrt{3}}{2} & -\frac{\sqrt{3}}{2} \end{bmatrix}, \text{ or } C_{abc-\alpha\beta} = \sqrt{\frac{2}{3}} \begin{bmatrix} 1 & -\frac{1}{2} & -\frac{1}{2} \\ 0 & \frac{\sqrt{3}}{2} & -\frac{\sqrt{3}}{2} \\ \frac{1}{\sqrt{2}} & \frac{1}{\sqrt{2}} & \frac{1}{\sqrt{2}} \end{bmatrix} \qquad \textbf{(2.39)}$$

Hence, the coordinate matrix transformation from α-β system to *abc* system is

$$C_{\alpha\beta-abc} = \sqrt{\frac{2}{3}} \begin{bmatrix} 1 & 0 \\ -\frac{1}{2} & \frac{\sqrt{3}}{2} \\ -\frac{1}{2} & -\frac{\sqrt{3}}{2} \end{bmatrix}, \text{ or } C_{\alpha\beta-abc} = \sqrt{\frac{2}{3}} \begin{bmatrix} 1 & 0 & \frac{1}{\sqrt{2}} \\ -\frac{1}{2} & \frac{\sqrt{3}}{2} & \frac{1}{\sqrt{2}} \\ -\frac{1}{2} & -\frac{\sqrt{3}}{2} & \frac{1}{\sqrt{2}} \end{bmatrix} \qquad \textbf{(2.40)}$$

While the matrix coordinates transformation between static 2-phase α-β and rotating *d-q* is given by:

$$C_{\alpha\beta-dq} = \begin{bmatrix} \cos\theta & \sin\theta \\ -\sin\theta & \cos\theta \end{bmatrix} \tag{2.41}$$

The matrix coordinates transformation of *d-q* to α-β is given by

$$C_{dq-\alpha\beta} = \begin{bmatrix} \cos\theta & -\sin\theta \\ \sin\theta & \cos\theta \end{bmatrix} \tag{2.42}$$

For the transformation between synchronous rotating *d-q* system and static *abc* system, the transformation from *abc* to *d-q* is given by:

$$C_{abc-dq} = \sqrt{\frac{2}{3}} \begin{bmatrix} \cos\theta & \cos\left(\theta - \frac{2\pi}{3}\right) & \cos\left(\theta + \frac{2\pi}{3}\right) \\ -\sin\theta & -\sin\left(\theta - \frac{2\pi}{3}\right) & -\sin\left(\theta + \frac{2\pi}{3}\right) \end{bmatrix} \tag{2.43}$$

or

$$C_{abc-dq} = \sqrt{\frac{2}{3}} \begin{bmatrix} \cos\theta & \cos\left(\theta - \frac{2\pi}{3}\right) & \cos\left(\theta + \frac{2\pi}{3}\right) \\ -\sin\theta & -\sin\left(\theta - \frac{2\pi}{3}\right) & -\sin\left(\theta + \frac{2\pi}{3}\right) \\ \frac{1}{\sqrt{2}} & \frac{1}{\sqrt{2}} & \frac{1}{\sqrt{2}} \end{bmatrix} \tag{2.44}$$

Similarly, the transformation matrix from *d-q* to *abc* can be found by (2.43) and (2.44) as

$$C_{dq-abc} = \sqrt{\frac{2}{3}} \begin{bmatrix} \cos\theta & -\sin\theta \\ \cos\left(\theta - \frac{2\pi}{3}\right) & -\sin\left(\theta - \frac{2\pi}{3}\right) \\ \cos\left(\theta + \frac{2\pi}{3}\right) & -\sin\left(\theta + \frac{2\pi}{3}\right) \end{bmatrix} \tag{2.45}$$

or

$$C_{dq-abc} = \sqrt{\frac{2}{3}} \begin{bmatrix} \cos\theta & -\sin\theta & \frac{1}{\sqrt{2}} \\ \cos\left(\theta - \frac{2\pi}{3}\right) & -\sin\left(\theta - \frac{2\pi}{3}\right) & \frac{1}{\sqrt{2}} \\ \cos\left(\theta + \frac{2\pi}{3}\right) & -\sin\left(\theta + \frac{2\pi}{3}\right) & \frac{1}{\sqrt{2}} \end{bmatrix} \quad \textbf{(2.46)}$$

Note that the above transformation can be applied to voltages, current and magnetic flux linkage. To satisfy the power-invariant condition, it can be proved that the effective no of turn for the *d-q* coils is $\sqrt{\frac{3}{2}}$ times the original *abc* coils.

The relationship between the parameters of the *d-q* axis and the original *abc* are as follows:

$$\boldsymbol{R = R_a}, \quad \boldsymbol{L = \frac{3}{2} L_a}, \quad \boldsymbol{K_E = \sqrt{\frac{3}{2}}\, K_{E3}} \quad \textbf{(2.47)}$$

For the above equations, left hand sides are the d-q parameters and the right hand sides are the original 3-phase parameters, K_E is the back EMF constant. If the original 3-phase system is in balanced condition, the corresponding transformed *d-q* parameter will have constant values of $\sqrt{3}$ times the 3-phase system [31].

2.3.2.2 Power Variant Coordinate Transform

Since there are the "square root" mathematical operation existing in the power-invariant transform, this can introduce many inconvenient in software programming of the control system and can affect the accuracy. Hence, the power-variant transformation is usually adopted in practice and also in this research project.

The respective power-variant coordinate transformation is as follows:

$$C'_{abc-\alpha\beta} = \frac{2}{3} \begin{bmatrix} 1 & -\frac{1}{2} & -\frac{1}{2} \\ 0 & \frac{\sqrt{3}}{2} & -\frac{\sqrt{3}}{2} \\ \frac{1}{2} & \frac{1}{2} & \frac{1}{2} \end{bmatrix} \quad \textbf{(2.48)}$$

$$C'_{\alpha\beta-abc} = \begin{bmatrix} 1 & 0 & 1 \\ -\frac{1}{2} & \frac{\sqrt{3}}{2} & 1 \\ -\frac{1}{2} & -\frac{\sqrt{3}}{2} & 1 \end{bmatrix} \quad \textbf{(2.49)}$$

$$C'_{\alpha\beta-dq} = \begin{bmatrix} \cos\theta & \sin\theta \\ -\sin\theta & \cos\theta \end{bmatrix} \quad \textbf{(2.50)}$$

$$C'_{dq-\alpha\beta} = \begin{bmatrix} \cos\theta & -\sin\theta \\ \sin\theta & \cos\theta \end{bmatrix} \quad \textbf{(2.51)}$$

$$C'_{abc-dq} = \frac{2}{3}\begin{bmatrix} \cos\theta & \cos\left(\theta-\frac{2\pi}{3}\right) & \cos\left(\theta+\frac{2\pi}{3}\right) \\ -\sin\theta & -\sin\left(\theta-\frac{2\pi}{3}\right) & -\sin\left(\theta+\frac{2\pi}{3}\right) \\ \frac{1}{2} & \frac{1}{2} & \frac{1}{2} \end{bmatrix} \quad \textbf{(2.52)}$$

$$C'_{dq-abc} = \begin{bmatrix} \cos\theta & -\sin\theta & 1 \\ \cos\left(\theta-\frac{2\pi}{3}\right) & -\sin\left(\theta-\frac{2\pi}{3}\right) & 1 \\ \cos\left(\theta+\frac{2\pi}{3}\right) & -\sin\left(\theta+\frac{2\pi}{3}\right) & 1 \end{bmatrix} \quad \textbf{(2.53)}$$

Where (2.52) is called Park Transform and (2.53) the Inverse Park Transform [2].

The power relationship is as follows:

$$\begin{aligned} \text{Power} &= u_a i_a + u_b i_b + u_c i_c \\ &= (3/2)(u_\alpha i_\alpha + u_\beta i_\beta + 2u_0 i_0) \\ &= (3/2)(u_d i_d + u_q i_q + 2u_0 i_0) \end{aligned} \quad \textbf{(2.54)}$$

2.3.3 Space-Vector Pulse-Width Modulation Scheme

As described in the previous sections, the Space Vector PWM drive scheme has better voltage utilization and it also allows the field-weakening technique [19] to be implemented for high-speed application. Therefore, this form of PWM generation scheme is adopted in the project.

The Space Vector motor current control theory as described in the previous section can be implemented digitally by the modern DSP system. The Figure 2-14 is the 3-phase power-bridge for drive the 3-phase permanent magnet synchronous motor. V_a, V_b and V_c are the output voltages of the inverter. Q1 through Q6 are the six power transistors that shape the output and they are controlled by their respective inputs a, a', b, b', c and c' (a "1" means an ON and "0" means OFF). The turn off of any power transistor can be at any time. Before a transistor is tuned on, the other transistor of the same half-bridge must be turned off to avoid shoot-through occurs and damaging the power transistor.

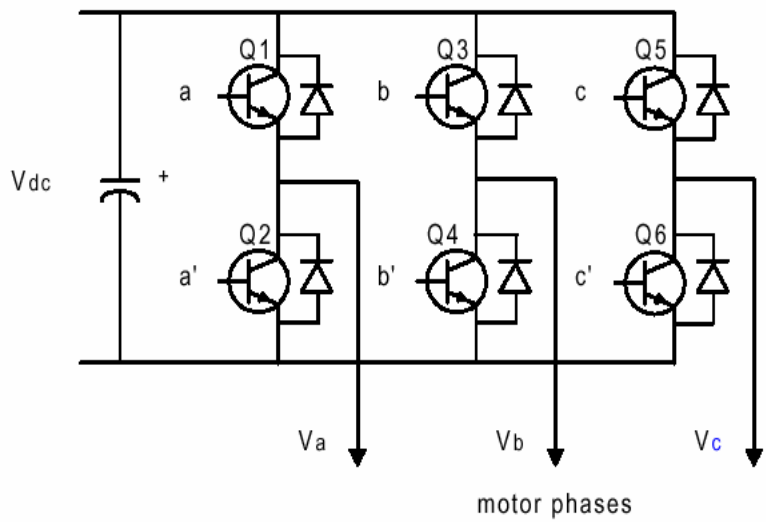

Figure 2-14 The 3-phase power bridge for motor drive

The relationship between the input switching variable vector $[a\ b\ c]^t$ and the line-to-line output voltage vector $[V_{ab}\ V_{bc}\ V_{ca}]^t$ and the phase (line-to-neutral) output voltage vector $[V_a\ V_b\ V_c]^t$ is given by equations below:

$$\begin{bmatrix} V_{ab} \\ V_{bc} \\ V_{ca} \end{bmatrix} = V_{dc} \begin{bmatrix} 1 & -1 & 0 \\ 0 & 1 & -1 \\ -1 & 0 & 1 \end{bmatrix} \begin{bmatrix} a \\ b \\ c \end{bmatrix} \qquad \textbf{(2.55)}$$

$$\begin{bmatrix} V_a \\ V_b \\ V_c \end{bmatrix} = \frac{1}{3} V_{dc} \begin{bmatrix} 2 & -1 & -1 \\ -1 & 2 & -1 \\ -1 & -1 & 2 \end{bmatrix} \begin{bmatrix} a \\ b \\ c \end{bmatrix} \qquad \textbf{(2.56)}$$

The eight possible combinations of the on and off states for the three upper power transistors are shown in the table below: The eight combinations and their derived output line-to-line and phase voltages in terms of DC supply voltage V_{dc}, according to (2.55) and (2.56) are shown in the Figure 2-15.

The Space Vector (SV) PWM refers to a special way of determining the switching sequence of the upper three power transistors of a three-phase power bridge. It generates less harmonic distortion in the output voltages and currents in the motor windings and provides more efficient use of DC supply voltage, in comparison to direct sinusoidal modulation technique. [19]

a	***b***	***c***	v_a	v_b	v_c	v_{ab}	v_{bc}	v_{ca}
0	0	0	0	0	0	0	0	0
1	0	0	2/3	-1/3	-1/3	1	0	-1
1	1	0	1/3	1/3	-2/3	0	1	-1
0	1	0	-1/3	2/3	-1/3	-1	1	0
0	1	1	-2/3	1/3	1/3	-1	0	1
0	0	1	-1/3	-1/3	2/3	0	-1	1
1	0	1	1/3	-2/3	1/3	1	-1	0
1	1	1	0	0	0	0	0	0

Figure 2-15 Device on/off states and corresponding outputs of a 3-phase bridge

Assume d and q are the fixed horizontal and vertical axes in the plane of the three motor phases. The vector respresentations of the phase voltages corresponding to the eight combinations can be obtained by applying the following d-q transformation to the phase voltages:

$$\begin{bmatrix} V_a \\ V_b \\ V_c \end{bmatrix} T_{abc-dq} = \sqrt{\frac{2}{3}} \begin{bmatrix} 1 & -\frac{1}{2} & -\frac{1}{2} \\ 0 & \frac{\sqrt{3}}{2} & -\frac{\sqrt{3}}{2} \end{bmatrix} \qquad \textbf{(2.57)}$$

This transformation is equivalent to an orthogonal projection of [*a, b, c*]**t** onto the two dimensional plane perpendicular to the vector [1, 1, 1]**t** in a three-dimensional coordinate

system, the results of which are six non-zero vectors and two zero vectors as shown in Figure 2-16. The non-zero vectors is 60°. The zero vectors are at the origin and apply zero voltage to a three-phase load. The eight vectors are called the Basic Space Vectors and are demoted here by $\mathbf{U_0}$, $\mathbf{U_{60}}$, $\mathbf{U_{120}}$, $\mathbf{U_{180}}$, $\mathbf{U_{240}}$, $\mathbf{U_{300}}$, $\mathbf{O_{000}}$ and $\mathbf{O_{111}}$.

The same d-q transformation can be applied to a desired three-phase voltage output to obtain a desired reference voltage vector $\mathbf{U_{out}}$ in the d-q plane as shown in Figure 2-16. The magnitude of $\mathbf{U_{out}}$ is the rms value of the corrseponding line-to-line voltage with the defined d-q transform.

The objective of the Space Vector PWM technnique is to approximate the reference voltage $\mathbf{U_{out}}$ instantaneously by combining the switching states that correspond to the basic space vector. To achieve this, for any small period of time T, the average inverter output can be the same as the average reference voltage $\mathbf{U_{out}}$ as shown in (2.58). T_1 and T_2 in the equation are the respective durations for which switching states corresponding to $\boldsymbol{U_x}$ and $\mathbf{U_{x+60}}$ (or $\mathbf{U_{x-60}}$) are applied. $\mathbf{U_x}$ and $\mathbf{U_{x+60}}$ (or $\mathbf{U_{x-60}}$) are the basic space vectors that form the sector containing $\mathbf{U_{out}}$. However, if we assume that the change in reference voltage of $\mathbf{U_{out}}$ is tiny within T, then (2.58) becomes (2.59) where $T_1 + T_2 \leq T$. Therefore, it is critical that T should be small with respect to the speed if change of $\mathbf{U_{out}}$. In practice the approximation is done for every PWM period, T_{PWM}. Therefore it is critical that the PWM period should be small with respect to the speed of change of $\mathbf{U_{out}}$.

$$\frac{1}{T}\int_{nT}^{(n+1)T} \mathbf{U_{out}}(t) = \frac{1}{T}(T_1\mathbf{U_x} + T_2\mathbf{U_{x\pm 60}}) \qquad (2.58)$$

$$\mathbf{U_{out}}(nT) = \frac{1}{T}(T_1\mathbf{U_x} + T_2\mathbf{U_{x\pm 60}}) \qquad (2.59)$$

The above equations (2.58) and (2.59) mean that for every PWM period, $\boldsymbol{U_{out}}$ can be approximated by having the inverter in switching states $\mathbf{U_x}$ and $\mathbf{U_{x+60}}$ (or $\mathbf{U_{x-60}}$) for T_1 and T_2 duration of time respectively.

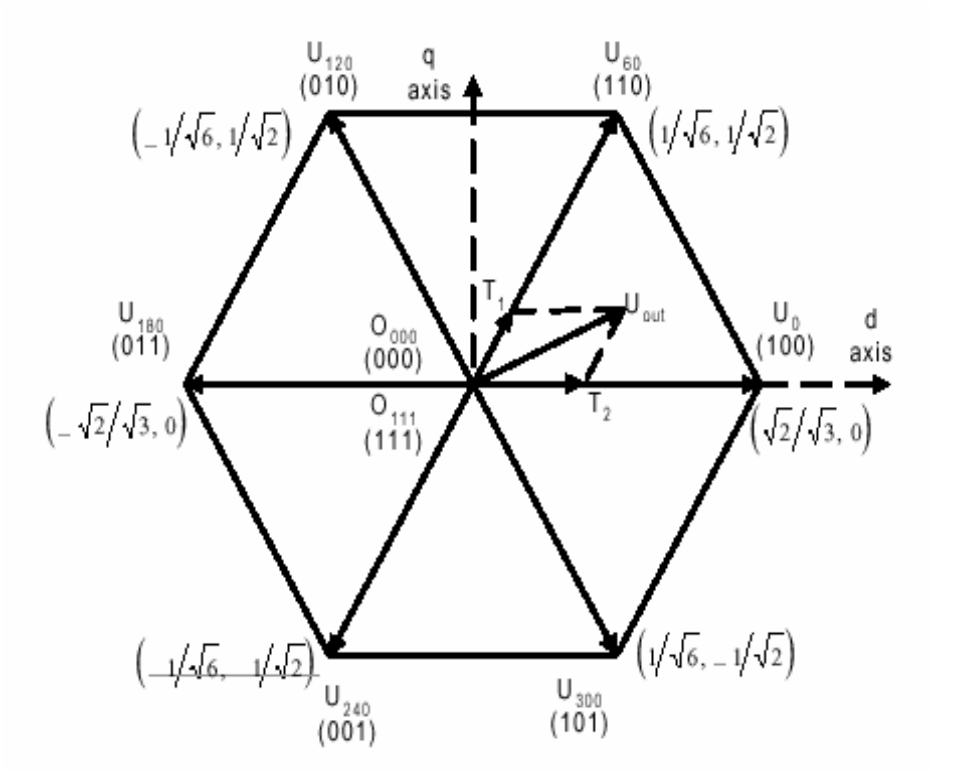

Figure 2-16 Basic Space Vectors (Normalized w.r.t. V_{dc}) and Switching States

Since the sum of T_1 and T_2 should be less than or equal to T_{PWM}, the inverter needs to be in $\mathbf{O_{000}}$ or $\mathbf{O_{111}}$ state for the rest of the period. Therefore, the equations (2.58) and (2.59) becomes (2.60) in the following, where $T_1 + T_2 + T_0 = T_{PWM} = T$.

$$T_{PWM}\mathbf{U_{out}} = T_1\mathbf{U_x} + T_2\mathbf{U_{x\pm60}} + T_0(\mathbf{O_{000}} \text{ or } \mathbf{O_{111}}) \qquad (2.60)$$

The above equation can further be re-writen as:

$$[T_1\ T_2]^t = T_{PWM}[\mathbf{U_x}\ \mathbf{U_{x\pm60}}]^{-1}\mathbf{U_{out}} \qquad (2.61)$$

where $[\mathbf{U_x}\ \mathbf{U_{x\pm60}}]^{-1}$ is the normalized decomposition matrix for the sector.

Assume the angle between $\mathbf{U_{out}}$ and $\mathbf{U_x}$ is α, from the space vector switching state diagram, the equation can be obtained for T_1 and T_2.

$$T_1 = \sqrt{2}T_{PWM}\|\mathbf{U_{out}}\|\cos(\alpha + 30^\circ) \qquad (2.62)$$

$$T_2 = \sqrt{2}T_{PWM}\|\mathbf{U_{out}}\|\sin(\alpha) \qquad (2.63)$$

Depending on the specific application, the calculation of T_1 and T_2 can be done either with (2.61) or (2.62)~(2.63). (2.61) is sector dependent. However, the matrix inverse can be calculated off-line for each sector and obtained via a look-up table during on-line calculation. This approach is useful when $\mathbf{U_{out}}$ is given in the form of vector $[\mathbf{U_d}, \mathbf{U_q}]^t$. (2.62)~(2.63) are independent of sector and is useful when $\mathbf{U_{out}}$ is given in the form of Magnitude and phase angle.

$\mathbf{U_x}$ can be the closest basic space vector on either side of $\mathbf{U_{out}}$. $\mathbf{U_{x+60}}$ *(or* $\mathbf{U_{x-60}}$*)* is then the basic space vector on the opposite side. In either case, T_1 represents the component on $\mathbf{U_x}$, T_2 represents the component on the other basic space vector.

2.4 THE POSITION CONTROL OF THE LINEAR DRIVER SYSTEM

The block diagram in Figure 2-17 is the traditional PID controller for position control application.

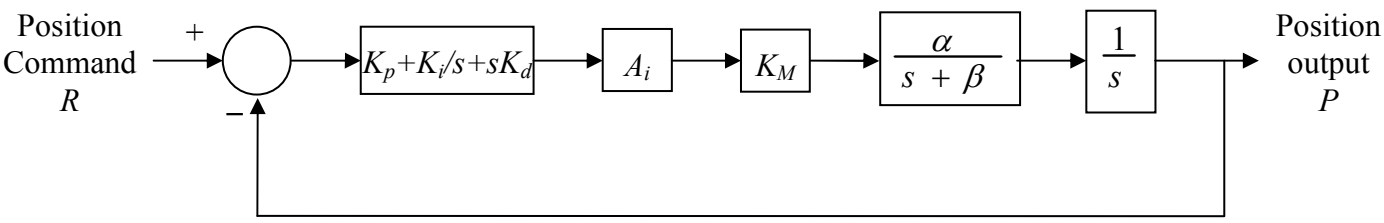

Figure 2-17 A traditional PID control system

The terms K_p, K_i, and K_d are the proportional, integral and derivative gain of the PID controller respectively. The term A_i is the current gain of the power driver and K_M is the motor force constant, and they are combined as A. The function $\frac{\alpha}{s+\beta}$ is the mechanical model of the motor where α is the inverse of the mechanical mass M i.e. $\frac{1}{M}$; while β equals to $\frac{K_{vf}}{M}$ with K_{vf} is the dynamic friction coefficient of the motor. For simplicity, the K_i term is ignored and the transfer function of the PID control system can be written as

follow:

$$\frac{P}{R}=\frac{(K_P+sK_d)A\frac{\alpha}{s+\beta}\frac{1}{s}}{1+(K_P+sK_d)A\frac{\alpha}{s+\beta}\frac{1}{s}} \tag{2.64}$$

By setting $\beta=\frac{K_P}{K_d}$

$$\frac{P}{R}=\frac{K_d A\alpha\frac{1}{s}}{1+K_d A\alpha\frac{1}{s}}=\frac{P}{R}=\frac{K_d A\alpha}{s+K_d Aa} \tag{2.65}$$

By using the pole-zero cancellation method, the transfer function can be reduced to first order form as (2.65). The system can be turned to the desired dynamic response if the load and friction of the system are known. The PID controller will be built for benchmarking of the linear drive system. The results will be used to compare with the robust controller which will be described in subsequent section.

CHAPTER THREE A HIGH-PERFORMANCE FULLY DIGITAL ROBUST DRIVE FOR LPMSM SYSTEM

In this chapter, the author has developed a set of non-traditional driving techniques for the LPMSM drive system. These include:

(i) Profile generation

(ii) Robust disturbance Compensated Controller

(iii) An All-Digital PWM Drive

3.1 PROFILE GENERATION

The block diagram in Figure 3-1 is a typical PID position control system with a Profile Generation block added at the input stage.

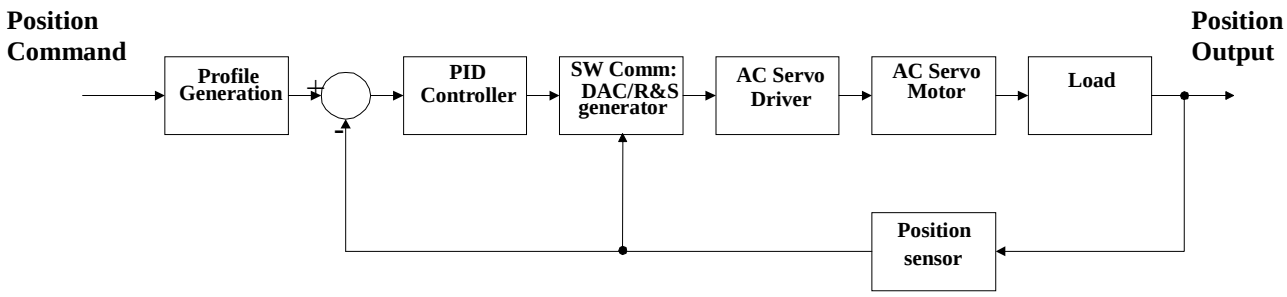

Figure 3-1 Block diagram of the position control loop

During initial testing, the step function motion profile is used to observe the time-domain response of the control system. As found in the investigation, the controller can be saturated very easily by the step input command. Due to the inertia and the limited power drive capability, the system will only allow a ramp function input. If there is a large initial step error appears at the controller input, it will try to drive the power stage to the limit in order to minimize the error.

Figure 3-2 shows the input and output response of a typical motion system. Simulation studies of the LPMSM system indicate that a saturation of the power stage will occur when the input step is large. A profile command is tested and the results show that it can effectively reduce the error applied on the input of the controller; hence the required driving power is minimized [43, 44, 45].

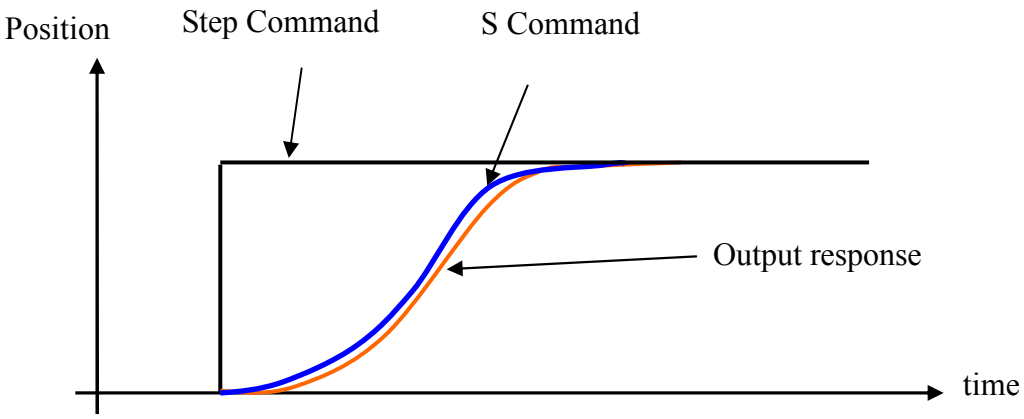

Figure 3-2 Step and 'S' profile command input

Another observation is that the overall mechanical system vibration is suppressed when the profile command is used. It is due to the high frequency harmonic from the step command is now band-limited by the relatively slow motion profile. These two findings are particularly useful in practical applications. As in real life, the physical controller and power drive will only have limited bandwidth and input/output ranges, a slow profile can improve the position tracking of the system, and reduced stress on the power electronics. Also, undesired vibrations can also be suppressed. This in turn reduces the stress of the mechanical parts.

In this project, a third order polynomial profile scheme is proposed as the profile generator. This is to generate the third derivative of the position variable and resulting in a simpler implementation of an S-profile.

The equations for the third order profile generator are shown below:

$$\frac{da}{dt} = \{J_{mx}, 0, -J_{\max}\} \qquad \textbf{(3.1)}$$

$$v = \int a dt \qquad \textbf{(3.2)}$$

$$x = \int v dt \qquad \textbf{(3.3)}$$

Where J, a, v and x are the jerk, acceleration, velocity and position of the motion system.

So if the maximum velocity (v), acceleration (a), and jerk (J), are defined, and the desired set point (x) is specified, the profile generator will generate the position command profile by the equations (3.1) to (3.3). The generator will calculate the ramp up time and ramp down time that based on the specified the dynamic limits. An approximate "S" position curve is obtained for feeding into the motion system.

As the S-profile can reduce the mechanical and electrical stresses on the system the following advantages can ready be obtained:

(i) Minimize the ware out of the mechanical parts such as bearings and preload.

(ii) Suppress the audible noise when the system is running due to reduced vibration.

(iii) Prolong the life time of the power electronic devices as the stress is relaxed.

(iv) Improve the system reliability as a result of (i) and (iii).

(v) Reduce the maintenance cost of the system.

Since the proposed profile generator requires only the integral action of the motion variables, it can easily be implemented in the DSP or MCU controller chip.

3.2 THE ROBUST DISTURBANCE COMPENSATED CONTROLLER

3.2.1 The Characteristics of the PID controller

The PID controller has the advantage of simple to implement and is widely used in the industry automation for position and velocity control [8]. When the load and friction are known and unchanged, and no disturbances got into the system, the control parameters can easily be tuned to obtain the desired dynamic response [9].

On the other hand, when disturbances exist and the load varies, it is difficult to obtain a consistent performance with only a set of control parameters [11, 12]. It is always the case that the load varies. For example in the transportation of the bonding substrate on a die bond machine, the load can vary from a copper lead frame to an organic PCB. Even the load varies; the dynamic response needs to remain unchanged in order not to decrease the

production yield [35].

As mentioned in previous sections, the direct drive linear motor is easily subject to load change and disturbance, therefore a robust control scheme needs to be developed to assure the dynamic response is not affected. Such robust control scheme is described in the subsequent section [13, 14, 38, 40, 41].

3.2.2 The Robust Disturbance Compensated Controller for Linear Drive System

The SISO system with observer is shown in Figure 3-3. *H* is the actual plant of the system while *L* is the observer that is introduced in order to detect any performance change due to disturbance *t*.

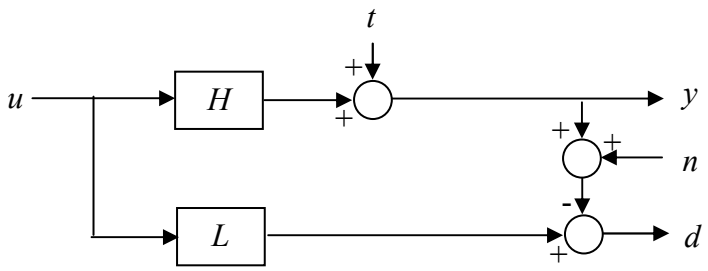

Figure 3-3 A SISO subsystem with its observer

The detected disturbance *d* of the system is therefore

$$d = (L - H)u + t - n \qquad (3.4)$$

Where u is the command, *n* is the noise of the system.

Normally L is the model that is same as the actual plant. Any performance change in the actual system due to the external disturbance *t*, or noise *n* is therefore ready be detected in such arrangement. [50]

Based on the disturbance based control system in Figure 3-3, a robust disturbance compensated controller for linear driver system is proposed. The robustness of the system is improved by introducing a force loop into the traditional PID control loop. The proposed disturbance compensated controller structure is shown in Figure 3-4. A software reference model is built according to the original model. The A_i and K_M is the current gain

of the power drive and motor force constant of the LPMSM. They are the same in the software reference model and the actual LPMSM and drive.

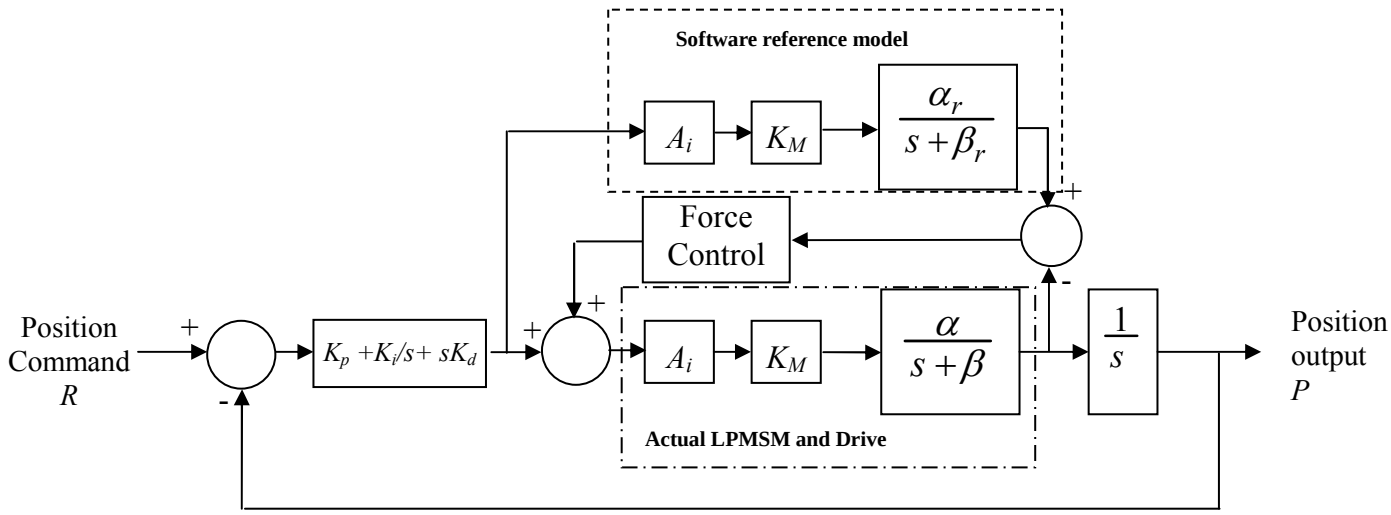

Figure 3-4 The proposed robust disturbance compensated controller for the LPMSM

The block $\frac{\alpha}{s+\beta}$ is the actual model of the LPMSM. α is the inverse of the mechanical mass of the motor M i.e. $\frac{1}{M}$; while β equals to $\frac{K_{vf}}{M}$ where K_{vf} is the dynamic friction coefficient of the motor.

The block $\frac{\alpha_r}{s+\beta_r}$ is the software reference model of the LPMSM. The term α_r is the inverse of the reference mechanical mass of the motor M_r i.e. $\frac{1}{M_r}$. The reference mechanical mass is the mass of the mover with no dummy load. While β_r equals to $\frac{K_{vf}}{M_r}$ with K_{vf} is the dynamic friction coefficient of the motor.

The Force Control block is to detect the difference between the velocity of the software reference model and the velocity of the actual LPMSM and drive. The output of the force control block will be added to output of the PID controller. The PID controller serves the

main position control function. The K_p, K_i and K_d are the proportional gain, integral gain and derivative gain of the PID controller respectively.

The concept is that a software reference load is built into the controller which has matched characteristics of the actual motor load. If there is no parameters change in the operation environment, the acceleration of the reference and the actual load will be the same. The error fed into the Force control block is zero and no compensation signal is generated.

When a system parameter change has occurred, e.g. an increase in the loading, the software reference model will produce a fast acceleration and a high velocity output. The positive velocity error will feed into the force control block. In response, a positive compensation signal is produced and it is added to the output of the PID controller. A higher driving force will be produced to drive the actual motor faster in order to catch up with the speed of the reference. As a result the dynamic performance of the actual motor with load change will appear the same as the reference, in other word the same as if the load has not been changed.

3.2.3 *The Controller Design*

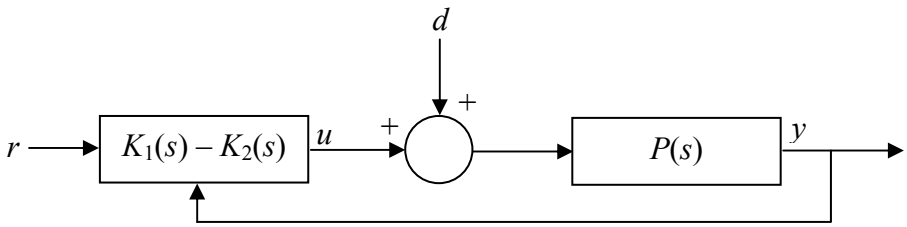

Figure 3-5 A general 2DOF controller

The feedback system in Figure 3-5 is a general two degree of freedom (2DOF) controller. Assume P(s) is an SISO strictly proper nominal system. Assume the 2DOF controller $K(s) = [K_1(s) - K_2(s)]$ is given by $K(s) = C(s) = [C_1(s) - C_2(s)]$ which is either already available or in operation with satisfactory nominal tracking performance, i.e. the transfer function from reference $r(t)$ to output $y(t)$ is satisfactory.

$$\frac{Y(s)}{R(s)} = \frac{C_1(s)P(s)}{1 + C_2(s)P(s)} \qquad (3.5)$$

Let the coprime factorization of P(s) be given as

$$P(s) = \frac{N(s)}{M(s)} \qquad (3.6)$$

where $M(s)$, $N(s) \in H_\infty$. Since C(s) is a stabilizing 2DOF controller for P(s), for any coprime factorization

$$C(s) = \frac{[X_1(s) - X_2(s)]}{Y_0(s)} \qquad (3.7)$$

where $X_1(s)$, $X_2(s)$ and $Y_0(s) \in H_\infty$. It is shown in [48, Theorem 5 of Section 5.6] that all 2DOF stabilizing controllers can be parameterized as

$$[K_1(2) - K_2(s)] = \frac{[S(s) - (X_2(s) + Q(s)M(s))]}{(Y_0(s)M(s) - X_2(s)N(s)} \qquad (3.8)$$

where $Q(s) \in H_\infty$ and $S(s) \in H_\infty$ are arbitrary stable system. If we plug $K(s) = [K_1(s) - K_2(s)]$ to the feedback system, then the transfer function from $r(t)$ to $y(t)$ becomes

$$\frac{Y(s)}{R(s)} = \frac{N(s)S(s)}{Y_0(s)M(s) - X_2(s)N(s)} \tag{3.9}$$

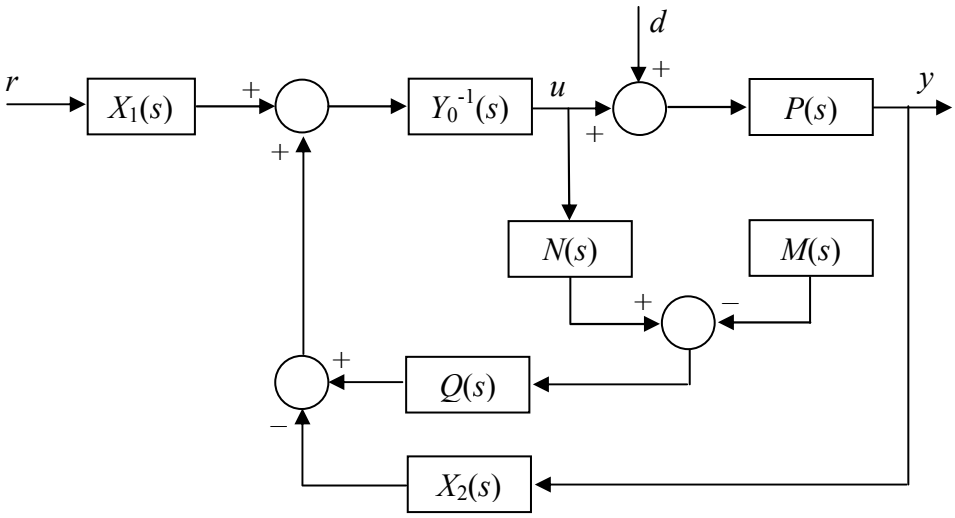

Figure 3-6 The proposed robust disturbance compensation controller

which is independent of $Q(s)$. Since we are satisfied with the original transfer function from $r(t)$ to $y(t)$ when $C(s) = [C_1(s) - C_2(s)]$ is used, then it follows that we can choose $S(s) = X_1(s)$ since

$$\frac{Y(s)}{R(s)} = \frac{N(s)S(s)}{Y_0(s)M(s) - X_2(s)N(s)} = \frac{C_1(s)P(s)}{1 + C_2(s)P(s)} = \frac{N(s)X_1(s)}{Y_0(s)M(s) - X_2(s)N(s)} \tag{3.10}$$

Therefore, the set of all stabilizing 2DOF controllers which depends on $K_2(s)$ and $P(s)$, now depends on $Q(s)$ only. For any stable system $Q(s)$, which can even be nonlinear and time varying, the nominal tracking performance is unaffected and the closed loop stability is guaranteed [49, 44]. Suppose that a $Q(s)$ is chosen, theoretically there are two ways to implement the new controller $K(s)$. One is to explicitly obtain $K(s)$ from (3.8) and implemented as in Figure 3-5. Or one can use the alternative structure as shown in Figure 3-6. The first way requires the dismantling of the original controller $C(s) = [C_1(s) - C_2(s)]$. The use of the structure in Figure 3-6 only requires the building of the additional disturbance compensation loop to the original controller. The original controller structure

is not affected and it is highly attractive in the actual coding as the additional loop can be plugged-in the main controller.

The function of the disturbance control block is to derive the compensation force from the velocity error input. Therefore the logical transfer function of the block is the inverse function of the software model (i.e. the inverse of the original actual load). In that case the force loop will produce no output as the load has no change. Otherwise the inverse characteristic of a motor load will transform the velocity error signal to a compensation force to drive the actual load to the original desired response. A low pass filter is added to the force loop in order to filter the noise pick-up and avoid instant feedback that may drive the power drive to saturation.

Regardless what the form of Disturbance Compensator is, provided that it is stable, the stability of the overall system is also stable. For a quick and easy implementation, the first order transfer function form for the Disturbance Compensation Controller F_c is used as follow:

$$F_C = \frac{s + \beta_r}{K_f s + \alpha_r} \qquad \textbf{(3.11)}$$

Where K_f is to select the low pass characteristic of the disturbance compensated controller.

3.3 AN ALL-DIGITAL PWM DRIVE

In order to implement and test the robust disturbance compensated controller for the LPMSM drive system, an all-digital PWM drive structure is proposed. The block diagram of the drive is shown in Figure 3-7. It is divided into five main parts: The PC, DSP, Signal Interface, Power Stage and the LPMSM [24].

Because of the advance in microelectronic, more and more high-performance DSP chips are available in the market [9]. There are many DSP chips specially made for motion control purpose as offer in low cost. Some of them have already build-in ADC, encoder

ports and PWM ports. So the DSP is selected for the controller of the PWM drive.

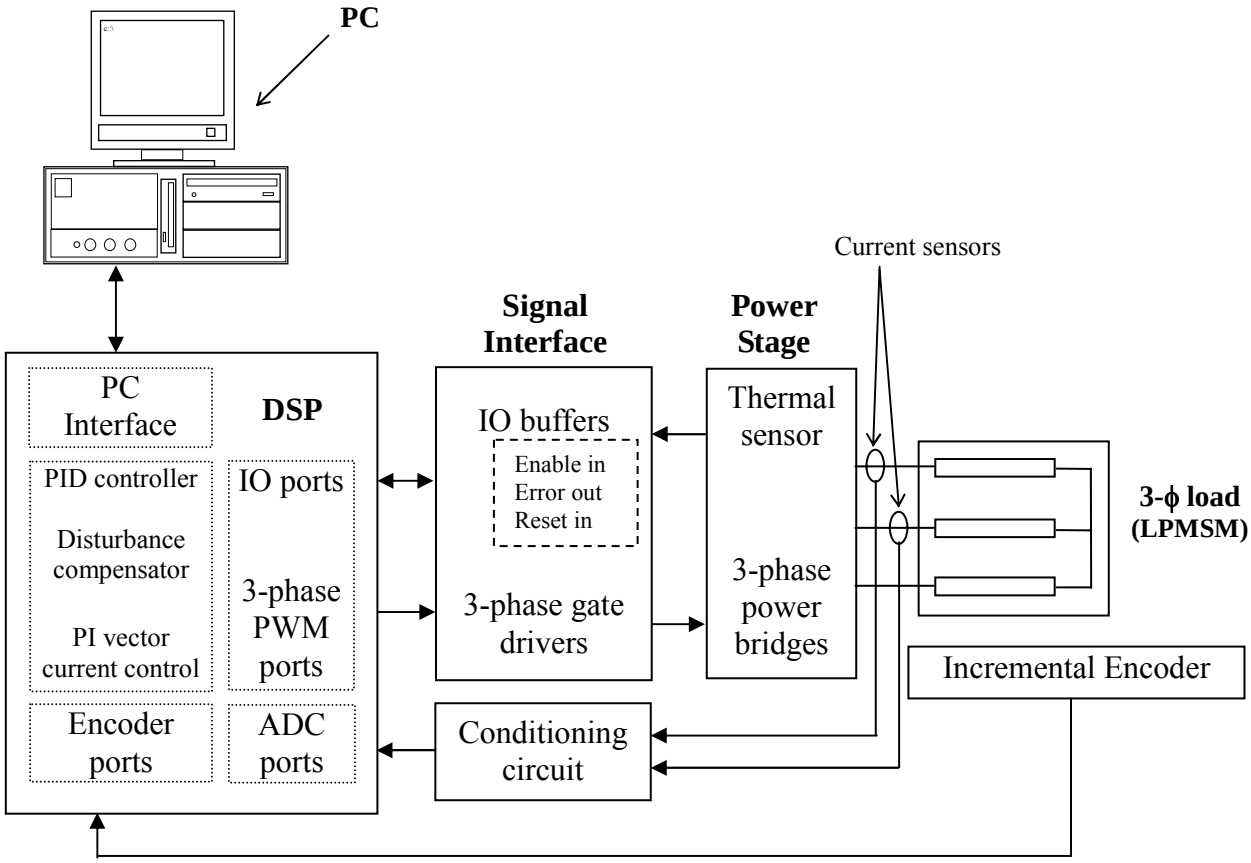

Figure 3-7 The proposed all-digital PWM driver for LPMSM

The DSP block is for implementing the PI current control, PID position control and the proposed disturbance compensation. Its ADC ports digitize the signal conditioned current signal for feeding to the PI vector current controller. The encoder ports are for sensing the mover position of the LPMSM. There are the IO ports and PWM ports for the generating and receiving the control signals to and from the signal interface blocks. The PC interface, which can be a serial bus or parallel, is for communication between the PC and the DSP block [42].

The PC serves the human machine interface function. All the control tuning parameter can be set via the PC. The respective motion dynamic signals can also be displayed and monitored.

The Signal Interface block contains the IO buffers, the 3-phase gate drivers and signal conditioning circuit. There is an error signal feedback to the DSP controller from the IO buffer. The error signal is activated when short-circuit or over-temperature in the power stage is detected. The IO buffers receive the enable signal and the reset signal. The enable signal is to energize the power stage, while the reset signal is to clear the detected short-circuit or over-temperature error when it has happened. The conditioning circuit is to scale and level shift the motor phase current signals to the APC ports of the DSP.

The power stage consists of the 3-phase power bridge and the thermal sensor. The 3-phase power bridges receive the PWM signals and provide power drive to the LPMSM. The thermal sensor is to monitor the temperature of the power bridge. If the temperature is above the preset operating limit of the power devices, an over-temperature error is report to the controller.

The linear encoder is to detect the position of the mover of the LPMSM. The encoder signals are direct feedback to the DSP block for current and position control of the system.

CHAPTER FOUR MODELING AND SIMULATION

In this chapter, the model of the LPMSM, the power drive and the overall control system will be developed by using the Matlab Simulink toolbox. Then the simulation studies of the robust LPMSM drive system will be presented.

4.1 MODEL OF THE LPMSM DRIVE SYSTEM

With the derived magnetic flux linkage, voltage, power and force equation of (2.52)~(2.54), the model for the linear motor can ready be built with the Matlab's Simulink Tools box. Figure 4-1 is the overall model of the Linear PM Synchronous motor:

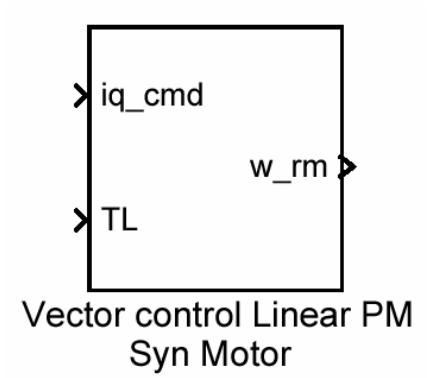

Figure 4-1 Matlab model symbol of the LPMSM

The inputs to the model are the thrust command, *iq_cmd* and the loading thrust, *TL*. The loading thrust is the total mass of the move including the dummy load. The electrical angle of the mover, *w_rm*, is the output of the model.

4.1.1 Inner Structure of Model

Figure 4-2 shows the inner structure of the model. It is composed of two parts:

(i) The mover flux oriented indirect vector controller and

(ii) The *PM_SM_current_input* model.

The parts (i) converts the i_d (set to zero) and i_q (the force) commands to the 3-phase *a*, *b* and *c* motor currents with the electrical angle of the mover as the vector controller input. The blocks *ia_off* and *ia_off1* is for setting the offset bias to the current command *ias* and *ibs*. The offset bias is to compensate the offset in the current sensor and the associated circuitry.

The part (ii) is the model that converts current inputs to thrust and then velocity and position as the outputs.

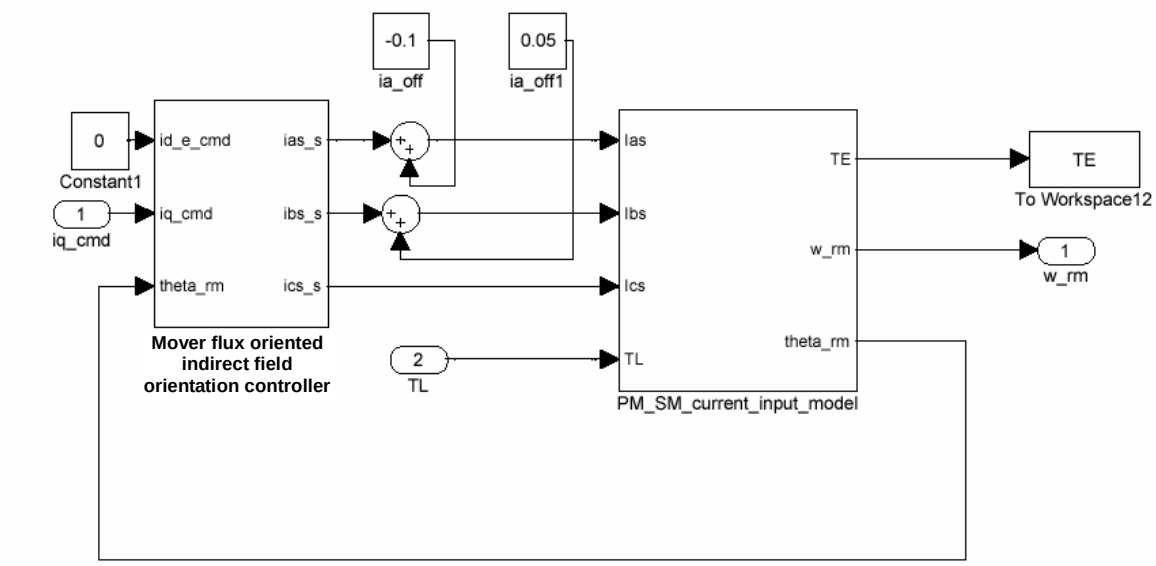

Figure 4-2 Inner structure of the Matlab model of the LPMSM

4.1.2 Vector Controller

Figure 4-3 shows the detailed construction of the vector controller:

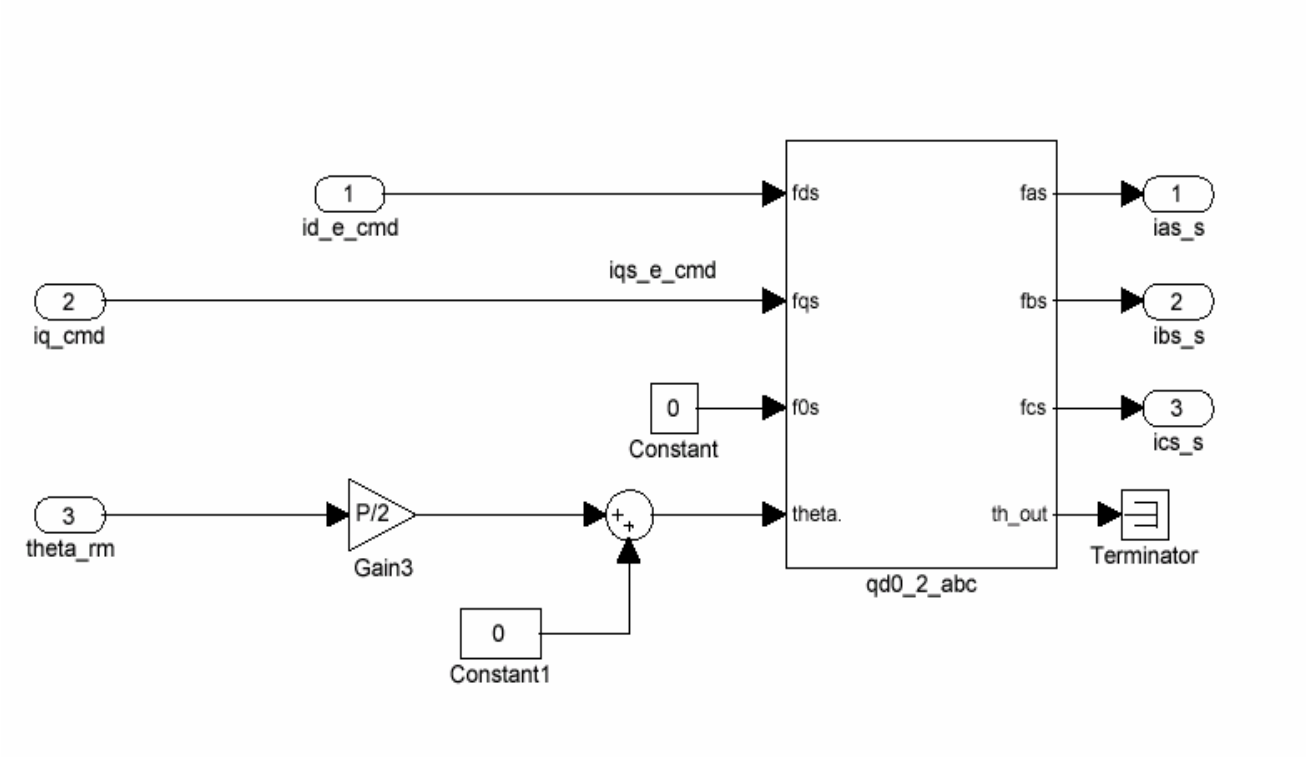

Figure 4-3 The vector controller

It performs the Inverse Park Transform function of (2.53) and transforms *id* and *iq* to the 3-phase current in the *abc* reference frame. The angle information *theta_rm* is obtained by (2.2), i.e.

$$\theta = \pi \frac{x}{p}$$

Where x is the position input from the encoder and p is the magnetic pole pitch of the linear motor.

4.1.3 PM_SM_Current_Input Model

Figure 4-4 is the inner structure of the *PM_SM_Current_Input_Model*.

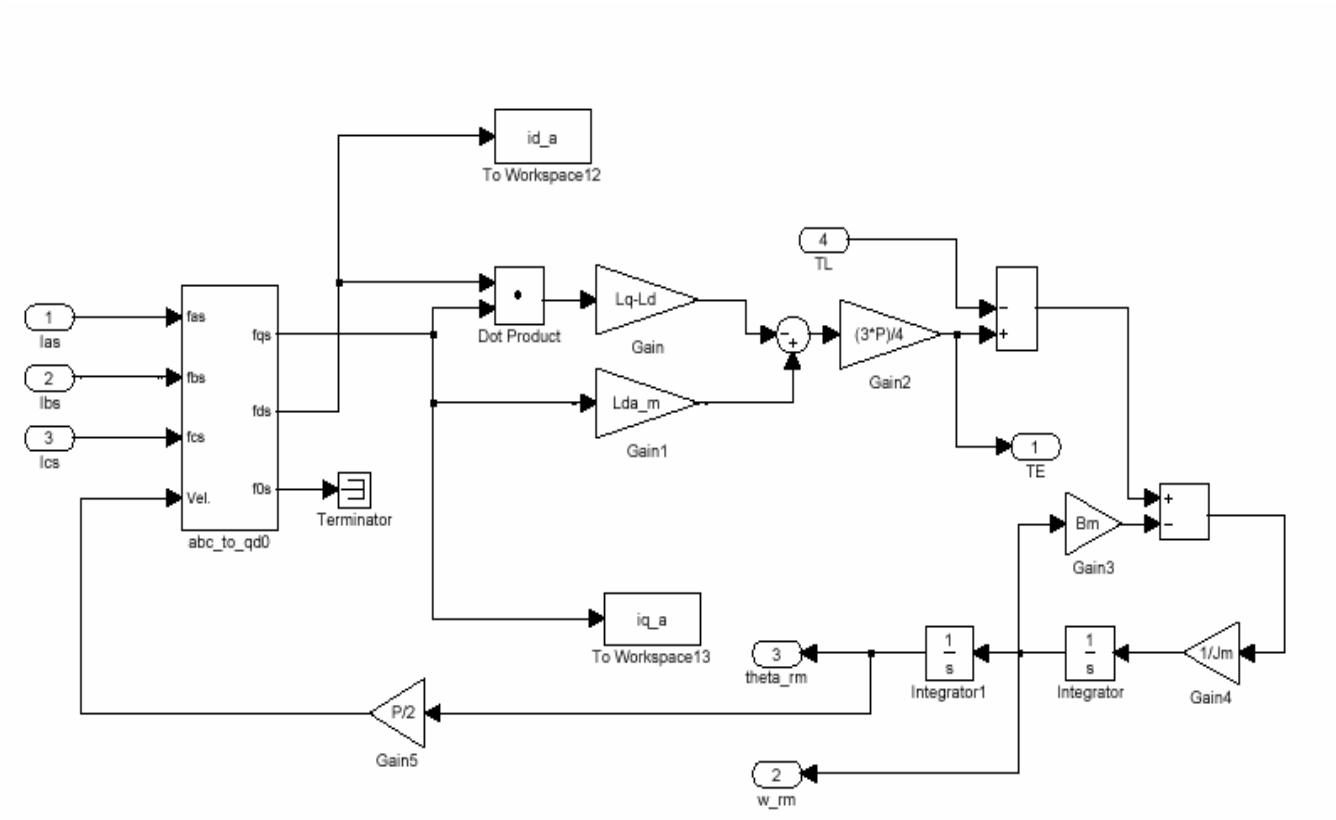

Figure 4-4 The PM_SM_Current_Input Matlab Model

The model first performs the Park Transform function of (2.52). It converts the 3-phase motor currents in the *abc* frame to the *id* and *id* current in the *dq* reference frame. The dynamic response of the motor is then obtained by the transformed motor model in the *dq* frame that also based on (2.52).

There are two outputs for this model:

- The position of the mover *w_rm* for the vector controller model
- The force output of the linear motor for monitoring.

4.2 MODEL OF THE POWER DRIVE

The Matlab model of the power drive is shown in the Figure 4-5 below.

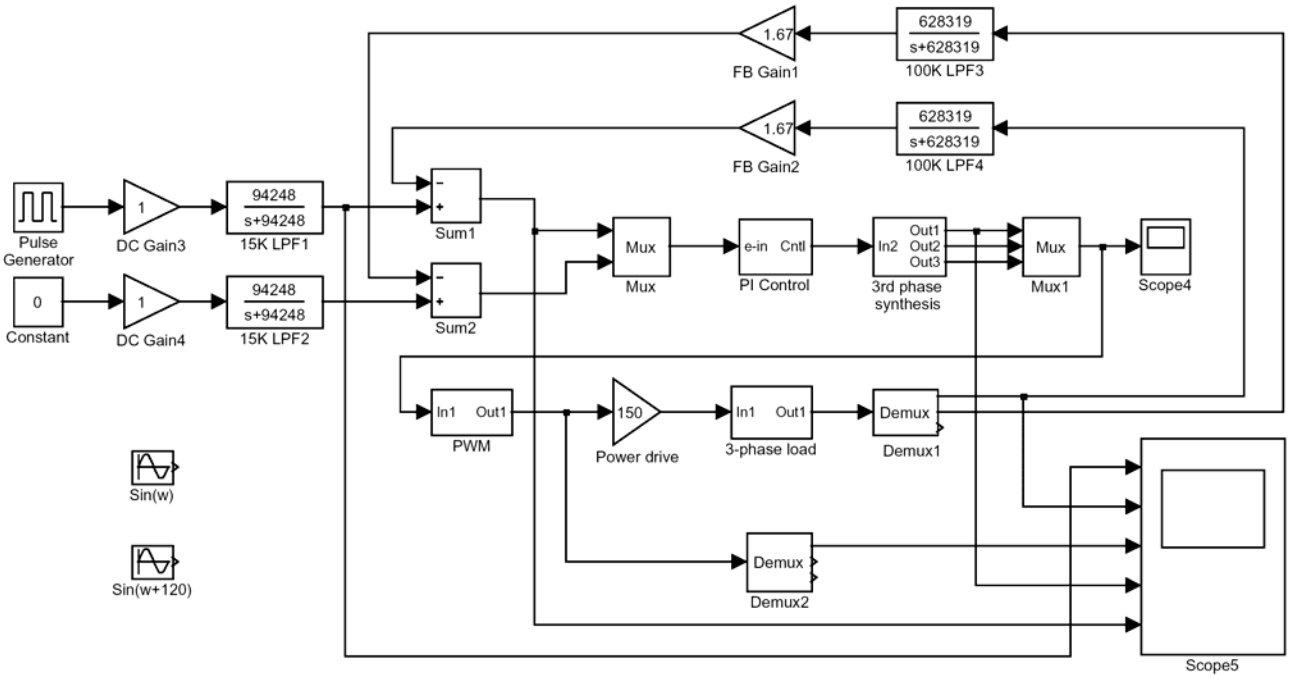

Figure 4-5 Matlab Model of the Power Drive

The model is based on the block diagram in Figure 4-5. The low pass filter in the two feedback loop is used to simulate the 100Kz bandwidth of the Hall effect current sensors. The 3-phase load is three inductor and resistors in Y-connection. The back EMFs of the motor are ignored in order not monitor the step input time domain test. It is because in the actual test of the driver performance, e.g. frequency bandwidth and step response, the mover of the motor is locked. This is to avoid any mover vibrations that may affect the bandwidth measurement especially at the frequency around the mechanical resonance of the motor.

The command input and the corresponding phase current is monitored. The data is captured for analysis and comparison.

4.3 MODEL OF THE ROBUST LINEAR DRIVE SYSTEM

The model of the Robust Linear Drive System is build by using Matlab Simulink as shown in Figure 4-6.

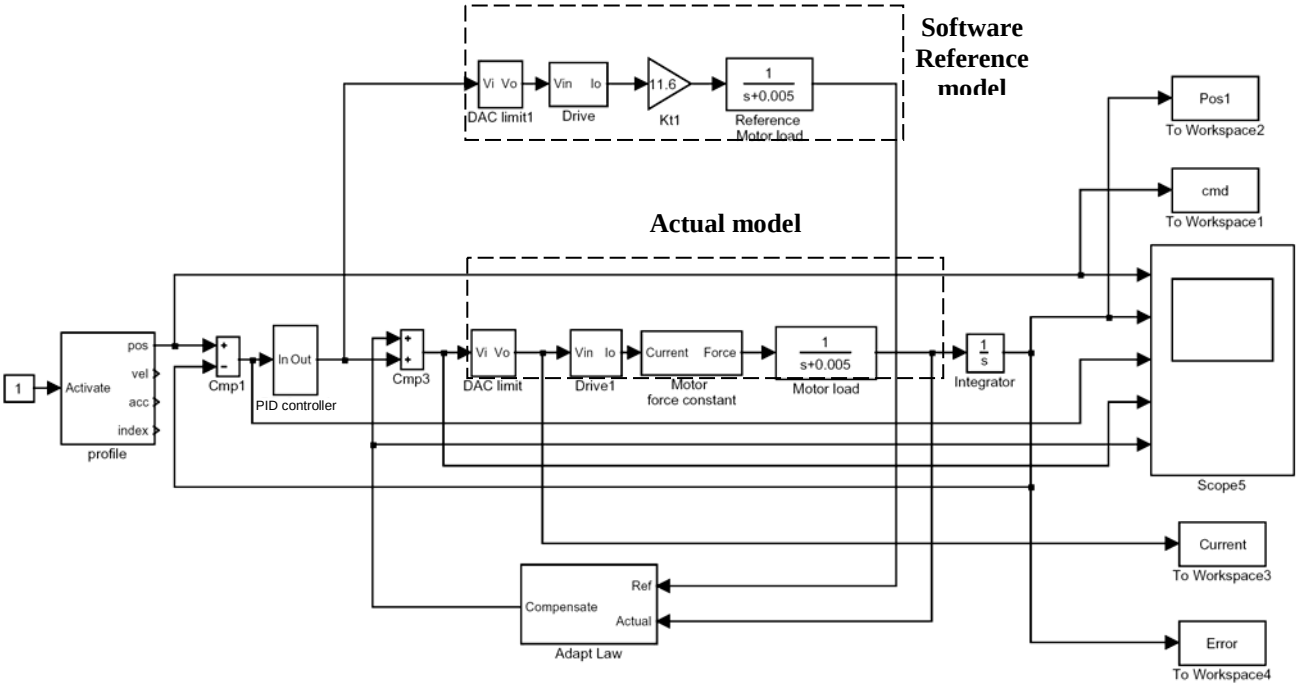

Figure 4-6 Matlab Model of the Robust Linear Drive System

The developed model is based on the block diagram derived in Figure 3-4

The reference motor load is on the top of the diagram. The blocks in this path is almost the same as path in the actual model except the load in the reference is fixed at the initial value. The PID control block is tuned to the loading before it is changed. The compensation loop is in the bottom. The block, *Adapt Law*, is based on (3.10). It produces the required compensation signal to the actual driving path. The input to the block is the velocity of the reference load and the actual load.

The block, *profile*, is for generating the third order profile according (3.1) to (3.3).

Up to here, the MATLAB Simulink models of the LPMSM drive system have been built. The actual hardware implementation will be discussed then the simulation results of the modeling will be presented.

4.4 SIMULATED RESPONSE OF THE LPMSM DRIVE SYSTEM

4.4.1 Simulated Current Loop Response

The simulated current loop response by using the Matlab Simulink is shown in Figure 4-7. The DC bus voltage is 150V, motor phase-to-phase inductance and resistance is 1.1mH and 0.9Ω respectively. Motor load current is 1A. The input is 10% of the rated command. As can be seen the simulated current rise time of the model is about 1ms. The full load step response of the digital current loop is shown in Figure 4-8

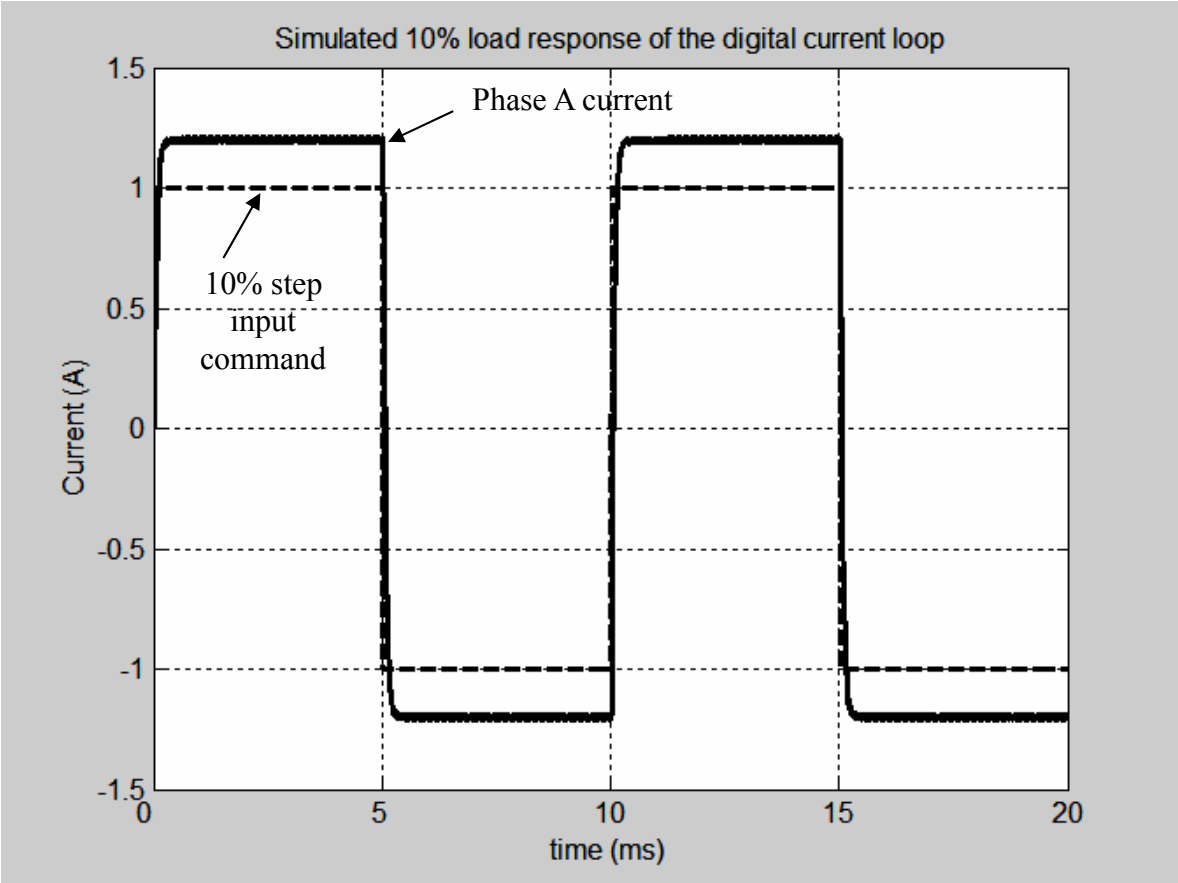

Figure 4-7 Simulated 10% load step response of the digital current loop

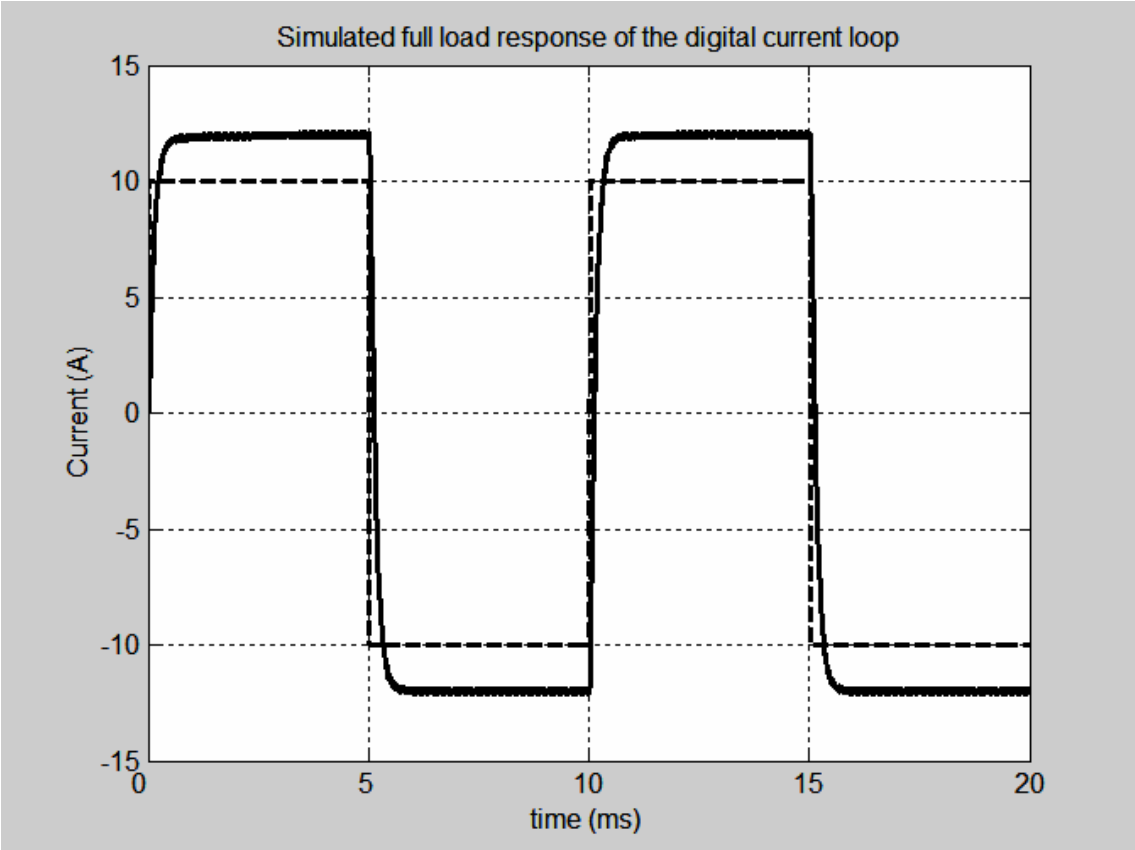

Figure 4-8 Simulated full-load step response of the digital current loop

4.4.2 Simulated Response of the Robust Disturbance Compensator

The profile settings for the simulations are shown in the Table 4-1 as follow:

Travel distance	12cm
Maximum/minimum velocity	3m/s
Maximum/minimum acceleration	+/- 60m/s^2
Maximum/minimum jerk	+/- 1200000m/s^3
Sampling time	0.5ms

Table 4-1 Profile setting for the simulations

The simulated responses of the LPMSM drive system are shown in Figure 4-9 to Figure 4-14.

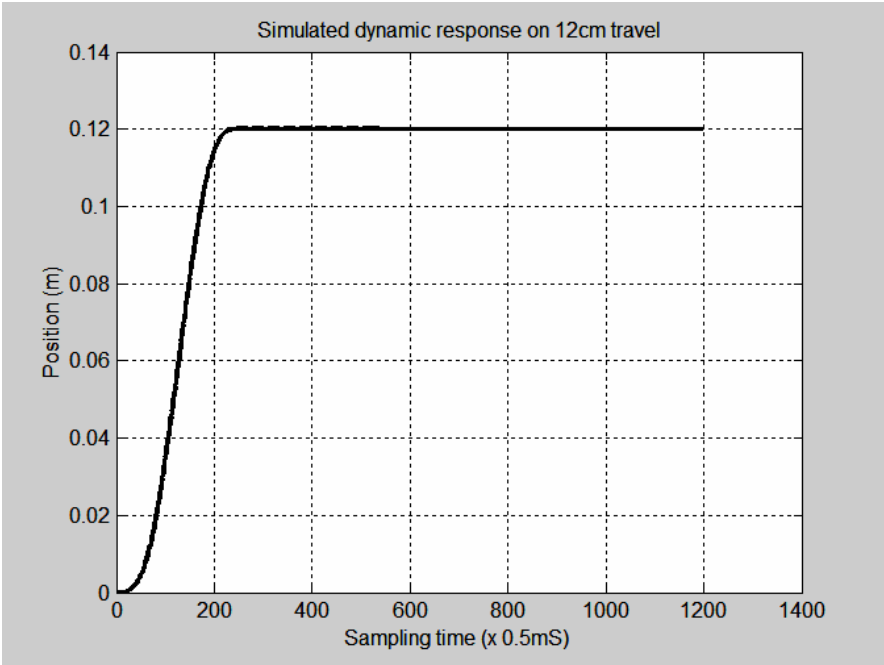

Figure 4-9 Simulated dynamic response

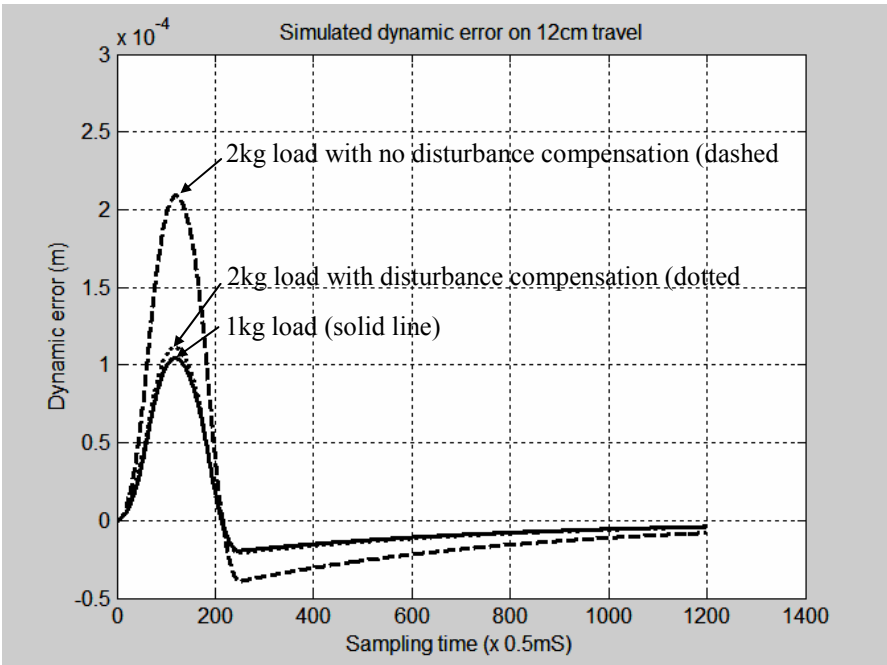

Figure 4-10 Simulated dynamic error

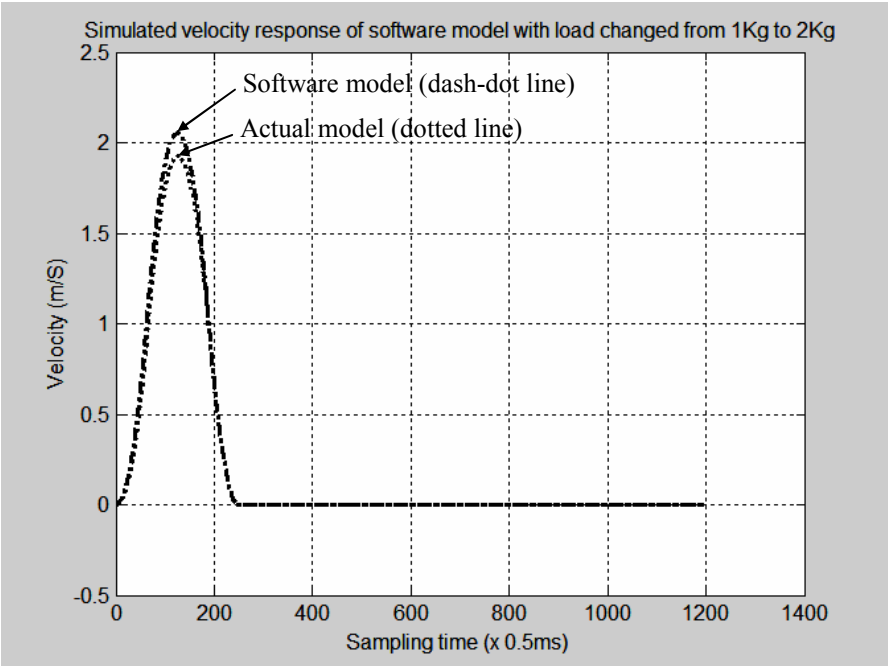

Figure 4-11 Simulated velocity of software and actual model

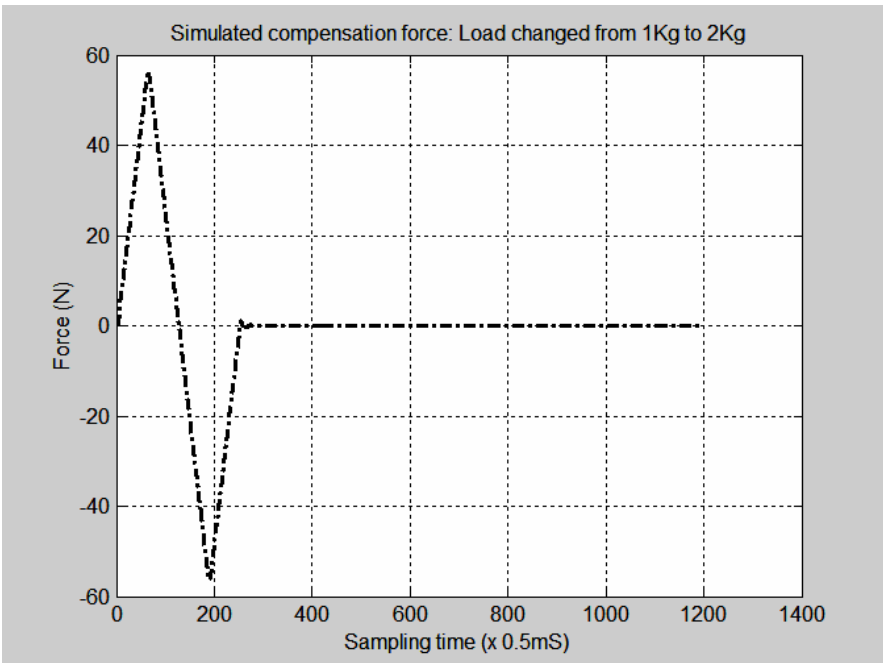

Figure 4-12 Simulated output of the disturbance compensator

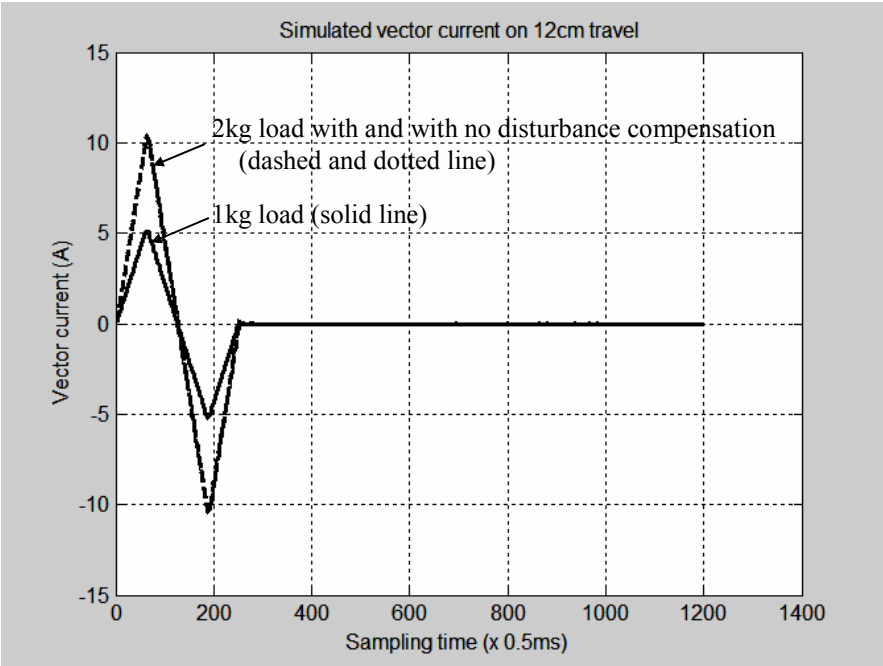

Figure 4-13 Simulated vector current

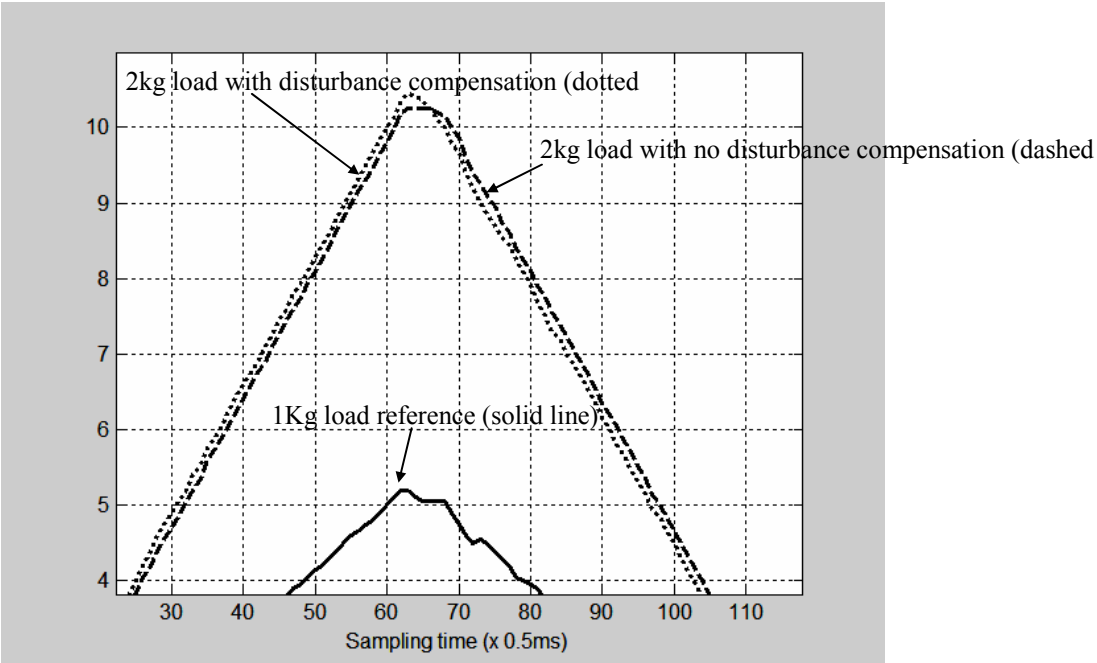

Figure 4-14 Zoom up of vector current (Figure 4-13)

For all simulated responses, the solid lines are the responses of traditional PID controller at 1kg load with no disturbance compensation. This is taken as reference. The dashed lines are the responses of the traditional PID position controller when load is changed from 1kg to 2kg with no disturbance compensation. The dotted lines curves are the 2kg

load response with disturbance compensator is activated.

The simulated dynamic responses of the LPMSM drive system are shown in Figure 4-9. All the three responses are similar and close to the command profile. The overshoot in all cases is not obvious. The overshoot for the 2kg load response with no disturbance compensation is 0.33%. The 1kg load response and 2kg load response with disturbance compensation is very the same at 0.17%.

The simulated dynamic errors are shown in Figure 4-10. In the 1kg load case, the peak error and settling time for within 15μm is 210μm and 205ms (410 sampling time). When the load is changed from 1kg to 2kg and disturbance compensation is not activated, the dynamic error increases from a peak of 105μm to 210μm. The settling time is increased to 415ms. When the disturbance compensator is activated, the peak dynamic error drops to 110μm and is closed to the 1kg response. With the disturbance compensator, the settling time for the error to fall within 15μm is 225ms (450 sample time), which is close to the the 1kg response.

The simulated velocity responses of the software motor model and the actual motor model with disturbance compensation are shown in Figure 4-11. The velocity profile of the actual model is lower than the software model when the load is increased from 1kg to 2kg. The peak velocity difference is 2.05m/s - 1.92m/s = 0.13m/s. The corresponding disturbance compensator output is shown in Figure 4-12. The disturbance compensator produces a peak correcting force of 58N to minimize the velocity difference between the actual and software model.

The simulated vector current responses are shown in Figure 4-13. Regardless the disturbance compensator is activated or not, the peak currents increase from 5.2A to 10.2A when the load is changed from 1kg to 2kg. The vector current profile for 2kg load is similar. The zoom up of the vector currents are shown in Figure 4-14. In the 2kg load response, the activation of disturbance compensator has an effect to advance the vector current in order to drive the dynamic the same as the 1kg load response.

The simulation results are summarized in Table 4-2.

	1kg load	2kg load	2kg load
Disturbance compensation	-	No	Yes
% overshoot	0.17%	0.33%	0.17%
Peak dynamic error	105μm	210μm	110μm
Settling time (within 15μm)	205ms	415ms	225ms
Peak vector current	5.2A	10.2A	10.5A
Peak velocity	1.924m/s	1.927m/s	1.925m/s
Peak acceleration *	6.03G	5.98G	6.05G
Peak compensation force	-	-	56N

* 1G=10m/s^2

Table 4-2 Simulation results summary

From the simulation results in Table 4-2, if the disturbance compensator is not activated, the peak dynamic error and settling time is about twice the 1kg response. If the foce compensator is activated, the responses are close to the 1kg responses. Therefore, the simulation results show that the disturbance compensator can improve the dynamic response of the LPMSM drive system for a load change of 1kg to 2kg.

The implementation of the proposed robust disturbance compensated controller will be described in next chapter. The actual dynamic response of the system will be measured in subsequent chapter.

CHAPTER FIVE IMPLEMENTATION OF THE LINEAR DRIVE SYSTEM

To use exactly the same copy of software code for simulation and implementation, the Real-Time Workshop toolbox of the Matlab software is used [5]. The program can generate the software code of the control algorithm of the model direct to the dSPACE controller card DS1102. The DS1102 controller card contains DSP chip for high speed control signal processing. It also provides powerful interface for easy implement of the required control system. The features of the DS1102 controller card can be found in Appendix I.

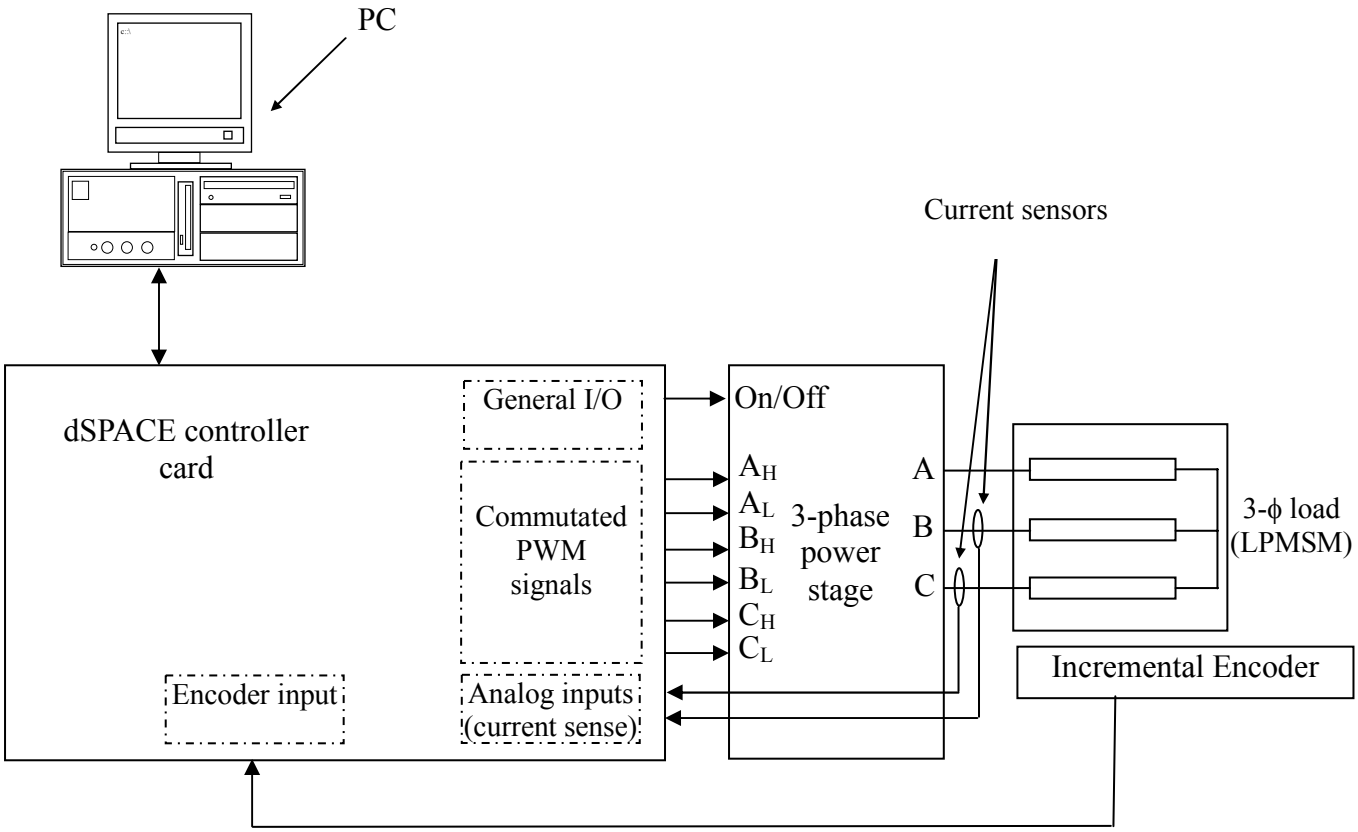

Figure 5-1 Arrangement of the Linear Drive System

The arrangement of the parts for the digital LPMSM driver is shown in the Figure 5-1. It consists of a PC for editing, compiling, monitoring and downloading the program into the dSPACE card. The dSPACE card is the controller that contains a DSP, I/O, PWM outputs and Analog input for controlling the 3-phase driver. The 3-phase driver is for delivering power to the linear motor whose current is to be controlled.

5.1 MOTOR COMMUTATION

Based on the Park's transformation equations (2.52) and 2.53), the mover position must be known when converting the vector current command into the respective three phase current command or vise versa. Unless an absolution encoder is used, the mover starting position is usually not known when just powering on the system. Therefore a sequence of procedure is needed in order to commutate the motor correctly.

The flow chart in Figure 5-2 is an algorithm to determine the mover position for motor commutation of brushless motor.

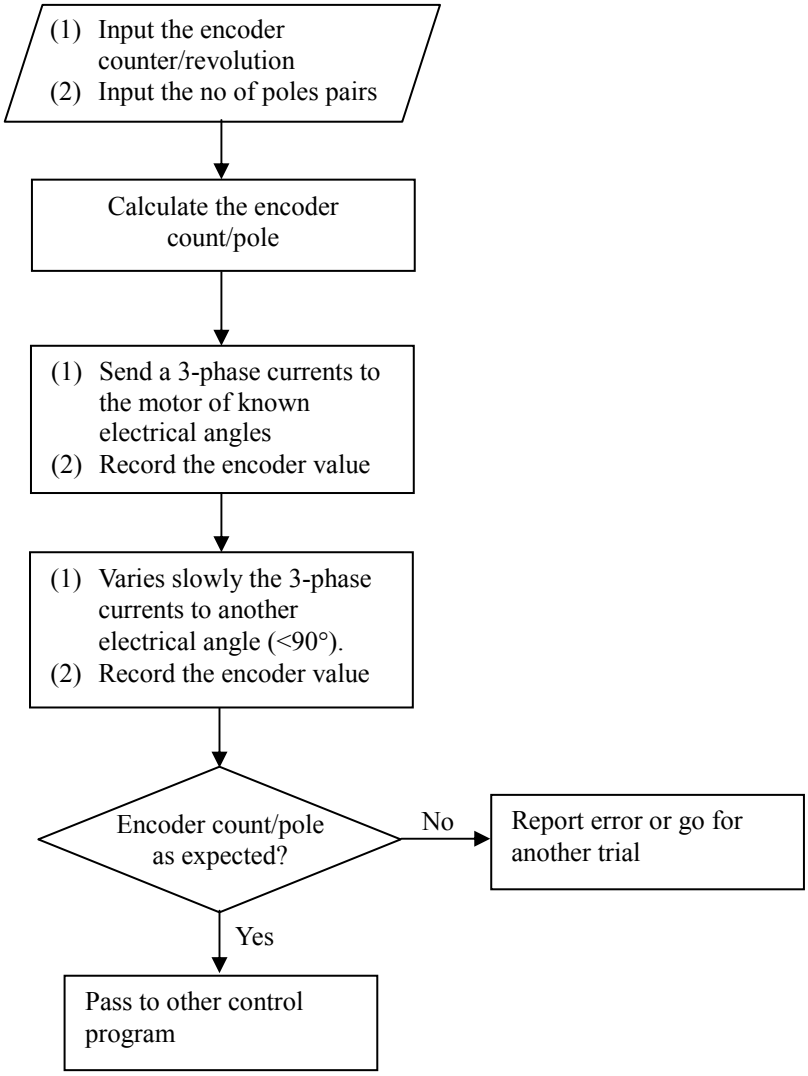

Figure 5-2 Flow chart for motor commutation

The software will get the encoder count per revolution and no of pole pairs of the motor. The encoder count per pole is calculated and the number of encoder counts for an electrical cycle of the motor is known. A 3-phase current of known and fixed electrical angle is send to the motor. The mover will then be locked by the 3-phase current to a particular position, and the encoder value is recorded when mover is steady. Then the 3-phase current is move slowly to another electrical angle and it is usually within 30° in practice. When the mover settles to the new position with no vibration, the encoder position is recorded. Therefore the mover displacement in electrical angle should match the electrical angle displacement of the 3-phase current. If the electrical angle displacement of the mover matches the expected angle, the mover position is known. If it does not match the expected encoder count, the software can go for another trial or report error to the user.

The mover position angle is calculated by:

$$\theta_p = \pi \text{ (mover encoder position / encoder counter per pole)} \qquad \textbf{(5.1)}$$

5.2 POWER STAGE OF THE LINEAR DRIVE SYSTEM

Figure 5-3 is the block diagram of the 3-phase power stage for driving the LPMSM.

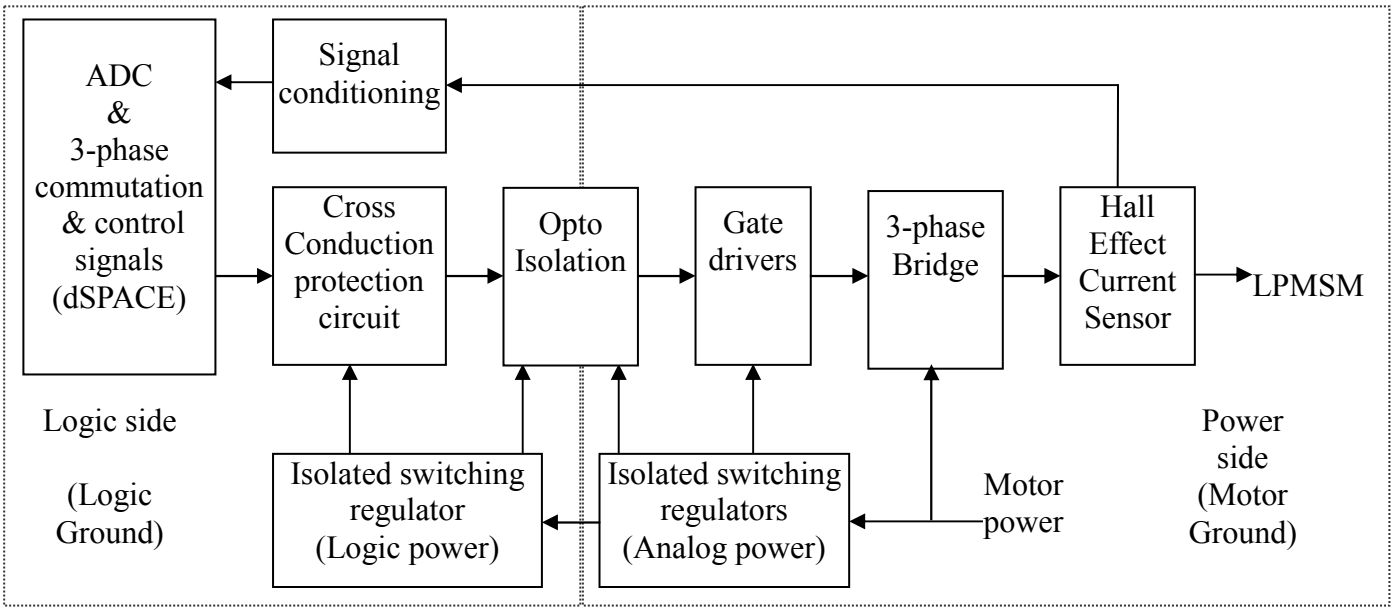

Figure 5-3 Block Diagram of the 3-Phase Power Stage

It consists of a cross-conduction protection circuit which generates the required dead time for the switching between the high-side and the low-side power devices. The logic design

of the cross-conduction protection circuit also prevents the simultaneous turn on of both the high-side and low-side power devices, hence avoiding damage to the 3-phase bridge due to incorrect PWM signal inputs.

In considering the low inductance and the exposed motor coils structure, opto-isolation is employed to isolate the power logic controller from the noisy power stage and motor coils. Isolated switching regulators for individually powering the logic side and the power side are installed. Hall effect current sensors are used for sensing the motor phase current and for providing signal isolation. In this manner, the logic side can be completely isolated from the power side, and ground looping and possible conductive EMI noise problem can be reduced. Also, signal interference in the small signal logic circuitry due to high speed switch of the power device at high voltage and high current can be minimized. The gate drivers are for interfacing the small signal PWM logic signal to the power devices. The 3-phase bridges are for the high-current drive of the motor load [18].

5.3 OPTO-ISOLATION CIRCUIT

Since the inputs of the gate driver are logic signals, they can be isolated by the digital opto-couplers. The HCPL2630 opto-coupler is used. It is a dual channel opto-coupler and has 10M high speed bit rate.

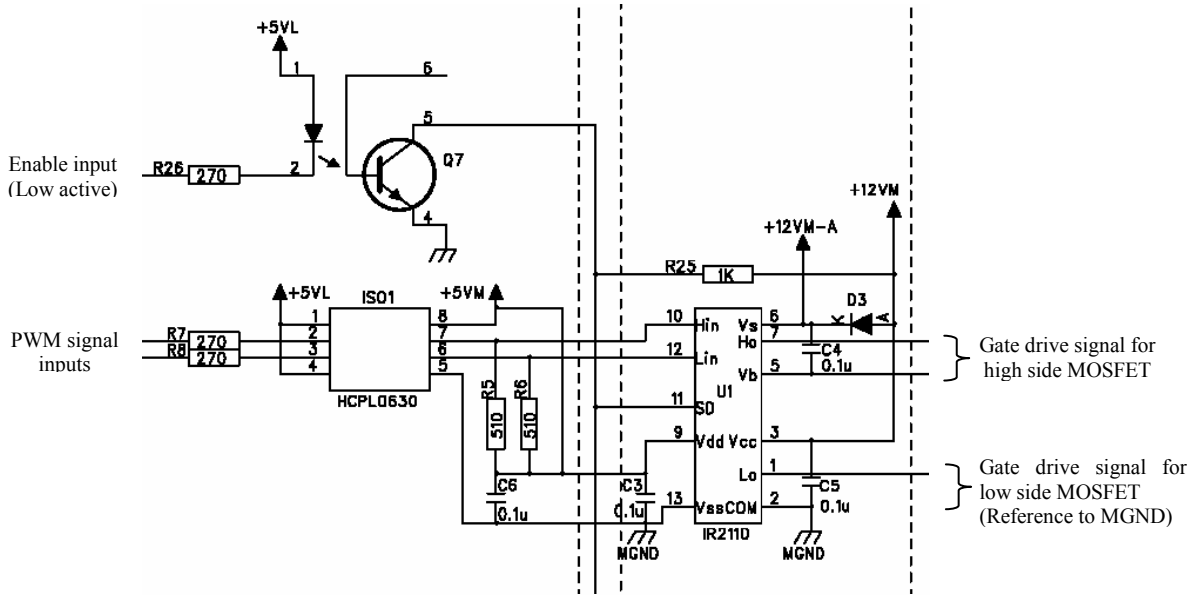

Figure 5-4 Signal isolation of the power stage

The circuit in Figure 5-4 is the actual PWM signals isolation circuit for one half of the MOSFET bridges. The minimum turn on current for the input diode of the HCPL2630 is 7mA, so a 270Ω input resistor can suitably interface to 5V TTL signals. The propagation delay of the opto-coupler is less than 200ns, therefore it has negligible effect on the 20kHz PWM signals.

The slow speed 4N26 opto-coupler (Q7) can be used for the isolation of the enable signal, which dose not need the high speed characteristic.

5.4 THE 3-PHASE BRIDGE AND GATE DRIVER CIRCUIT

Figure 5-5 is a bridge drive circuit. The power devices are represented by the high side switches *A_H* and *B_H*, and also the low side switches *A_L* and *B_L*. Each switch has an ideal diode (D1-D4) connected in parallel. The high side and low side switched of each half-bridge are driven in anti-phase to avoid shoot through. The carrier cancellation PWM method is employed [19, 20], that is has the advantage of minimal current ripple at near zero current level. The PWM for controlling the output of the half-bridge is the central aligned type [47], which enables a double update rate for the current control to the motor load.

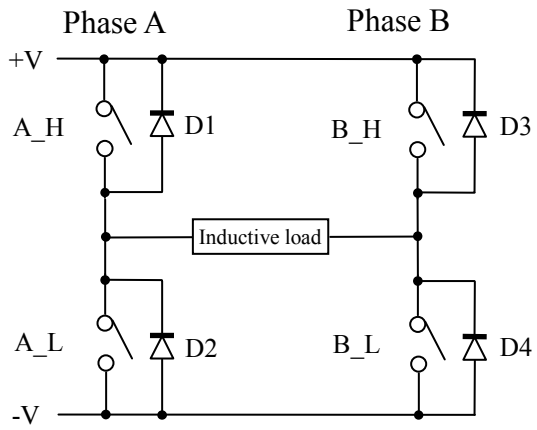

Figure 5-5 A bridge drive circuit

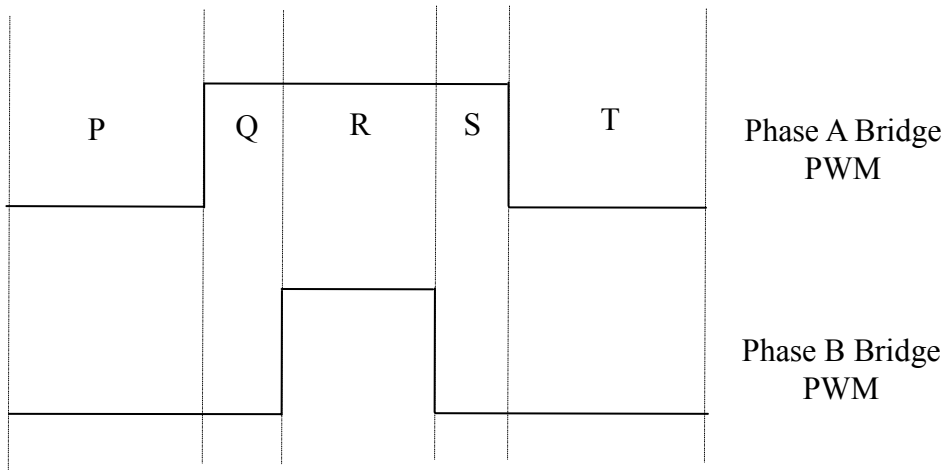

Figure 5-6 Central aligned PWM signals

A high level PWM signal feeds to the half-bridge (Phase A or Phase B) means high side is turned on and low side is turned off, and vice visa for a low level of PWM signal.

Assume the current is being flown in the inductive load from the phase A to phase B as implied by the PWM in Figure 5-6. In time zone P and T, both the low side power switches of the bridge circuit are turned on, current circulates in the low side switch (*B_L*) and diode (D2). In zone Q and S, current is being charged to the inductive load from the phase A to phase B. While in zone R, current circulates in the high side power switch (*A_H*) and diode (D3). ,

The switch sequence of the power devices is summarized in the table below:

Time zone	A_H	A_L	B_H	B_L	D1	D2	D3	D4	Description
P	OFF	ON	OFF	ON	OFF	ON	OFF	OFF	Current circulating at low side
Q	ON	OFF	OFF	ON	OFF	OFF	OFF	OFF	Current charging from phase A to phase B
R	ON	OFF	ON	OFF	ON	OFF	OFF	OFF	Current circulating at high side
S	ON	OFF	OFF	ON	OFF	OFF	OFF	OFF	Current charging from phase A to phase B
T	OFF	ON	OFF	ON	OFF	ON	OFF	OFF	Current circulating at low side

Table 5-1 Switching sequence of the power devices in a PWM cycle

The 3-phase bridges are implemented by 3 pairs of N-channel power MOSFET half-bridges. The IRF640N power MOSFET is used for building the 3-phase power bridge. Since the power bridge will be operated at 150V, the maximum 200V drain-source

voltage of the IRF640N allows a 25% safe operation margin. Since the motor load required a 15A peak and 5A RMS current, the 18A RMS driving capacity of the IRF640N can deliver the required current to the load. In addition, the IRF640N is equipped with a fast recovery diode, this enable an efficient bridge drive circuit to be built.

The IR2110 gate driver chip is used for driving the power MOSFETs. It can deliver a 2A peak current and switching speed can be up to 100KHz. Since the IR2110 is a half bridge gate driver chip, it can be placed close to the half-bridge power MOSFETs. This can minimize the length of the gate wiring and reduce possible gate ringing that may degrade the efficiency and cause EMI noise problem.

Three floating power supplies are used for powering the three high side gate driver circuits individually. This has the benefit over the charge pump circuit that the PWM duty cycle can be driven to 100% with no time limit. Also, a faster current rise time can be obtained. The isolated power supply, BXA24D12 from Computer Product, is used. It can deliver 125mA to the load and has 400Vdc isolation voltage. The low side of the gate driver chips are power by the forth isolation power supply. This allows the power side can be electrically isolated from the small signal controller side.

The gate drive voltage required to obtain the specified operation characteristic of the power MOSFET is 10V. While the maximum allowable gate voltage is 20V, so a 12V power supply for the gate driver can fulfill the need.

As the PWM signal inputs to the gate driver chips are in digital form, the power side can be isolated from the small signal side by the digital opto-couplers HCPL2630. They are high-speed couplers of up to 10M bit/s. The isolation of the enable signal is by the low speed opto-coupler of the 4N26.

The parallel resistor-diode is used for the fast turn-off and slow turn-on of the MOSFETs. The power MOSFET has a faster turn-on time (typically 150nS) than the turn-off time (typically 250nS). Therefore the parallel resistor-diode pair on one hand is to balance the switching characteristics of the MOSFET, and on the other hand slow down the turn-on speed of the MOSFET. This can minimize the reverse current stress on the body diode, which in turn reduces the noise generation in the power circuit. By experiment, a 100 Ω

gate resistor is used. The circuit in Figure 5-7 below is a phase of the gate drive and the power MOSFET bridge. The other two phases are identical except that the pull-high resistor (R19) is not needed in the other phase.

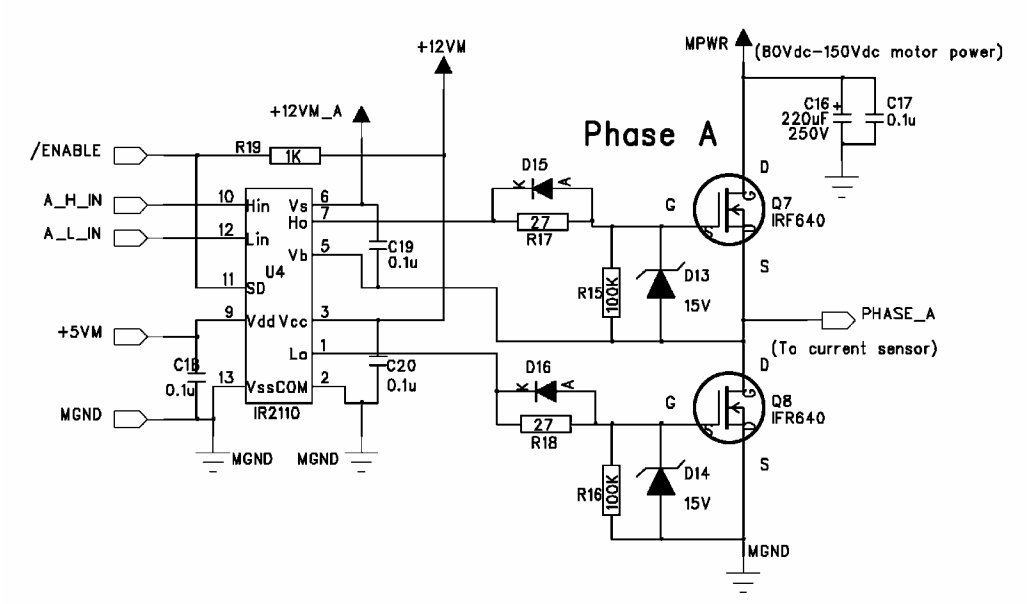

Figure 5-7 Gate driver and the power MOSFET bridge

Since the bridge circuit will automatically clamp the voltage across the motor load to the applied 80V bus voltage, voltage transient will not occur and the MOSFET will not be damage by transient Drain-Source voltage surge. However, the wiring at the source of the MOSFET needs to keep short to minimize the stray inductance. Otherwise, transient voltage may appear at the gate driver circuit that may cause unwanted voltage bouncing at the gate driver voltage and lead to excessive heat dissipation. A 15V zener diode is added to the gate-source terminal to protect the gate of the MOSFET from damaging by the transient voltage pickup.

The motor power supply is decoupled by the 0.1uF (C17) ceramic capacitor 22uF (C16) electrolytic capacitor. The physical location of the 0.1uF capacitor, C17, is placed close to the MOSFET bridge. It is to decouple the high frequency current ripple at motor power supply.

5.5 THE CONTROL LOGIC CIRCUIT

The inputs to the 3-phase power drive are six PWM input signals from the dSPACE card. Three of the signals are for controlling the high side power MOSFET and the other three are for controlling the low side power MOSFETs. Each pair of the high-low side PWM signal will never turn on simultaneously. A 800ns dead time is required to ensure that one power MOSFET in a half bridge is switched off before the other one is switched on. The controller side will provide the correct input logic and the dead time to the bridge circuit.

A hardware circuit is built to further safe guard incorrect logic inputs and provide minimum dead time to prevent shoot-through. This protection logic circuitry is implemented by the programmable array logic chip 22V10. The logic design for the high side and low side logic protection is illustrated in Figure 5-8.:

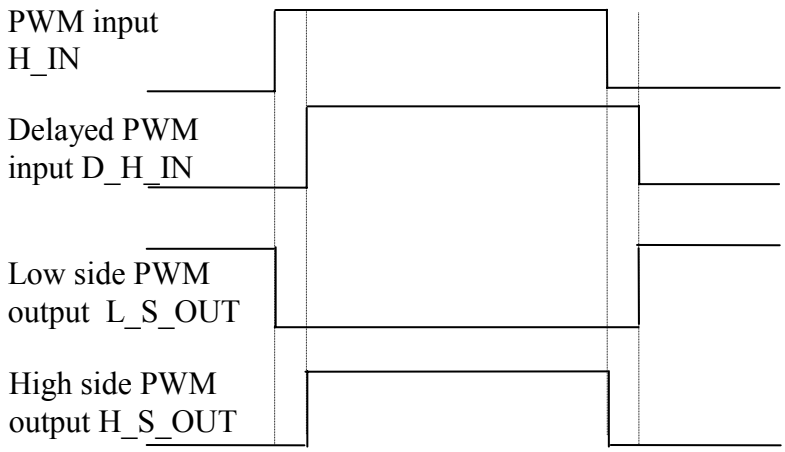

Figure 5-8 Dead time generation logic

As shown in Figure 5-8, the delayed PWM input (by simple RC network) and the PWM input are manipulated to produce PWM output signal with the required dead time. The PWM outputs for the high side and low side are given by the following equations:

$$H\_S\_OUT = (H\_IN * D\_H\_IN) * ENABLE \qquad (5.2)$$

$$L\_S\_OUT = /(H\_IN + D\_H\_IN) * ENABLE \qquad (5.3)$$

where the ENABLE is a high active power bridge enable signal.

The dead time generation for the 3-phase power drive is implemented by the GAL22V10 programmable logic devices (PLD) chip. The source code for the PLD chip can be found in the APPENDIX IV.

5.6 THE CURRENT SENSORS

The Hall effect current sensors are used for detecting the phase current of the LPMSM. It has the advantages of direct measuring the load current and providing isolation between the power side and the small signal controller side. In addition, single power source is required to operate the sensors and no addition floating power supplies are needed.

The current sensors used are the SY-10M from the LEM company. It can measure up to 15A peak and 10A continue current. The sensors are voltage output type and has a gain of 0.4V/A. The full scale output is 6V at 15A peak current. Signal condition circuit is needed to scale the 6V to the 10V full scale ADC input of the dSPACE card. The signal conditioning is shown in Figure 5-9.

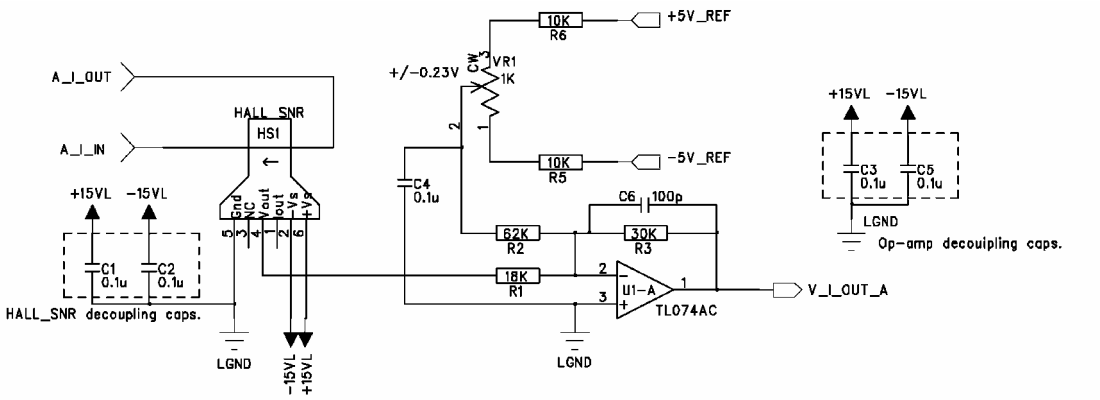

Figure 5-9 Current sensor signal conditioning circuit

The gain of the op-amp is scaled to 1.67 so that it gives 10V full scale output with 15A input current. There is an offset trimmer circuit added to provide addition offset trimming facility. From the specification of the current sensor that it may have 50mA input offset current. The corresponding offset voltage at the operational amplifier U1-A output is 33mV. Therefore the 0.84mV offset provide by the trimmer VR1 can full fill the compensation purpose.

Signal bandwidth of the Hall Effect current sensor is 100KHz. This high bandwidth

characteristic allow the load current can be closely monitor and provide minimum phase delay before the current signal is sampled by the digital controller.

5.7 THE LAYOUT OF THE POWER STAGE

The layout of the 3-phase power stage is shown Figure 5-10. The placement follows the logical signal flow, and the small signal logic side is physically placed far away from the power side. The opto-couplers are aligned in line so as to have a clear separation of the logic side and power stage. The wiring is to avoid running the logic side over the power side and vice visa, to prevent noise pick up and interference.

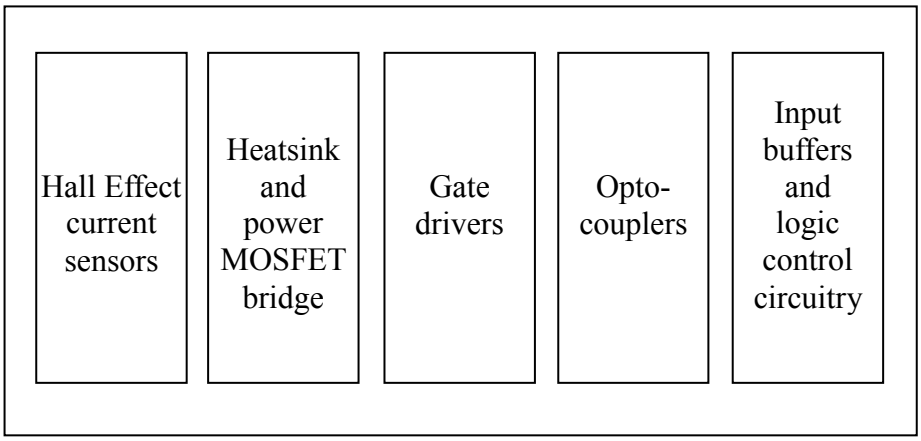

Figure 5-10 Layout of the 3-phase power stage

Since the bridge circuit will automatically clamp the voltage across the motor load to the applied 80V bus voltage, voltage transient will not occur and the MOSFET will not be damaged by transient Drain-Source voltage surge. However, the wiring at the source of the MOSFET needs to be kept short to minimize the stray inductance. Otherwise, transient voltage may appear at the gate driver circuit that may cause unwanted bouncing at the gate driver voltage and lead to excessive heat dissipation.

The schematic of the 3-phase power stage can be found in Appendix II. The actual wire-wrapped 3-phase power stage of the driver is shown in Figure 5-11.

.

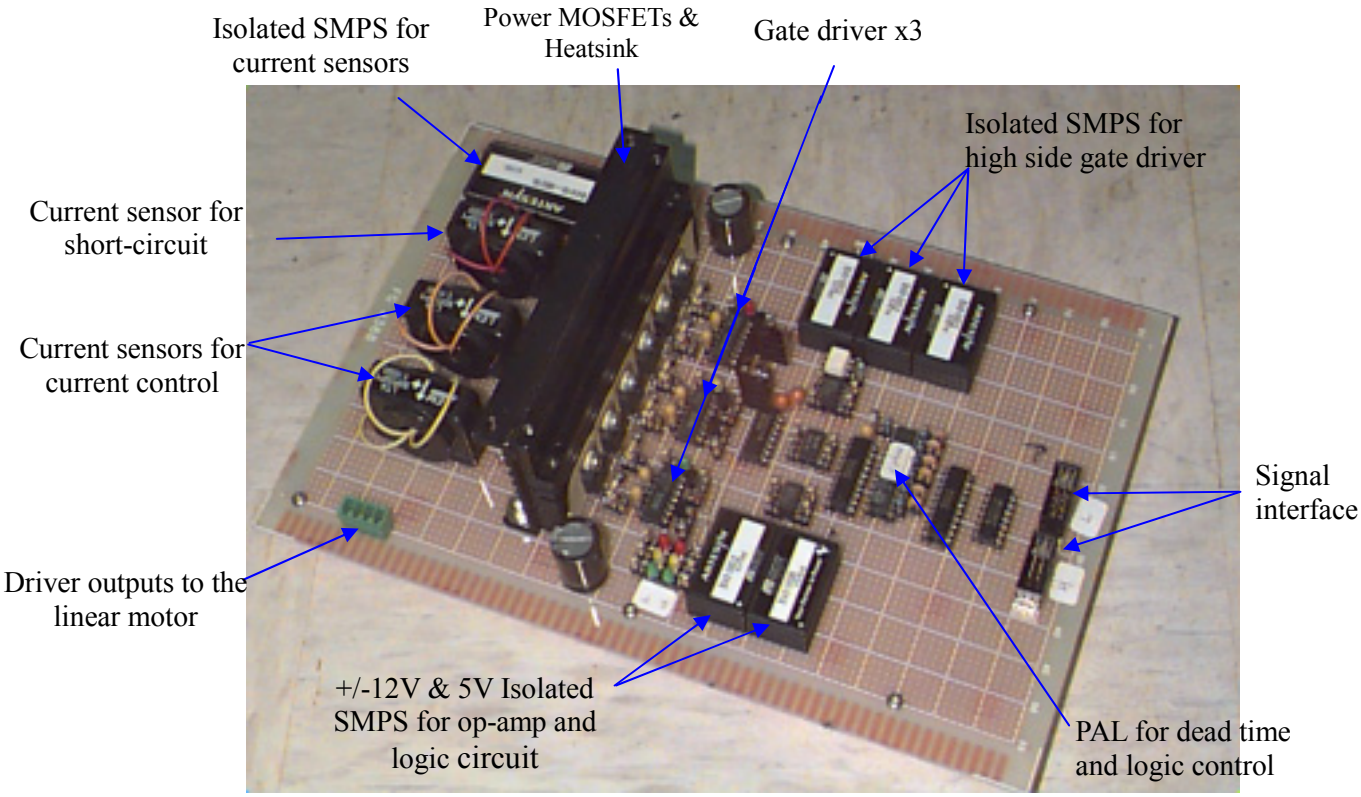

Figure 5-11 Wire-Wrapped 3-Phase Power Stage

CHAPTER SIX EXPERIMENTAL RESULTS AND DISCUSSIONS

The simulations of the LPMSM drive system are done by Simulink toolbox of the Matlab software. The results are printed in the subsequence sections. The actual responses of the system are also measured for comparison.

6.1 MEASURED RESPONSE OF THE LPMSM DRIVE SYSTEM

6.1.1 Measured Current Loop Response

The actual responses of the current drive are shown in Figure 6-1 and Figure 6-2.
The power supply of the drive is at 150Vdc, and the step response of 10% to full step is measured. The current rise time of the drive system is measured at 1.8ms. The current probe setting is at 1A/10mV. No overshoot is observed in the current dynamics of the two phase current outputs. The rise times and fall time are measured to be within 210uS for both phases.

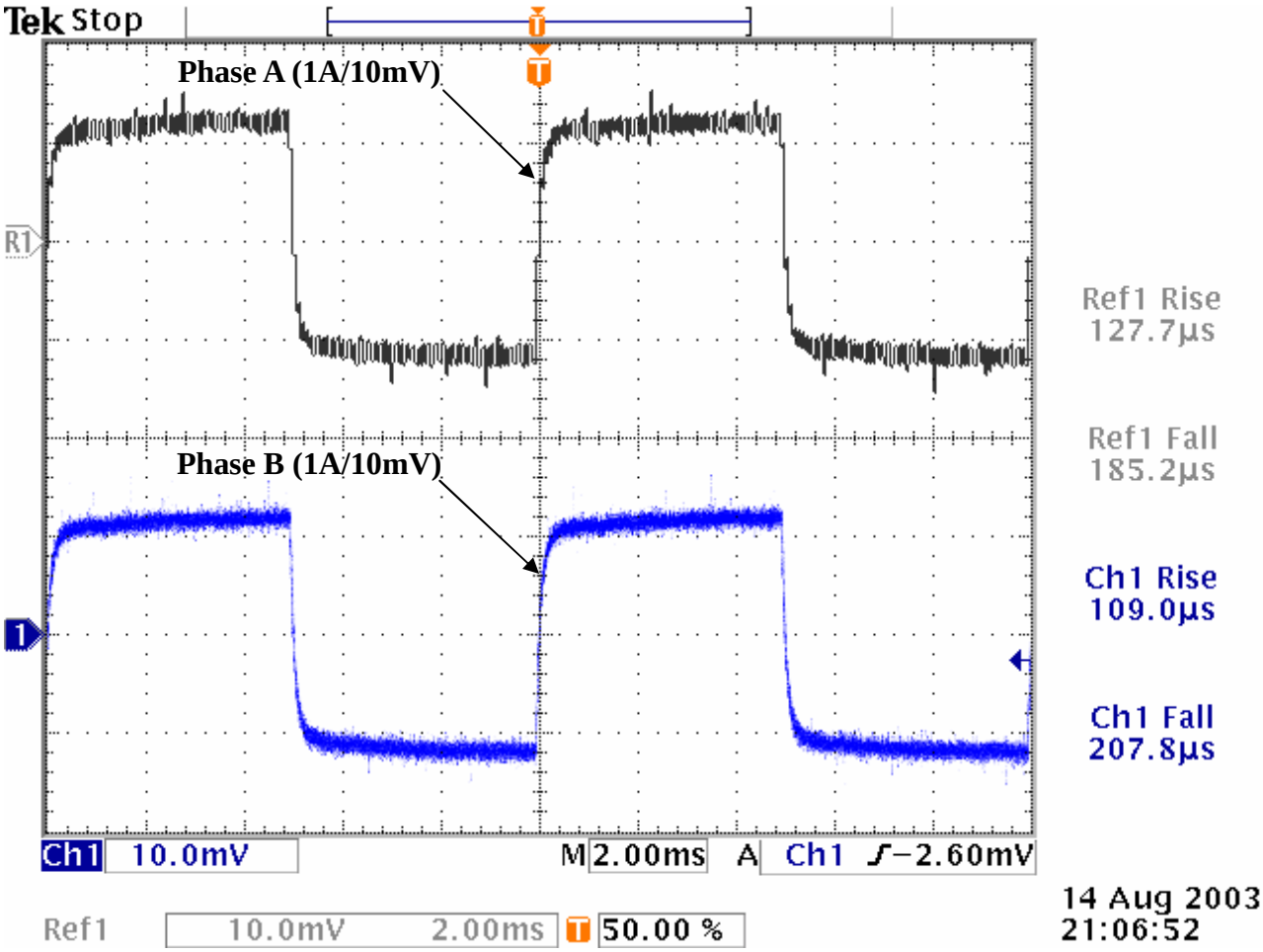

Figure 6-1 Phase A and B 10% current step response

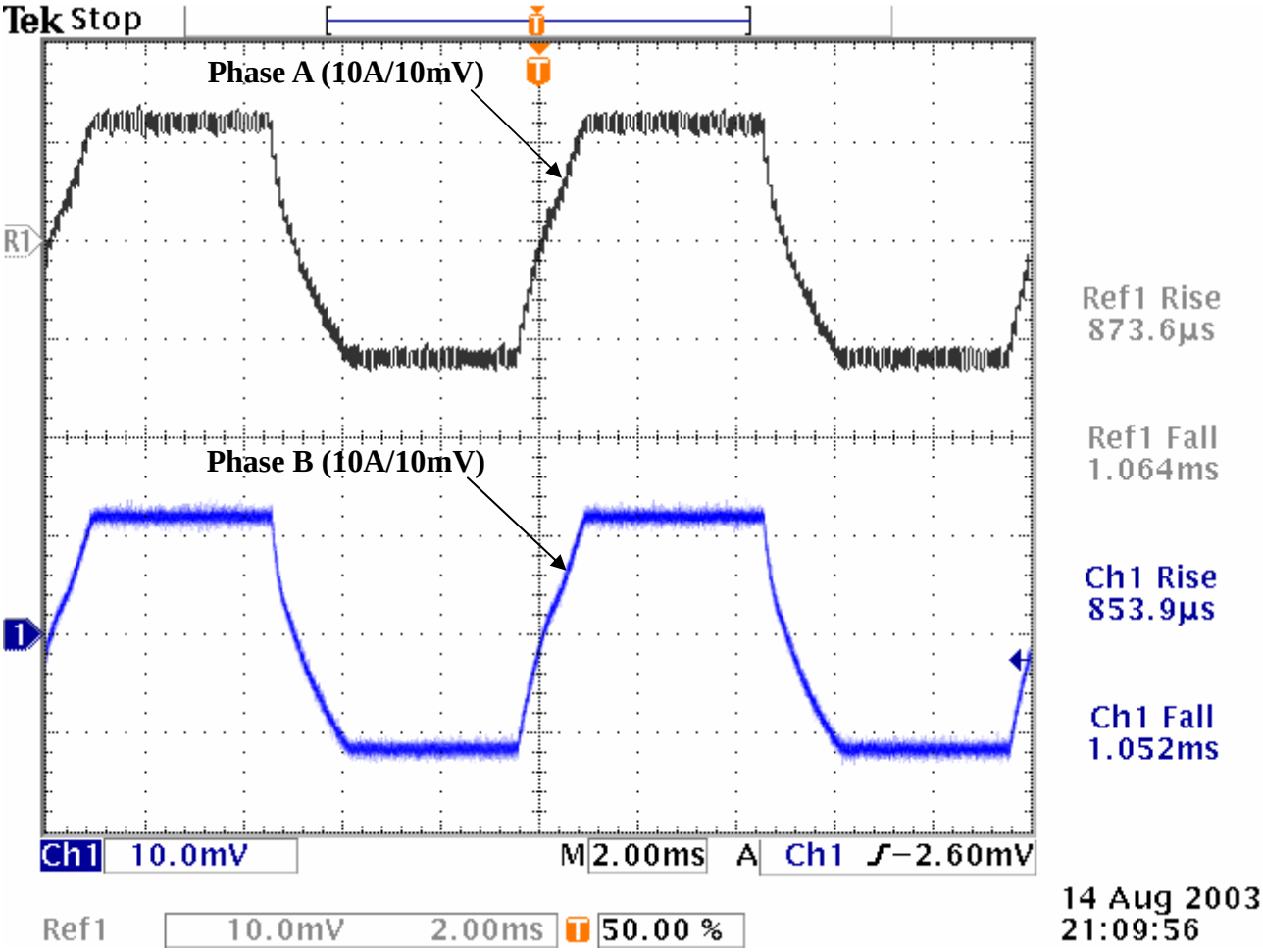

Figure 6-2 Phase A and B 100% current step response

The 100% full-load current step responses are shown in Figure 6-2. The current response is not a pure first order response and non-linearity is observed near the cross-zero regions. It is observed that the full-load step responses do not exhibit overshoot. As the current probe setting is at 10A/10mV, the measured peak current that the power drive can deliver is 12A. The worst rise time and fall time are for both phase A and phase B is within 1.1ms.

6.1.2 Measured Responses of the Robust disturbance Compensator

The profile settings for the measurement are as follow:

Travel distance	12cm
Maximum/minimum velocity	3m/s
Maximum/minimum acceleration	+/- 60m/s^2
Maximum/minimum jerk	+/- 1200000m/s^3
Sampling time	0.5ms

The actual responses of the LPMSM drive system are shown in Figure 6-3 to Figure 6-8.

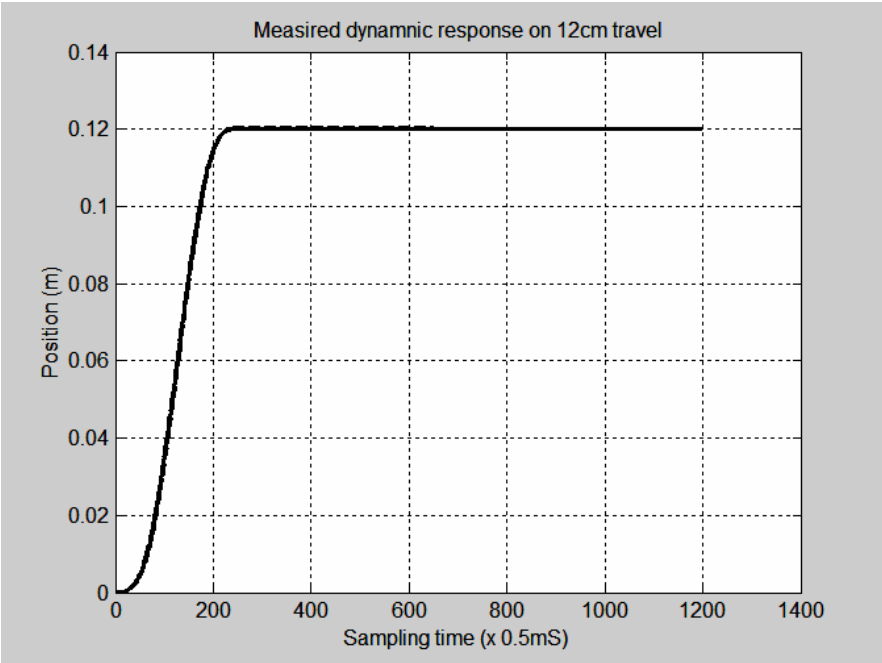

Figure 6-3 Measured dynamic responses

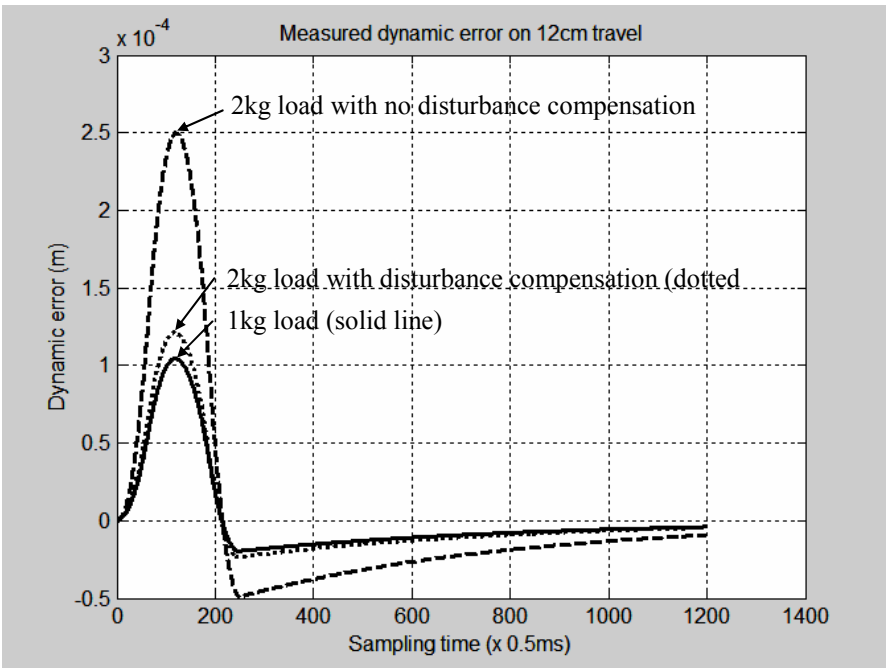

Figure 6-4 Measured dynamic error

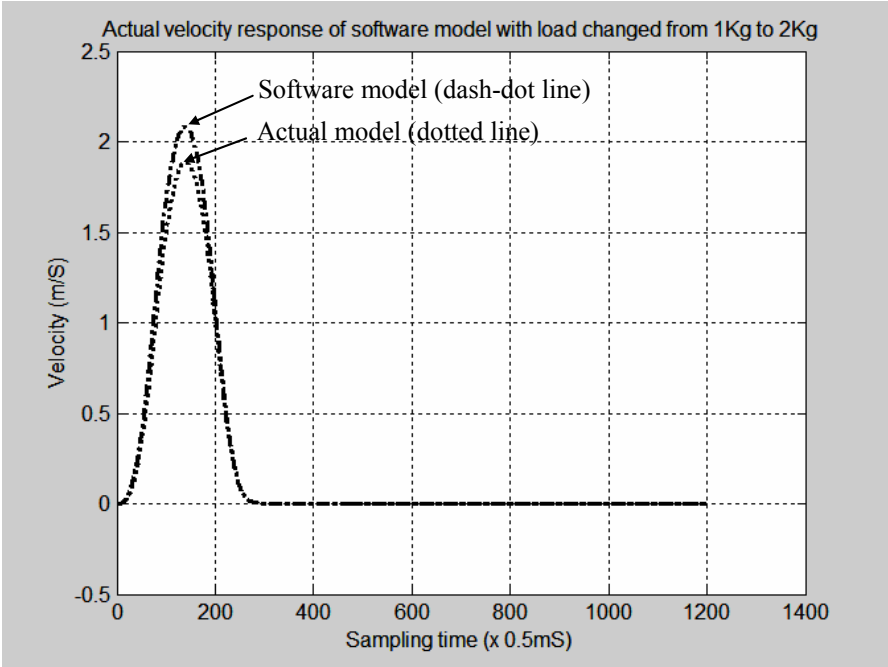

Figure 6-5 Measured velocity of software and actual model

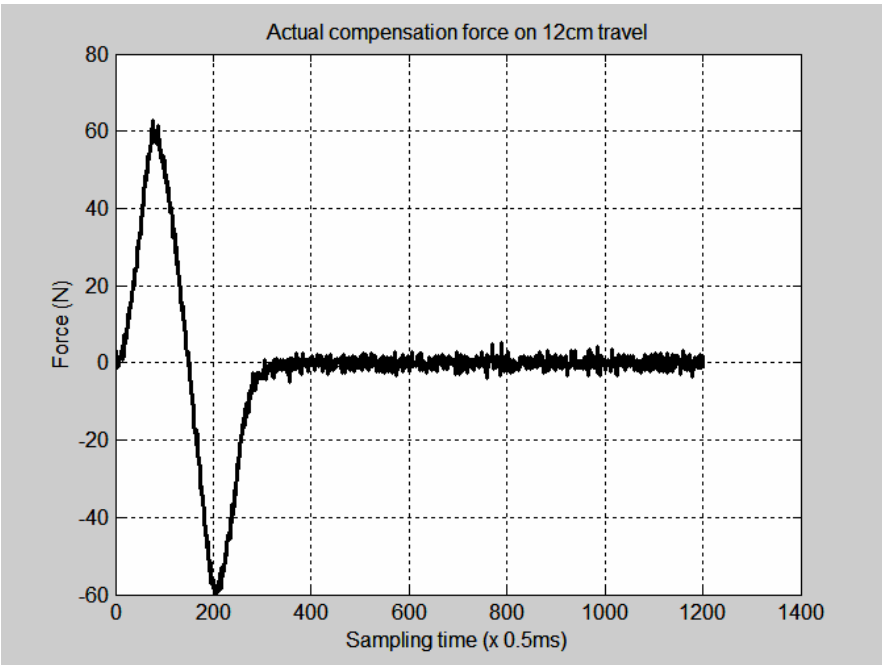

Figure 6-6 Actual output of disturbance compensator

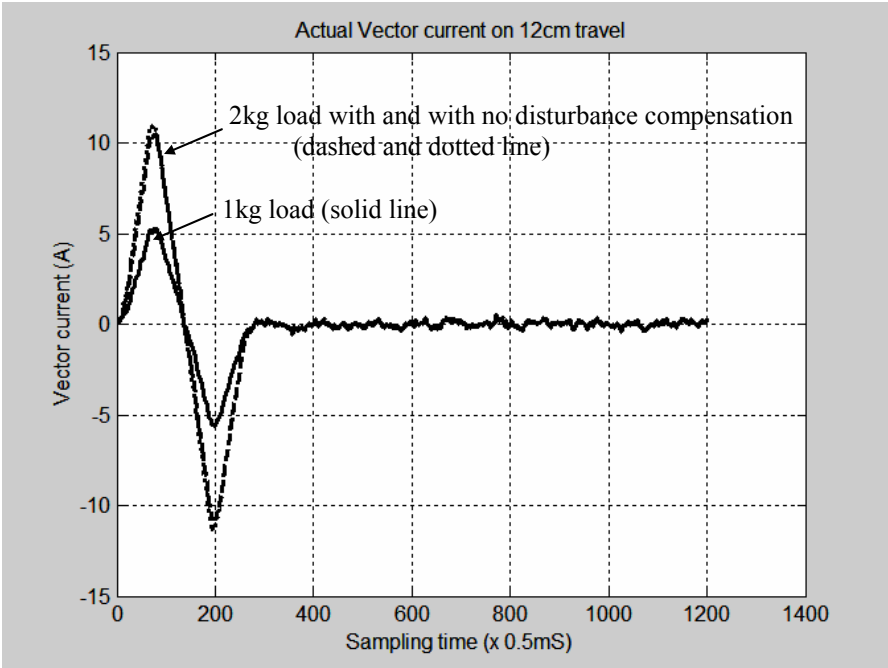

Figure 6-7 Actual vector current

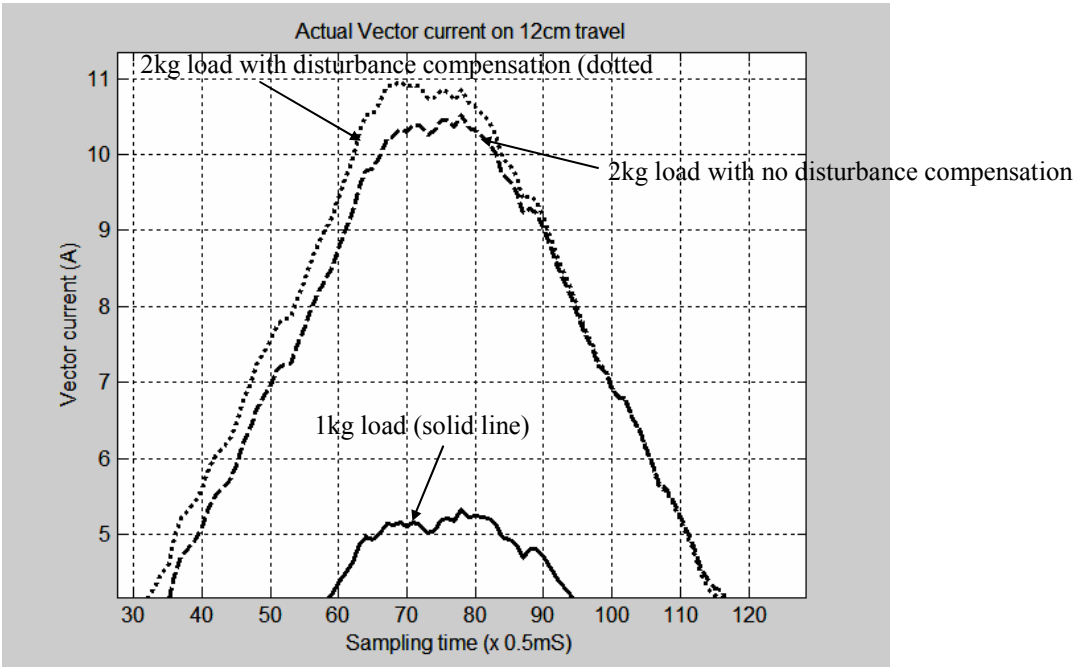

Figure 6-8 Zoom up of actual vector current (Figure 6-7)

The line style of the curves is set to the same as the simulated results. The solid curves are the responses of traditional PID controller with no disturbance compensation. This is taken as reference for comparison. The dashed curves are the responses of the traditional

PID position controller when load is changed from 1kg to 2kg with no disturbance compensation. The dotted curves are the 2kg load response with disturbance compensator activated.

The measured dynamic response of the LPMSM drive system is shown in Figure 6-3. All the three responses are similar. The overshoot for 1kg load response is 0.17%. The overshoots with and with no disturbance compensation is 0.21% and 0.42% respectively.

The measured dynamic error is shown in Figure 6-4. In the 1kg load response, the peak error and time to settle within 15μm are 110μm and 200ms (400 sampling time) respectively. When the load is changed from 1kg to 2kg and disturbance compensation is not activated, the dynamic error is increased from a peak error of 110μm to 250μm. The settling time is increased to 460ms. When the disturbance compensator is activated, the peak dynamic error drops to 120μm and is closed to the 1kg response. With the disturbance compensator, the settling time for the error to fall within 15μm is 250ms (500 sample time).

The measured velocity responses of the software motor model and the actual motor model with disturbance compensation are shown in Figure 6-5. The velocity profile of the actual model is lower than the software model when the load is increased from 1kg to 2kg. The peak velocity difference is 2.08m/S - 1.89m/s = 0.19m/s. The corresponding output of the disturbance compensator is shown Figure 6-6. The disturbance compensator produces a peak correcting force of 60N to minimize the velocity difference between the actual and software model.

The measured vector current responses are shown in Figure 6-7. Both the vector current profiles are similar for the 2kg load response. When the disturbance compensator is not activated, the peak current is increased from 5.3A to 10.5A. If the disturbance compensator is activated, the vector current is increased to 10.9A. The zoom up of the vector currents are shown in Figure 6-8. The activation of disturbance compensator has an effect to advance the vector current.

	1kg load	2kg load	2kg load
Disturbance compensation	-	No	Yes
% overshoot	0.17%	0.42%	0.21%
Peak dynamic error	110μm	250μm	120μm
Settling time (within 15μm)	200ms	460ms	250ms
Peak vector current	5.3A	10.5A	10.9A
Peak velocity	1.925m/s	1.928m/s	1.89m/s
Peak acceleration	6.1G	5.95G	6G
Peak compensation force	-	-	62N

Table 6-1 Measured results summary

An accuracy of about 10μm steady state error and an acceleration of 6G are measured.

6.2 DISCUSSIONS

6.2.1 Response of the Digital Power Drive

From the simulated responses of the power driver in Figure 4-7 and Figure 4-8, and the measured responses in Figure 6-1 and Figure 6-2, it can be found that the measured current rise time is 0.8ms slower then the simulated. This could be due to the non-ideal characteristics of the power devices since ideal switches are used in the simulation. In addition, the total 1.2us dead time for the gate drive circuit also contributes to a slower rise time of the power drive. As a whole, the output currents of the power drive can track the command inputs very well with no overshoot.

6.2.2 Response of the Disturbance Compensated Robust Control System

The simulated responses of the robust control system are shown in Figure 4-9 to Figure 4-14 and the measured responses are shown in Figure 6-3 to Figure 6-8. The simulated improvement and the actual measured improvement of the disturbance compensator are

summarized in Table 6-2 and Table 6-3 respectively.

	1kg load	2kg load (no compensation)	2kg load (with compensation)	% improvement (compared with no compensation)
Overshoot	0.17%	0.33%	0.17%	48%
Peak dynamic error	105μm	210μm	110μm	48%
Settling time (within 15μm)	205ms	415ms	225ms	46%
Peak vector current	5.2A	10.2A	10.5A	-2.9%
Peak acceleration	6.03G	5.98G	6.05G	-1.1%

Table 6-2 Simulated improvement of the disturbance compensator

	1kg load	2kg load (no compensation)	2kg load (with compensation)	% improvement (compared with no compensation)
Overshoot	0.17%	0.42%	0.21%	50%
Peak dynamic error	110μm	250μm	120μm	52%
Settling time (within 15μm)	200ms	460ms	250ms	46%
Peak vector current	5.3A	10.5A	10.9A	-3.8%
Peak acceleration	6.1G	5.95G	6G	-0.8%

Table 6-3 Actual improvement of the disturbance compensator

There are some discrepancies between the measured and the simulated results. The differences could be due to the inaccuracy of the specified static and dynamic friction force of the linear motor. In addition the cogging force and the loss in the power drive system are not taken into account. Also it is assumed that an ideal switch is used in the Matlab model of the power driver, while actually it is not the case. It is logical that the faster the motion, the higher the dynamic frictional losses and hence more power is needed to drive the LPMSM at high speed.

There is particular high difference in the overshoot figures between the simulated and the measured values (see Table 6-2 and Table 6-3). The difference can be up to 27% in the case of 2kg response with no compensation. The overshoot in all case is within 0.5%, which is a very low figure and can be treated as insignificant.

The peak vector current and peak acceleration of the simulated and measured results are well within 5% difference. The settling time is the key figure to determine the performance of the motion system. The shorter the settling time the faster is the process can be completed. The difference is around 10% in general. Therefore, the measured motion dynamics match well with simulated motion dynamics.

Refer to Table 6-2 and Table 6-3, in the 1kg load response, the simulated peak error and time for settling within 20μm error are 105μm and 205ms respectively. While measured peak error and time for settling within 20μm error are 110μm and 200ms respectively. The peak vector currents reach a peak of 5.2~5.3A in both the cases as can been seen in Figure 4-13 and Figure 6-7. Thus the simulated and measured dynamic responses at 1kg load are very close together and can be a good start for further measurement and comparison.

.

The effects of the torque compensator can be observed in both the simulated and actual measured results. For both cases, if the disturbance compensators are disabled, an increase in position error of up to 100% is observed when the load increases from 1kg to 2kg. The position response experiences some slight overshoot (0.33% for the simulated and 0.42% for the measured). The corresponding actual position error increases from a peak of 110μm to 250μm. It takes 460ms for the error to settle within 20μm. When the disturbance compensator is activated, the dynamic error reduces to almost the same as the 1kg load. The dynamic error settles to within 20μm in 200ms. The same trend is observed in the simulation results. Similar trend can be found in the simulation results.

When the compensation loop is enabled, the actual peak dynamic error with 2kg load reduces to 120μm, and is close to the original 1kg load response. But an investigation on the vector currents (see Figure 6-7 and Table 6-3) shows that there is only 3.8% increase in the motor currents to achieve the reduced dynamic error benefit. A close look on the vector currents curves (Figure 6-8) reveals that the vector current has a phase advance profile as compared to the response with no compensation. More or less the same observations can be found in the simulation results. Another observation is that the system takes almost the same driving current in order to correct the motion to the desired

profile. In other words, the system can withstand 100% load change with insignificant increase in the dynamic error and the vector current.

The dynamic responses show that the motor can track the command to within the measured 250μm peak error and 460ms settling time when the disturbance compensator is not activated. When the load is varied from 1kg to 2kg the peak vector current (or the thrust) is increased from 5.3A to 10.9A, approximately 100% increase. But the position error of both the double load cases has a reduced error with the disturbance compensation loop is activated. The measured settling time for within 15μm is reduced from 460ms to 250ms, which is close to the original 200ms settling time. Hence the disturbance compensator has significant effect in maintaining the performance consistence due to load variation.

CHAPTER SEVEN CONCLUSIONS AND RECOMMENDATIONS

7.1 CONCLUSIONS

This research project has been carried out to develop a fully digital drive system for the LPMSM. The models of the motor, driver and overall control system have been derived and simulated by the Matlab Simulink. The Real-Time Workshop toolbox of the Matlab software and the dSPACE controller card DS1102 are used for building the digital controller of the system. A wire-wrapped 3-phase power driver is for the current driver of the LPMSM. A robust control scheme is designed and implemented to compare the actual motor acceleration with the acceleration of a software model. A compensation torque is then derived and fed to the power drive to correct the dynamic response of the system to the desired value. The measured results of the system show that:

- The driver can deliver 12A peak and 4A rms current with 500Hz bandwidth.
- The developed torque compensation loop can improve the system robustness to load variation.
- The system can achieve the required 150ms settling time with 100% load change at 12cm travel distance.
- The system can settle to within 15μm in 250ms for a load variation of 1kg to 2kg, and position accuracy is ±10μm.
- The system can achieve peak velocity of 2m/s with 6G acceleration capability.

During the research of this project there are two findings. The first finding is on the replacement of the step-input profile with an S profile. With the S function input profile, the step error that appeared at the beginning of the motion is much smaller. It avoids saturation on the controller and the current drive. It also implies a reduced stress on the system and the reduction of the mechanical vibration of the system.

Another finding is on the input to the current drive. It can easily be saturated by the torque compensation when the control parameters of the torque loop are not well tuned. This is due to the fast response of the torque loop; it tries to minimize the velocity error developed between the actual motor and the software motor model. If the saturation occurs under this situation, the system drive will go into the non-linear region and the

performance of the motion system becomes unpredictable. This saturation can be avoided partly by the S profile input of the command and partly by the suitable design of the overall drive system. A sufficient force margin must be reserved in the design to allow the system to have sufficient correction force to track the motion dynamics.

To summarize, the proposed control system can be used to drive the LPMSM at high speed with a consistent desired dynamic performance. The plug-in feature of the compensator allows it to be built in the controller system with minimal software changes and development effort. Also the overall stability of the original system can be preserved. Thus, it is very useful in the application of semi-conductor package machines.

7.2 RECOMMENDATIONS

Since the derived fully digital control system is implemented by the dSPACE controller, PC and Matlab software, a useful future work is to implement the whole control system on a DSP chip to allow a more cost-effective product for general usage.

The saturation effect of the system is also worth a deeper study, to enable the development of a better design rule for the control parameter tuning and produces a stable system even at saturation region.

A third order profile is used in this research. There is a need to study any further benefit of using high order profiles in high-performance motion application of the LPMSMs.

ACHIEVEMENTS OF THE PROJECT

Through the investigation work of this project, the following deliverables have been achieved:

(i) Developed a fully digital drive system for robust control of permanent magnet synchronous motors. The system is built with a Pentium III PC, a dSPACE DSP controller card, the Simulink and real-time workshop toolbox of the Matlab software. The system has the advantages of high noise immunity, flexible parameter and controller setting.

(ii) Constructed a detailed model for the linear PMSM with the Simulink toolbox of the Matlab software. The model is verified experimentally to be accurate and is used for the controller design and verifications.

(iii) Proposed a robust control method to compensate the load variation of the linear drive system. The actual load response is compared with a build-in software model and a compensation signal is generated to correct the dynamic performance of the control system to a desired one. Satisfactory output tracking performances can still be achieved for a 100% load variation (from 1kg to 2kg).

(iv) Verified the fully digital drive and control methodology through

(a) Simulation and

(b) Hardware implementation

The experimental results matched well with the simulation results. This validates the proposed robust control and can be applied in precision position control applications so as to improve the system robustness and tracking performances.

AWARD

(1) Received the best paper award for the paper:
MSW Tam, NC Cheung, “An All-Digital High Performance Drive System for Linear Permanent Magnet Synchronous Motor,” *CPSS 2001 Conference Proceedings* vol. 14, p.321, Sept 2001, in the 14th China Power Supply Society bi-annual meeting, CPSS 2001 in Beijing.


证 书

Hong Kong Polytechnic University : Michale S.W.Tam, Norbert C.Cheung

你在中国电源学会第十四届学术年会上发表的 *An All-Digital High-Performance Drive System for Linear Permanent Magnet Synchronous Motor* 论文被评为优秀论文。特发此证

AUTHOR’S PUBILCATIONS

(1) MSW Tam, NC Cheung, "A high-speed, high-precision linear drive system for manufacturing automations," *IEEE APEC 2001 Conference Proceedings*, vol. 1, no 13A4, Mar 2001, in Anaheim, L.A., USA.

(2) KKC Chan, MSW Tam, NC Cheung, "Adaptive current control of variable reluctance finger gripper," *IPEC 2001 Proceedings*, vol. 2TP-8.1 May 2001, in Singapore.

(3) MSW Tam, NC Cheung, “An all-digital high performance drive system for linear permanent magnet synchronous motor,” CPSC 2001 Conference Proceedings vol. 14, p.321, Sept 2001, in Beijing.

REFERENCES

[1] I. Boldea and S. A. Nasar, *Linear Electric Actuators and Generators*, Cambridge University Press, 1997.

[2] M. S. Sarma, *Electric Machine - Steady State Theory and Dynamic Performance*, West Publishing Company, 1994.

[3] D. Y. Ohm, "Control and application of AC servo motors," 26th Annual Symposium on Incremental Motion Control Systems and Devices, July 1997.

[4] I. Boldea and S.A. Nasar, *Vector Control of AC Drives*, CRC Press Inc, 1992.

[5] Shahian and Hassul, *Control System Design Using Matlab*, Prentice-Hall, 1993.

[6] J. S. Ko, J. H. Lee and M. J. Youn, "Robust digital position control of brushless DC motor with adaptive load torque observer," *IEE Proc. Electr. Power Appl.*, vol.141, no.2, Mar. 1994.

[7] J. Hu, D. M. Dawson and K. Anderson, "Position control of a brushless DC motor without velocity measurement," *IEE Proc.-Electr. Power Appl.*, vol.146, no.2, Mar.1995.

[8] F. J. Lin, K. K. Shyu and Y.S. Lin, "Variable structure adaptive control for PM synchronous motor drive," *IEE Proc.-Electr. Power Appl.*, vol.146, no.2, Mar. 1999.

[9] Y. Dote, "Servo Motor and Motion Control Using Digital Signal Processing," Prentice Hall, 1990.

[10] J. D. V. Wyk, "Power electronic converters for motion control," *Proc. of IEEE*, pp.1194-1214, Aug. 1994.

[11] J. S. Ko, J. H. Lee, "A new approach for robust digital position control of brushless direct drive motor with load torque observer," *PCC-Yokohama*

[12] E. Cerruto, A. Consoli, "A robust adaptive controller for PM motor drives in robotic applications," *IEEE Trans. on Power Electronics*, vol.10. no.1, Jan. 1995.

[13] F. J. Lin, "Real-time IP position controller design with torque feedforward control for PM synchronous motor," *IEEE Trans. on Industrial Electronics*, vol.44, no.3, Jun. 1997.

[14] T. Umeno, "Robust speed control of DC servo motors using modern two degrees of freedom controller design," *IEEE Trans. on Industrial Electronics*, vol.38. no.5, Oct. 1991.

[15] J. F. Gieras and M. Wing, *Permanent Magnet Motor Technology: Design and Application*, Marcel Dekker, Inc., 2002.

[16] J. F. Gieras and Z. J. Piech, *Linear Synchronous Motors: Transportation and Automation Systems*, CRC Press, 2000.

[17] D. W. Novotny and T. A. Lipo, *Vector Control and Dynamics of AC Drives*, Oxford Science Publications, 1996.

[18] M. Bertotti, *Smart Power ICs*, Springer, 1996.

[19] J. Holtz, "Pulse width modulation for electronic power conversion," *Proc. of IEEE*, vol. 82, no.8, pp.1194-1214, Aug. 1994.

[20] A. M. Hava, R. J. Kerkman and T. A. Lipo, "Simple analytical and graphical tools for carrier based PWM methods," *Proc. of IEEE PESC*, vol.2, pp. 1462-1471, 1997.

[21] S. H. Kim and S. K. Sul, "Voltage control strategy for maximum torque operation of an induction machine in the field-weakening region," *IEEE Trans. on Industrial Electronics*, vol. 44, no.4, Aug. 1997.

[22] M. S. W. Tam and N. C. Cheung, "A high-speed, high-precision linear drive system for manufacturing automations," *IEEE APEC 2001 Conference Proceedings*, vol. 1, no.13A4, Mar.2001.
[23] K. K. C. Chan, M. S. W. Tam, N. C. Cheung, "Adaptive current control of variable reluctance finger gripper," *Proc. on IPEC 2001*, vol. 2TP-8.1 May 2001.
[24] M. S. W. Tam, N. C. Cheung, "An all-digital high performance drive system for linear permanent magnet synchronous motor," *CPSC 2001 Conference Proceedings*, vol. 14, pp.321, Sept 2001.
[25] S. R. Trout, "Material selection of permanent magnet, considering thermal properties correctly", *Proc. on Electrical Electronics Insulation Conference and Electrical Manufacturing & Coil Winding Conference*, pp.365-370 Oct. 2001.
[26] R. Petrie, "Permanent magnet in review", *Proc. on Electrical Electronics Insulation Conference and Electrical Manufacturing & Coil Winding Conference*, pp.207-210 Oct. 1993.
[27] S. K. Pal, "Comparative study of the design and manufacturing process of electrical motors with low and high energy permanent magnets," *Electrical Machines and Drives*, Conf. Publ. no. 376, pp. 339-346 Oct. 1993.
[28] P. K. Budig, "The application of linear motors," *Power Electronics and Motion Control Conference, Proc. PIEMC 2000*, pp.1336-1341, vol. 3, Aug. 2000.
[29] T. J. E. Miller, *Brushless Permanent-Magnet and Reluctance Motor Drives*, Oxford, 1989.
[30] P. Vas, *Vector Control of AC Machines*, Oxford, 1990.
[31] D. W. Novotny and T. A. Lipo, *Vector Control and Dynamics of AC Drives*, Oxford, 1998.
[32] I. Boldea and S. A. Nasar, *Linear Electric Actuators and Generators*, Cambridge University Press, 1997.
[33] D. G. Giulio, *Reliability of Eletronic Packages and Semiconductor Devices*, New York: MCGraw-Hill, 1997.
[34] I. Boldea and S. A. Nasar, *Electric Drives*, CRC Press, 1999.
[35] V. Petrovic, R. Ortega, A. M. Stankovic and G. Tadmor, "Design and implementation of an adaptive controller for torque ripple minimization in PM synchronous motors," *IEEE Trans. on Power Electronics*, vol. 15, no. 5, pp. 871-880, Sep. 2000.
[36] G. P. Widdowson, D. Howe and P. R. Evison, "Computer-aided optimization of rare-earth permanent magnet actuators," *International Conference on Computation in Electromagnetics*, pp. 93 –96, Nov. 1991.
[37] Y. J. Liu, G. P. Widdowson and S. Y. Ho, "Design analysis of a PM motion system for semiconductor applications," *The Fourth International Symposium on Linear Drives for Industry Applications*, Sep. 2003
[38] W. C. Gan and L. Qiu, "Design and analysis of a plug-in robust compensator: an application to indirect-field-oriented-control induction machine drives," *IEEE Trans. on Industrial Electronics*, vol. 50, no. 2, pp.272-282, Apr. 2003.
[39] J. W. F. Cheung, A. W. K. Chung and N. C. Cheung, "Self-tuning control of brushless servo drive for a high performance tracking manipulator**,"** *Proc. of Power Electronics and Drive Systems*, vol. 1, pp. 297-301, May 1997.
[40] K. Zhou, J. C. Doyle and K. Glover, *Robust and Optimal Control*, Prentice Hall, 1996.
[41] K. Zhou and J. C. Doyle, *Essentials of Robust Control*, Prentice Hall, 1998.

[42] Y. T. Kao and C. H. Liu, “Analysis and design of microprocessor-based vector controlled induction motor drives,” *IEEE Trans. on Industrial Electronics*, vol. 39, no. 1, pp. 46-54, Feb. 1992.
[43] D. M. Dawson, J. Hu and T. C. Burg, *Nonlinear Control of Electric Machinery, Dekker*, 1998.
[44] K. Zhou and Z. Ren, “A new controller architecture for high performance, robust, adaptive, and fault tolerant control,” *IEEE Trans. on Automatic Control*, vol. 46, no. 10, pp. 1613-1618, Oct. 2000.
[45] J. F. Gieras and M. Wing, “Analysis of an universal permanent magnet brushless motor drive,” *Proc. on Power Electronics, Drives and Energy System for Industrial Growth*, vol. 1, pp. 517-522, Jan. 1996.
[46] S. Bhattacharya, D. G. Holmes and D. M. Divan, “Optimizing three phase current regulators for low inductance loads,” *Industry Applications Conference*, vol. 3, pp. 2357-2364, Oct. 1995.
[47] J. O. Krah and J. Holtz, “High performance current regulation and efficient PWM implementation for low-inductance servo motors,” *IEEE Trans. on Industry Applications*, vol. 35 issue: 5, pp. 1039-1049, Sep.-Oct. 1999.
[48] M. Vidyasagar, *Control System Synthesis*, The MIT Press, Cambrigde, 1985.
[49] P. P. Khargonekar and K. R. Poolla, “Uniformally optimal control of linear time-invariant plants: nonlinear time-varying controllers,” *System and Control Letters*, vol. 6, no. 5, pp. 3003-308, 1986.
[50] H.X. Li and P.P.J. Van Den Bosch, “A robust disturbance-based control and its application.” *INT. J. Control*, vol. 58, no. 3, pp. 537-554, 1993.

APPENDIX I. THE DS1102 DSPACE CONTROLLER CARD

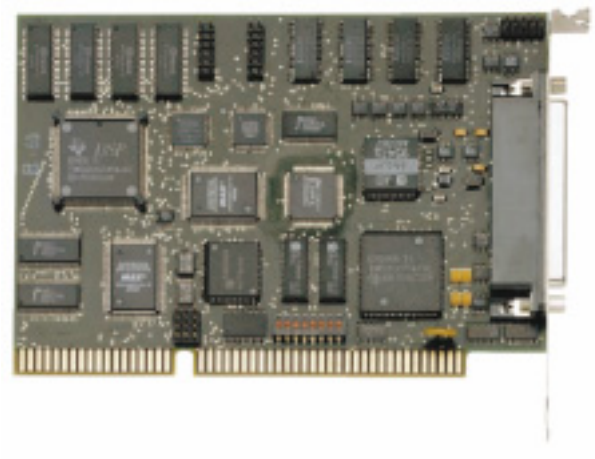

Figure A- 1 The DS1102 dSPACE Controller Card

Function	No of channel	Description
ADC ports	4	12-bit x 2 channel: - ±10V input voltage range - 1.2µS settling time - 65dB S/N ratio 16-bit x2 channel: - ±10V input voltage range - 1.2µS settling time - 80dB S/N ratio
DAC ports	4	16-bit resolution +/-10V, 4uS settling time)
Incremental Encoder ports	2	- Fourfold pulse multiplication - Quadrature phase lines and indexer line - 24-bit counters - up to 8.3MHz count frequency
I/O ports	16	- Programmable digital I/Os - TTL compatible - Bit selectable 16-digital I/O lines - Capture/compare unit of 8 channels (2 in, 4 out, 2 in/out) - PWM generation of up to 6 channels (40nS resolution) - User interrupt

Table A- 1 Features of the DS1102 dSPACE Controller Card

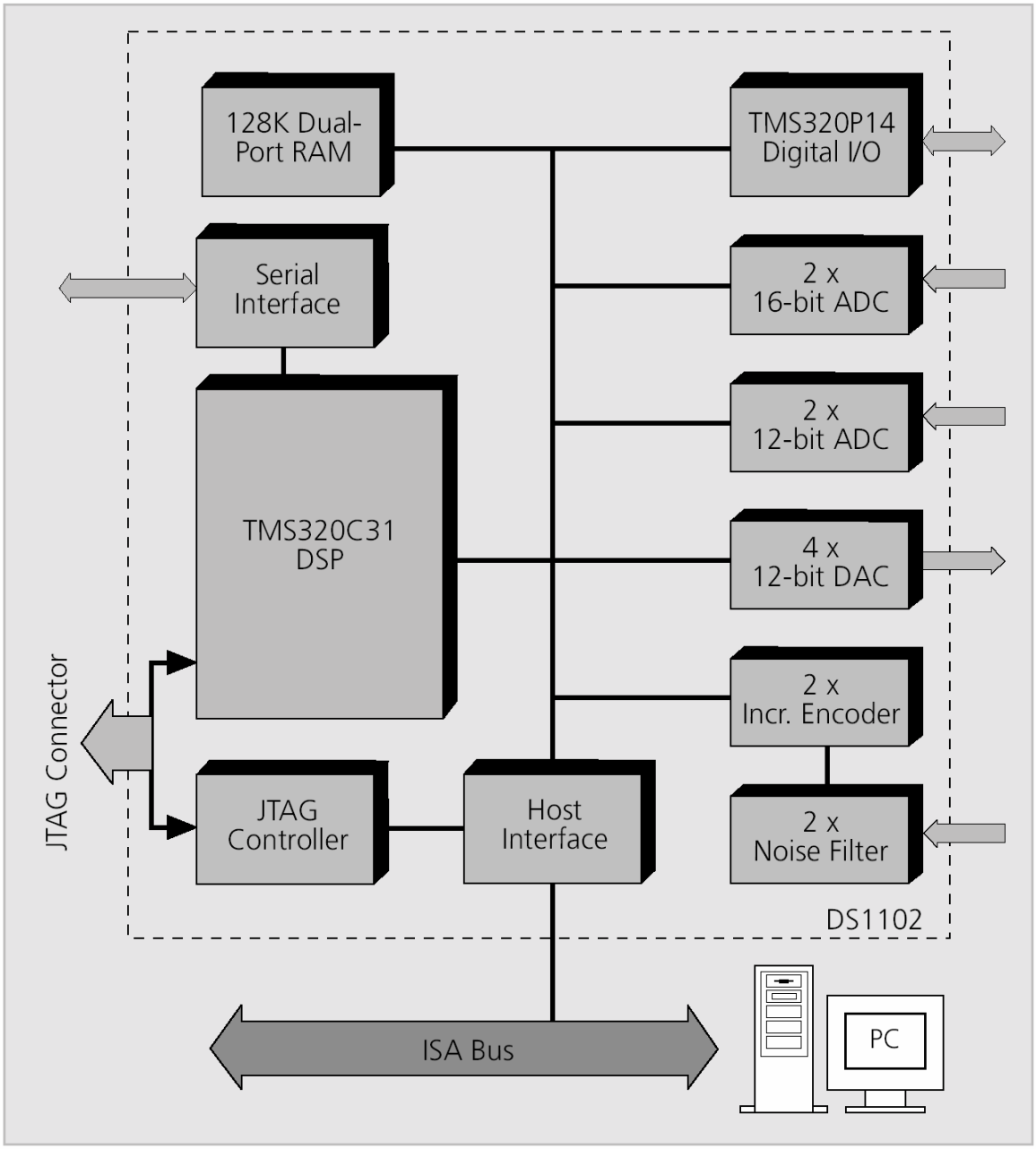

Figure A- 2 Block Diagram of the dSPACE Controller Card

APPENDIX II. THE SCHEMATIC DIAGRAMS OF THE POWER DRIVE

Appendix II.A. Schematic of the Input stage

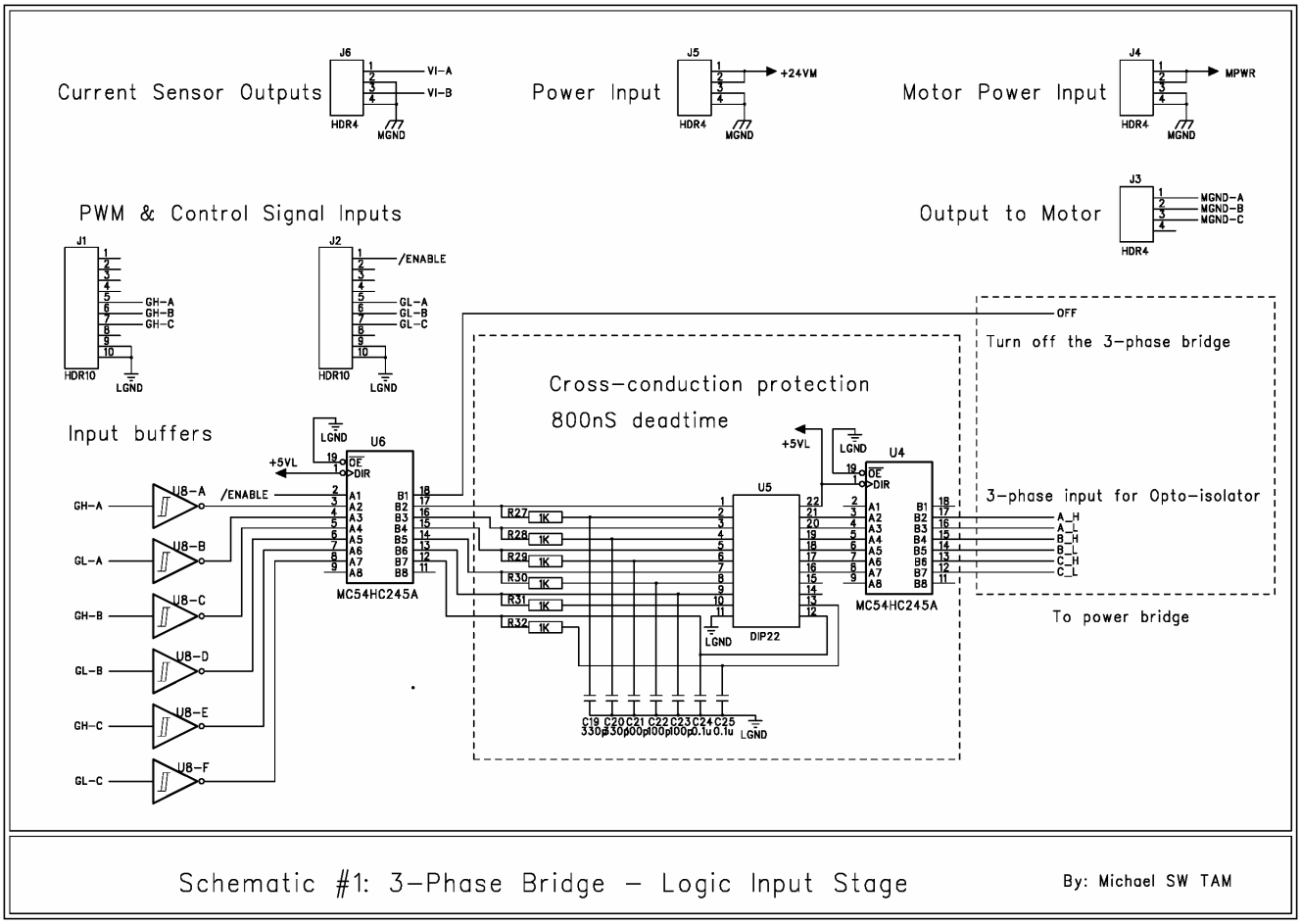

Figure A- 3 Schematic of the Input Stage

Appendix II.B. Schematic of the Phase A Power Bridge

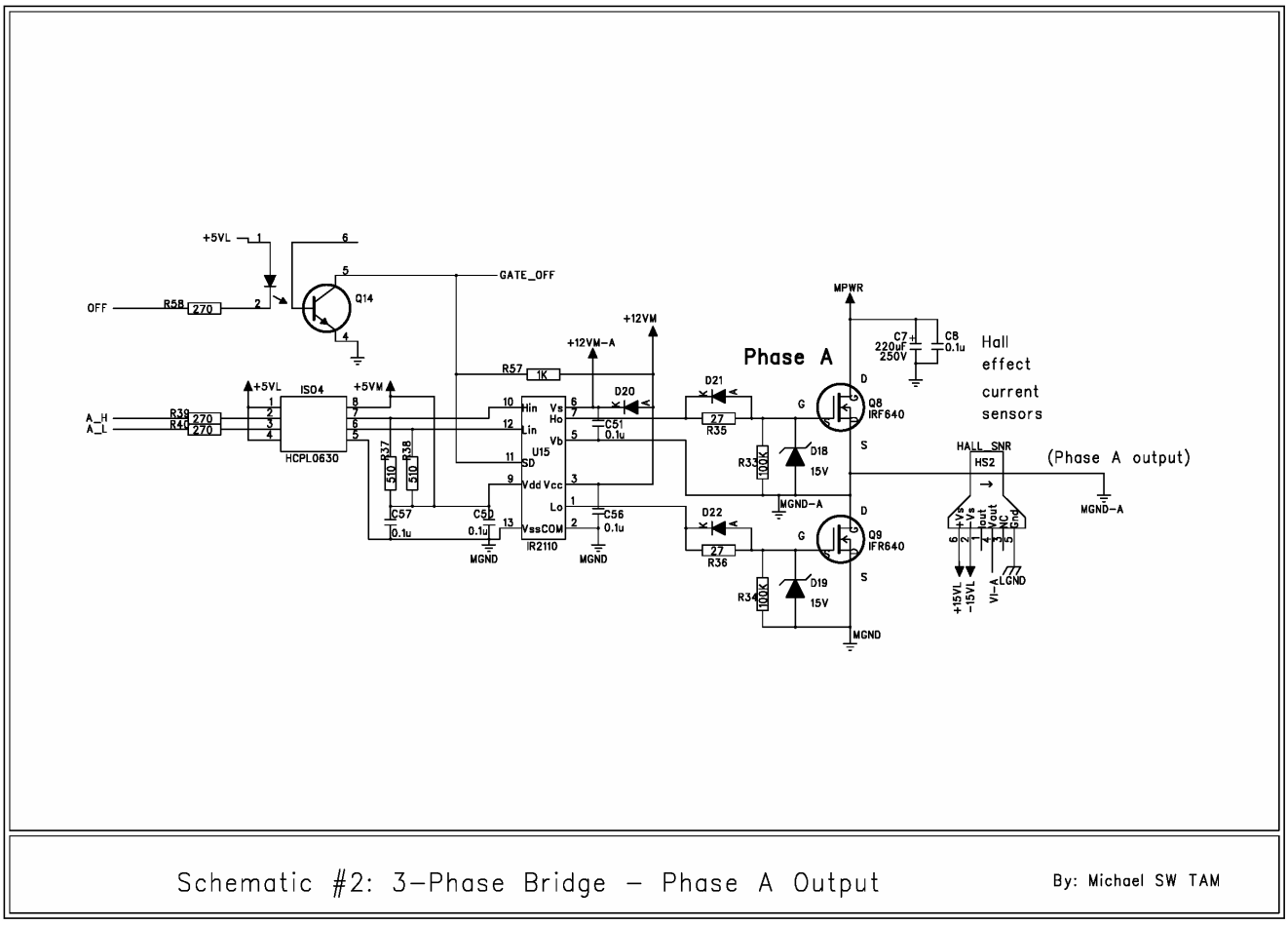

Schematic #2: 3-Phase Bridge - Phase A Output By: Michael SW TAM

Figure A- 4 Schematic of the Phase A Power Bridge

Appendix II.C. Schematic of the Phase B Power Bridge

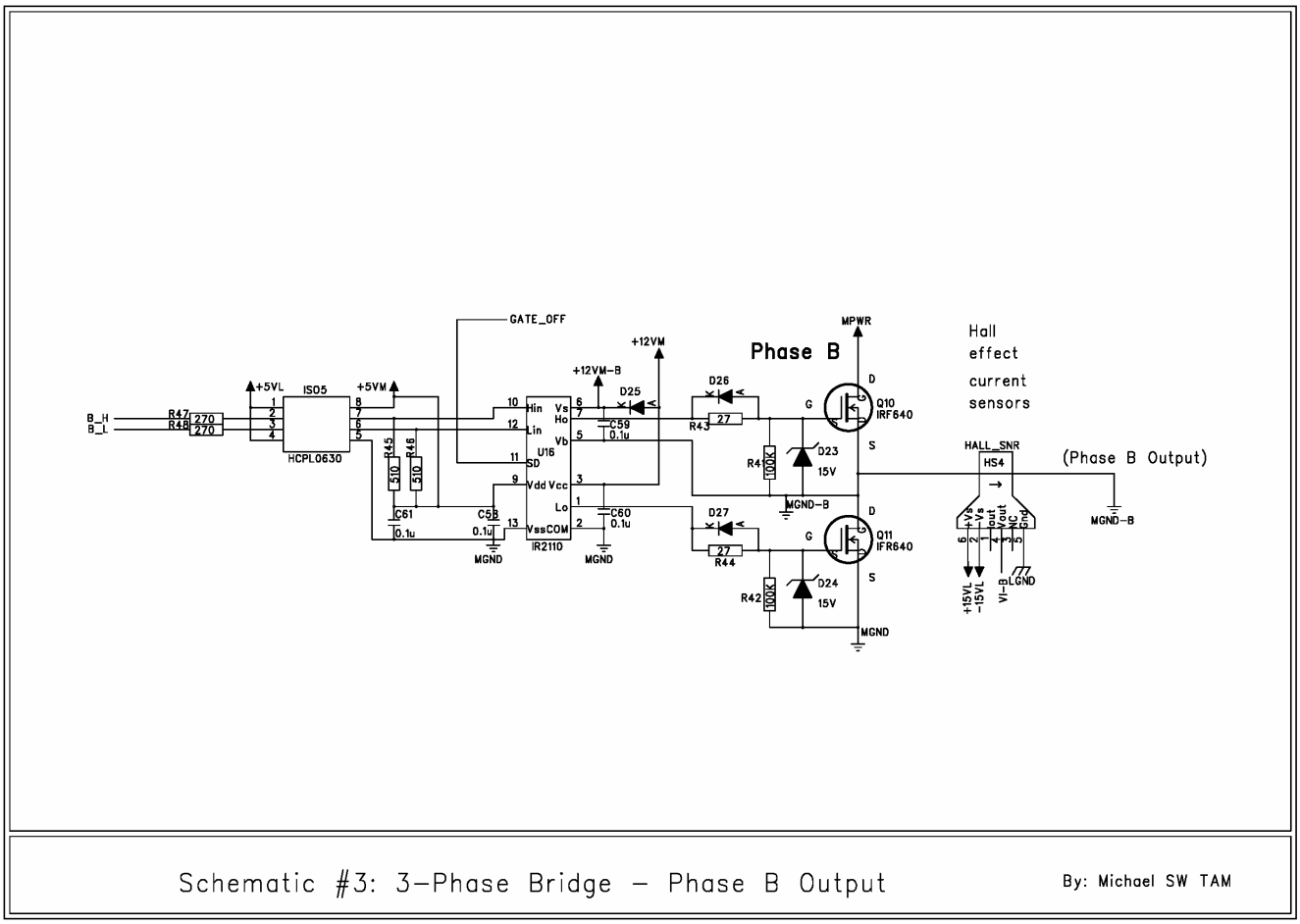

Figure A- 5 Schematic of the Phase B Power Bridge

Appendix II.D. Schematic of the Phase C Power Bridge

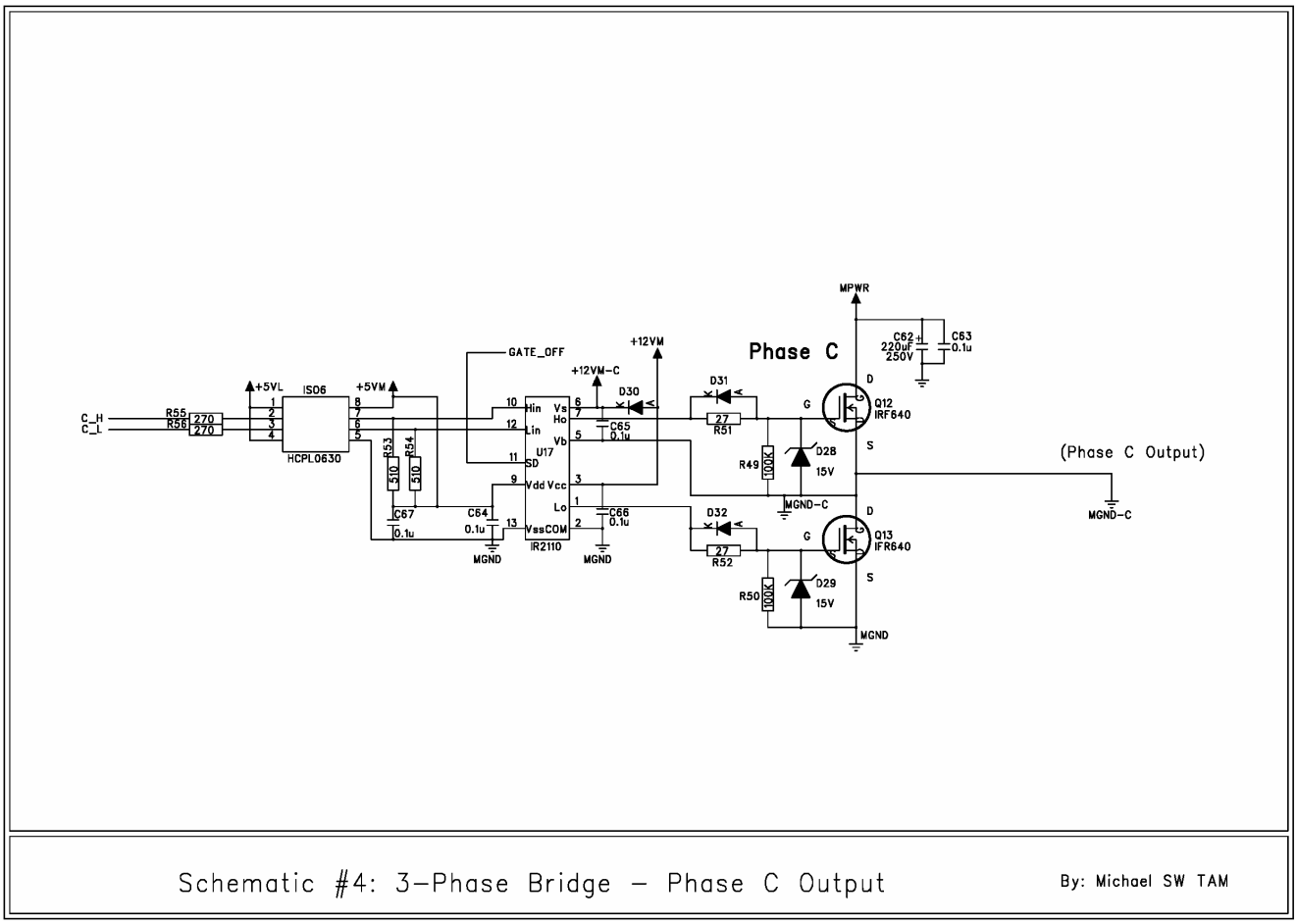

Figure A- 6 Schematic of the Phase B Power Bridge

Appendix II.E. Schematic of the Isolated Power Supplies

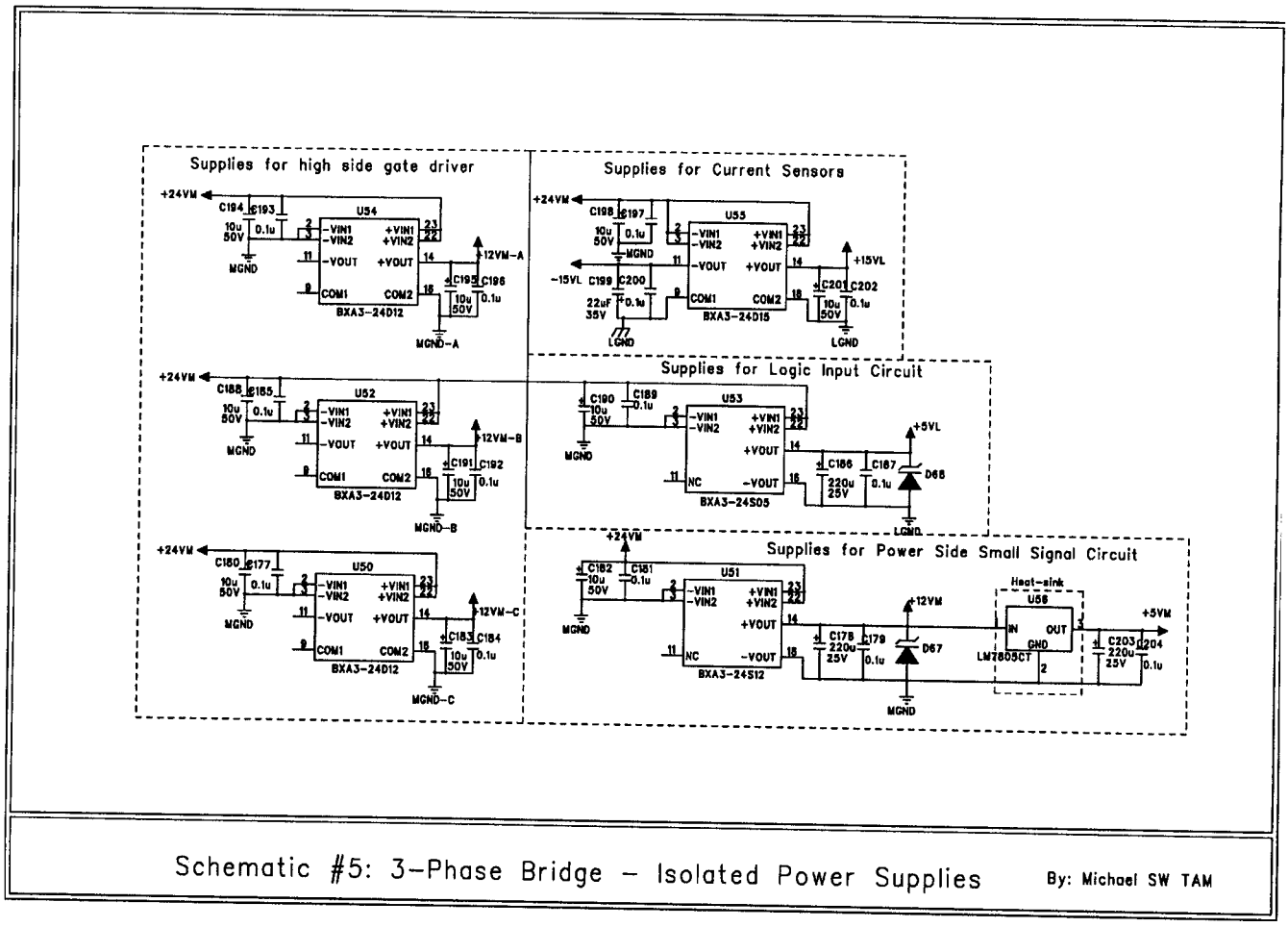

Schematic #5: 3-Phase Bridge – Isolated Power Supplies By: Michael SW TAM

Figure A- 7 Schematic of the Isolate Power Supplies

APPENDIX III. THE MECHANICAL LAYOUT OF THE LPMSM

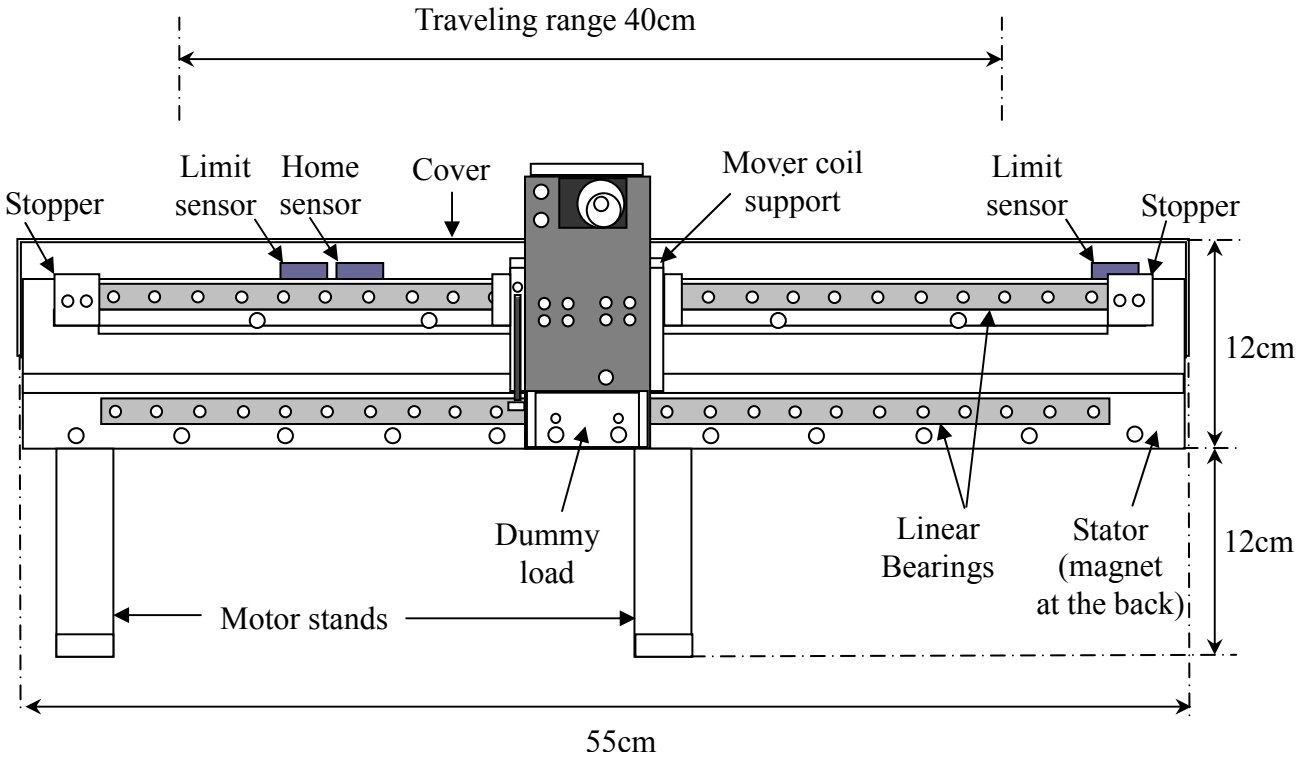

Figure A- 8 Mechanical Drawing of the LPMSM

APPENDIX IV. LOGIC EQUATIONS OF 22V10 PLD CHIP

AMD's PALASM4 compiler is used for editing and compiling the logic description to the JED file for programming into a 22V10 PLD chip.

```
;PALASM Design Description

;---------------------------------- Declaration Segment ------------
TITLE    Cross-Conduction protection for 3-phase bridge driver
PATTERN
REVISION 1.0
AUTHOR   SW Tam
COMPANY  AAA_POLYU
DATE     20Sept1998

CHIP  _3phase  PAL22V10

;----------------------------------- PIN Declarations ---------------
PIN  1        Enable          ; Enable pin : Low = Enable
PIN  2        A_H_in          ; Phase A high side input
PIN  3        A_H_in_dly      ; Phase A high side delayed input
PIN  4        A_L_in          ; Phase A low  side input
PIN  5        A_L_in_dly      ; Phase A low  side delayed input
PIN  6        B_H_in          ; Phase B high side input
PIN  7        B_H_in_dly      ; Phase B high side delayed input
PIN  8        B_L_in          ; Phase B low  side input
PIN  9        B_L_in_dly      ; Phase B low  side delayed input
PIN  10       C_H_in          ; Phase C high side input
PIN  11       C_H_in_dly      ; Phase C high side delayed input
PIN  12       GND             ; Ground
PIN  13       C_L_in          ; Phase C low  side input
PIN  14       C_L_in_dly      ; Phase C low  side delayed input

PIN  15       Protect         ; Protection enable, High active
PIN  18       C_L_out         ; Phase A low  side output
PIN  19       C_H_out         ; Phase A high side output
PIN  20       B_L_out         ; Phase B low  side output
PIN  21       B_H_out         ; Phase B high side output
PIN  22       A_L_out         ; Phase A low  side output
PIN  23       A_H_out         ; Phase A high side output
PIN  24       VCC             ; +5V supply

;----------------------------------- Boolean Equation Segment ------
EQUATIONS

;Description :     Enable is low will hold all output at low.
                  Protect = low => Output = Input (Still controlled by Enable)
;                 Each output can be high after (Td) its complementary output is low.

A_H_out =  Protect * /Enable * (A_H_in * (/A_L_in * /A_L_in_dly)) +
           /Protect * /Enable *  A_H_in;
A_L_out =  Protect * /Enable * (A_L_in * (/A_H_in * /A_H_in_dly)) +
           /Protect * /Enable *  A_L_in;
B_H_out =  Protect * /Enable * (B_H_in * (/B_L_in * /B_L_in_dly)) +
           /Protect * /Enable *  B_H_in;
B_L_out =  Protect * /Enable * (B_L_in * (/B_H_in * /B_H_in_dly)) +
           /Protect * /Enable *  B_L_in;
C_H_out =  Protect * /Enable * (C_H_in * (/C_L_in * /C_L_in_dly)) +
           /Protect * /Enable *  C_H_in;
C_L_out =  Protect * /Enable * (C_L_in * (/C_H_in * /C_H_in_dly)) +
           /Protect * /Enable *  C_L_in;
```

---<END OF THESIS>---